Inorganic Phase Characterization, Corrosion Modelling and Refractory Selection for Direct Contact Steam Generation

Nicole Bond

Thesis submitted in partial fulfillment of the requirements

For a Master of Applied Science in Chemical Engineering

Department of Chemical and Biological Engineering

Faculty of Engineering

University of Ottawa

Abstract

Technological advances are required to reduce the environmental impact of the Canadian oil sands. Oxy-direct contact steam generation (DCSG) is one such way to move toward this goal, by producing steam for oil sands operations with a higher efficiency, lower fresh water consumption, and lower CO_2 emissions than traditional once-through steam generators. For DCSG, untreated process water, which may contain a variety of inorganics, is injected directly into the combustor to produce steam. The inorganic material that may deposit in the combustor as a result of that process water was studied for two applications of DCSG in the Canadian oil sands: (1) steam assisted gravity drainage (SAGD), and (2) mining, in order to inform refractory material selection for the combustor.

For SAGD, free water knockout tank discharge was used as the process water and resulting deposits in the combustor were predicted to be high in silica and sodium oxide, and enriched with sodium sulfate as the potential operating temperature of the combustor was lowered. At the lowest combustor temperature studied (1075 °C), a low viscosity molten salt phase rich in sodium sulfate was also expected to form. It is recommended that the operating temperature of the combustor be as low as possible while still remaining above the formation temperature of this potentially corrosive salt phase, thus in the range of 1200-1250 °C in the regions of the wall where solids are expected to impact it. A number of candidate refractory materials were assessed through corrosion models and corrosion tests. Aluminosilicate based refractory materials should be avoided due to their potential reaction with the sodium oxide in the slag. This can result in formation of low density solid phases such as nepheline, which can damage the refractory material through volume expansion. Of the three refractories tested, mullite zirconia yielded the worst corrosion resistance, with dissolution of the binder phase and full penetration by sodium oxide. Chromia corundum

yielded the greatest resistance to penetration of the materials tested, though some dissolution of the chromia in the slag was still evident. Further investigation into high chrome refractory materials is recommended for this application.

For mining applications, mature fine tailings water (MFT) combined with an oil sands processing water (OPW) was used as the process water for injection. Due to the high liquidus of the resulting inorganic deposits, co-injection of a fluxant is recommended to reduce the liquidus and viscosity of the resulting slag solution, thereby maximizing the combustor efficiency by reducing the required operating temperature. Dolomite was identified as the optimal fluxant, at a concentration of 20 wt % $CaMgO_2$ in the fluxed slag. This mixture was found to have a viscosity of just under 25 Pa·s at 1300 °C, making this a good operating point for the DCSG combustor, as the slag should flow freely and not cause plugging. The corrosion resistance of several candidate refractory materials was assessed through modelling and laboratory scale testing for both the fluxed and non-fluxed slag. Similar to the results for SAGD, of the refractories tested, chromia corundum offered the greatest resistance to penetration, while mullite zirconia was most deeply penetrated by sodium oxide. Again, a chromia-containing refractory is recommended for further investigation for use in the DCSG combustor. Other candidate refractories investigated in the models that warrant testing are chromia spinel and magnesium aluminate spinel. For future work, further corrosion tests at multiple durations are recommended, as well as characterization of refractory samples from CanmetENERGY's DCSG pilot plant and quantification of the effects of slag exposure on the mechanical strength of the refractory materials.

Sommaire

Des progrès technologiques sont nécessaires pour réduire l'impact environnemental des sables bitumineux canadiens. La production de vapeur par contact direct (PVCD) lors d'oxy-combustion est un moyen de progresser vers cet objectif, en produisant de la vapeur pour les opérations des sables bitumineux avec une efficacité plus élevé, une consommation d'eau douce réduite et des émissions de CO_2 réduites par rapport aux générateurs de vapeur traditionnels à passage unique. Pour le PVCD, de l'eau de procédé non traitée, qui peut contenir une variété de substances inorganiques, est injectée directement dans la chambre de combustion pour produire de la vapeur. La matière inorganique qui peut se déposer dans la chambre de combustion à la suite de cette eau de traitement a été étudiée pour deux applications de PVCD dans les sables bitumineux canadiens: (1) drainage par gravité au moyen de la vapeur (DGMV) et (2) exploitation minière, afin d'informer la sélection de matériaux réfractaires pour la chambre de combustion.

Pour le DGMV, la décharge du réservoir de séparation d'eau libre a été utilisée comme eau de traitement et les dépôts résultants dans la chambre de combustion devraient être riches en silice et en oxyde de sodium, et enrichis en sulfate de sodium lorsque la température d'opération potentielle de la chambre de combustion serait abaissée. A la température de chambre de combustion la plus basse étudiée (1075 °C), une phase de sel fondu de faible viscosité riche en sulfate de sodium devait également se former. Il est recommandé que la température d'opération de la chambre de combustion soit aussi basse que possible tout en restant au-dessus de la température de formation de cette phase de sel potentiellement corrosive, donc dans l'intervalle de 1200-1250 °C dans les régions de la paroi où les solides impactent. Un certain nombre de matériaux réfractaires candidats ont été évalués au moyen de modèles de corrosion et d'essais de corrosion. Les matériaux réfractaires à base d'aluminosilicate doivent être évités en raison de leur réaction potentielle avec

l'oxyde de sodium dans le scorie. Cela peut entraîner la formation de phases solides de faible densité telles que la néphéline, qui peuvent endommager le matériau réfractaire par expansion de volume. Parmi les trois réfractaires testés, la zircone mullite a donné la pire résistance à la corrosion, avec dissolution de la phase liante et pénétration complète de l'oxyde de sodium. Chromie corindon a donné la plus grande résistance à la pénétration des matériaux testés, bien qu'une certaine dissolution de la chromie dans le scorie soit encore évidente. Une étude plus approfondie des matériaux réfractaires à haute teneur en chrome est recommandée pour cette application.

Pour les applications minières, des eaux de résidus fins mûrs (RFM) combinées à une eau de traitement des sables bitumineux (TSB) ont été utilisées comme eau de procédé pour injection. En raison du liquidus élevé des dépôts inorganiques résultants, la co-injection d'un fluxant est recommandée pour réduire le liquidus et la viscosité de la solution de scorie résultante, maximisant ainsi l'efficacité de la chambre de combustion en réduisant la température d'opération requise. La dolomite a été identifiée comme le fluxant optimal, à une concentration de 20% en poids de $CaMgO_2$ dans le scorie fondu. Ce mélange s'est avéré avoir une viscosité d'un peu moins de 25 Pa·s à 1300 °C, ce qui en fait un bon point de fonctionnement pour la chambre de combustion PVCD, car le scorie fondu doit s'écouler librement et ne pas provoquer de colmatage. La résistance à la corrosion de plusieurs matériaux réfractaires candidats a été évaluée par modélisation et essais à l'échelle de laboratoire pour les scories fluxées et non fluxées. Semblable aux résultats pour le DGMV, parmi les réfractaires testés, le chrome corindon offrait la plus grande résistance à la pénétration, tandis que la zircone mullite était la plus profondément pénétrée par l'oxyde de sodium. Encore une fois, un réfractaire contenant du chrome est recommandé pour une étude plus approfondie pour l'utilisation dans la chambre de combustion PVCD. D'autres réfractaires

candidats étudiés dans les modèles qui justifient des essais sont le spinelle de chrome et le spinelle d'aluminate de magnésium. Pour les travaux futurs, d’autres essais de corrosion à plusieurs durées sont recommandés, ainsi que la caractérisation des échantillons réfractaires de l’usine pilote PVCD de CanmetÉNERGIE et la quantification des effets de l’exposition au scorie sur la résistance mécanique des matériaux réfractaires.

Acknowledgements

I would like to express my sincerest gratitude to my supervisor, Dr. Arturo Macchi, for his continuous support and professional insight throughout this work. His questions and feedback have made me a better researcher and helped me to think critically about the story I am trying to tell.

I would also like to thank many of my colleagues at CanmetENERGY Ottawa, without whom this research could not have taken place. First, Dr. Marc Duchesne, who provided valuable guidance on this project from conception, to execution, to analysis. Much of my own expertise is a result of his teachings, and I am grateful for his continued mentorship throughout my career. Second, Dr. Robin Hughes, who generously strives to help me become a better writer, think strategically, and propel me forward in my own professional development. Third, Dr. Bruce Clements, who advocated on my behalf to help ensure this thesis became a reality. Finally, I would like to thank the rest of the team at CanmetENERGY Ottawa, who were always willing to answer my questions and offer help, and who were always a source of encouragement.

I am grateful to my family and friends, who have stood by me, not only through graduate school, but through each and every challenge along the way. They have offered me patience, understanding and encouragement when I needed it most. They were the ones who instilled in me the confidence to attain my goals.

Finally, I would like to acknowledge the financial support of both the University of Ottawa and Natural Resources Canada for the completion of this research.

Table of Contents

List of Tables

List of Figures

Nomenclature

AALE	Average absolute logarithmic error
BET	Brunauer-Emmett-Teller
BJH	Barrett-Joyner-Halenda
CFD	Computational fluid dynamics
DCSG	Direct contact steam generation
EMPA	Electron probe micro-analysis
EDX	Energy dispersive x-ray
FWKD	Free water knockout tank discharge
GHG	Greenhouse gas
ICP-AES	Inductively coupled plasma atomic emission spectroscopy
MFT	Mature fine tailings
OPW	Oil sands processing water
OTSG	Once-through steam generator
RCW	Pond recycle water
SAGD	Steam assisted gravity drainage
SEM	Scanning electron microscopy
SLPH	Standard litres per hour
XRF	X-ray fluorescence

Chapter 1. Introduction

1.1 Motivation to develop direct contact steam generation

The oil and gas industry is a significant contributor to global CO_2 emissions, and thus there lies the motivation to improve process efficiencies and develop new technologies to reduce its environmental impact [1]. In Canada, the process is yet more CO_2 intensive because extracted bitumen requires upgrading before it can enter the market. There are two main methods employed to extract bitumen from the Canadian oil sands: (1) surface mining and (2) *in situ* extraction, such as steam assisted gravity drainage (SAGD) [2]. SAGD requires steam for injection into the wells, where the steam heats the bitumen, thereby reducing its viscosity and allowing it to be pumped to the surface. Upon arrival at the surface, the bitumen is separated from the water and sent for further treatment. The water is sent to a de-oiling treatment step, and then to a further process water treatment step to improve the water quality so that it can be re-used for steam generation [3]. Surface mining requires steam for, among others, the hot water extraction process that separates the mined bitumen from the sands and clays of the oil sands [4]. Oxy direct contact steam generation (DCSG) is considered herein as a means of producing steam for both of these oil sands applications, acting as a replacement for the traditional once-through steam generators (OTSGs).

CanmetENERGY-Ottawa's DCSG process is oxy-fired and operates under high pressure (up to 100 bar(g)). As shown in Figure 1-1, process water, oxygen and fuel are injected into the combustor, resulting in vaporization of the water upon combustion of the fuel. The steam and CO_2 mixture then passes to the quench, where additional process water is injected to cool the combustion products and increase the steam yield. Finally, the gases pass to the scrubber where particulates are removed and additional process water is injected to yield a product consisting of roughly 90 mol % H_2O, with the balance being primarily CO_2. When used for SAGD, the produced

CO_2 would be injected directly into the well with the steam. Approximately 80% of the CO_2 is expected to remain sequestered below ground, while the remainder will be contained within the extracted bitumen stream. The vapor separated from the extracted bitumen will be recycled back to the DCSG units and re-injected into the well, allowing the technology to achieve near-zero direct emissions [3].

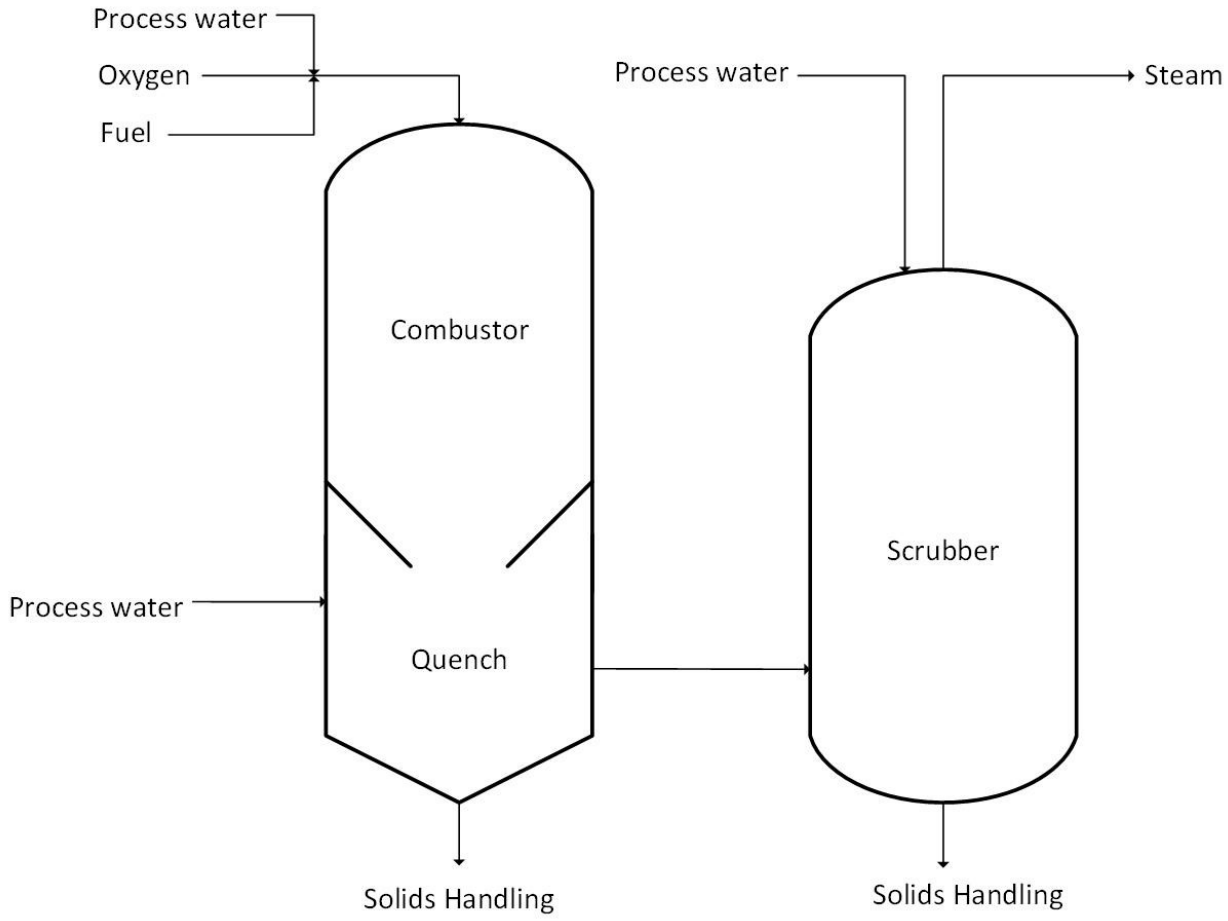

Figure 1-1. Schematic of CanmetENERGY-Ottawa's direct contact steam generation process.

DCSG offers many advantages relative to OTSGs. Due to the direct injection of water into the combustor, the risk of fouling of boiler tubes is avoided and water treatment steps can be eliminated. DCSG also offers an improved efficiency because there are no sensible heat losses from an emitted flue gas stream, since the flue gas is injected along with the steam product into

the well [3]. Other advantages include reduced (or eliminated, if using natural gas as the fuel) fresh water consumption, reduced greenhouse gas emissions, and reduced wastewater production [5]–[7].

Many kinds of oil sands processing waters or wastewaters can be considered for use in DCSG, though the presence of inorganic material in that water can have a heavy impact on how the process should be ran and what materials should be selected for the internals. The inorganics in the water can lead to deposits on internal surfaces, which in turn can cause corrosion, affect heat transfer, and, in severe cases, lead to plugging [8]. This is of particular importance to the combustor, which operates at elevated temperatures and is thus likely to accelerate the speed of corrosion. Developing an understanding of what phases may form in the combustor and how they may interact with potential refractory materials based upon specific process water applications is thus of utmost importance for continuous and reliable operation of the DCSG process.

1.2 Research objectives and scope

Two specific applications for DCSG and their respective process water compositions were considered in this work: SAGD and surface mining. Research focused on the evolution of and refractory interactions with inorganics within the combustor for the CanmetENERGY process. For both applications, the objectives of the research were as follows:

1. Establish expected compositions and properties of deposits in the combustor based on process water analyses and operating conditions.
2. Screen candidate refractory materials for the combustor through models of potential interactions between the deposits and the refractory.
3. Validate corrosion models and recommend a refractory material for the combustor through laboratory-scale corrosion tests.

4. Advise on any changes that may be required to the operating conditions of the DCSG combustor in order to improve reliability, maintainability and operability.

1.3 Thesis organization

This thesis is organized into 4 chapters, with the first being this introduction. Chapter two is a research article intended for publication that examines the use of free water knockout tank discharge from SAGD operations for injection to the DCSG combustor. Refractory selection in this case is based upon a high-Na_2O slag solution. Chapter three is a second research article intended for publication, which considers DCSG for surface mining applications. Mature fine tailings, in conjunction with another oil sands processing water as a diluent, is injected into the combustor in this case. In addition to refractory selection, this article highlights the challenges associated with operating with process water with such a high solids content, and proposes solutions. Finally, chapter four summarizes the conclusions of the research in relation to the research objectives.

1.4 References

[1] M. S. Masnadi *et al.*, “Title: Global carbon intensity of crude oil production,” p. 19.

[2] J. A. Bergerson, O. Kofoworola, A. D. Charpentier, S. Sleep, and H. L. MacLean, “Life Cycle Greenhouse Gas Emissions of Current Oil Sands Technologies: Surface Mining and In Situ Applications,” *Environ. Sci. Technol.*, vol. 46, no. 14, pp. 7865–7874, Jul. 2012, doi: 10.1021/es300718h.

[3] P. E. Cairns, “High Pressure Oxy-fired (HiPrOx) Direct Contact Steam Generation (DCSG) for Steam Assisted Gravity Drainage (SAGD) Application,” p. 128.

[4] J. Masliyah, Z. J. Zhou, Z. Xu, J. Czarnecki, and H. Hamza, “Understanding Water-Based Bitumen Extraction from Athabasca Oil Sands,” *Can. J. Chem. Eng.*, vol. 82, no. 4, pp. 628–654, 2004, doi: https://doi.org/10.1002/cjce.5450820403.

[5] P. E. C. Cairns *et al.*, “High-Pressure Oxy-Firing (HiPrOx) of Fuels with Water for the Purpose of Direct Contact Steam Generation,” *Energy Fuels*, vol. 29, no. 7, pp. 4522–4533, Jul. 2015, doi: 10.1021/ef502754h.

[6] J. Seaba, D. Wissmiller, and S. Alavandi, “Advanced Steam Generation: Technologies for Canadian Oil Sands,” Gas Technology Institute, 2017. Accessed: Apr. 30, 2020. [Online]. Available: https://www.cosia.ca/uploads/documents/id46/COSIA%20Advanced%20Steam%20Generation%20-%20Technologies%20for%20Canadian%20Oil%20Sands.pdf.

[7] M. Wolinetz, “DCSG Market Analysis,” Navius Research, 2013.

[8] J. Nakano, S. Sridhar, J. Bennett, K.-S. Kwong, and T. Moss, “Interactions of refractory materials with molten gasifier slags,” *Int. J. Hydrog. Energy*, vol. 36, no. 7, pp. 4595–4604, Apr. 2011, doi: 10.1016/j.ijhydene.2010.04.117.

Chapter 2. Direct contact steam generation for steam assisted gravity drainage: Inorganic phases and refractory corrosion in the combustor

2.1 Abstract

Oxy-direct contact steam generation (DCSG) is a means of producing high-pressure steam with significant reductions in greenhouse gas emissions and fresh water consumption. In this process, contaminated water can be directly injected into an oxy-fired combustor to produce steam without boiler tubes and their associated fouling risks. Free water knockout tank discharge, from oil sands processing, is investigated in this paper as a feedstock for DCSG in steam-assisted gravity drainage (SAGD) applications. In the combustor, this is predicted to result in the formation of a high Na_2O silicate slag, enriched with Na_2SO_4, and additionally at lower temperatures, a Na_2SO_4 rich molten salt. Based on material properties and the desire to avoid formation of the corrosive salt phase, a combustor wall temperature ranging from 1200 – 1250 °C in regions where inorganics will be contacting the wall is recommended for commercial operation. A series of refractory materials were evaluated by thermodynamic corrosion models using FactSage, and a subset by bench-scale cup and sessile drop corrosion tests, to recommend a refractory material for the combustor. Of the refractories tested, chromia-corundum offered the greatest resistance to penetration by slag and salt, but there was some dissolution of chromia in the bulk slag layer. On the other hand, a mullite-zirconia refractory was severely affected by the slag, with dissolution of its alumina-silica binder phase, mobilization of zirconia grains, and deep penetration by Na_2O. There was evidence of nepheline formation in the aluminosilicate binder phases of both mullite-zirconia and silicon carbide-based refractories as a result of reaction with the sodium in the slag. Nepheline is a low density solid that can cause damage to the refractory through volume expansion. Aluminosilicate-based refractory materials should thus be avoided, whereas a high chrome refractory material such

as chromia-corundum is recommended for further investigation. A magnesium aluminate spinel or a chromia spinel also warrant testing due to their expected corrosion resistance from the models.

2.2 Introduction

Oxy-direct contact steam generation (DCSG) can produce high pressure steam for Canadian oil sands operations with a significant reduction in greenhouse gas (GHG) emissions and fresh water consumption. CanmetENERGY Ottawa is currently developing the technology at the pilot scale. Its application for steam-assisted gravity drainage (SAGD) is considered herein, though this process can apply to many applications in which large quantities of steam are used [1]. Currently the extraction of Canadian bitumen is a GHG- and energy-intensive process. Replacement of once-through steam generators with DCSG for *in situ* oil extraction can reduce GHG emissions by 33-70 % depending on the source of electricity, reduce the overall energy intensity of the process, reduce feed water treatment requirements, eliminate wastewater production, and reduce fresh water consumption by 50-100% [2]–[4].

Input streams to the DCSG combustor are oxygen, fuel and untreated process water. The process water directly contacts the flue gas and is vaporized by the heat of combustion. After quenching and scrubbing for inorganics removal, the process outputs a high pressure, slightly superheated, stream consisting of approximately 90 mol % H_2O, with the balance being principally CO_2. For SAGD, this stream can be injected directly into the well, resulting in a predicted sequestration of 80% of the CO_2 [2]. After steam injection, the bitumen and water pumped from the well require separation. In some cases, a diluent is added to the bitumen to reduce its density, thereby allowing it to float on water. The water remaining after this gravity separation is termed free water knockout tank discharge (FWKD), and is investigated herein for use as the process water for DCSG [5].

The impact of inorganic species in the water on the combustor is a key challenge to address in the development of this technology. These inorganic species can accumulate on surfaces, affecting heat transfer and corrosion mechanisms. They further can form liquid phases (slag and molten salts) that can cause wear of refractory materials through mechanisms such as chemical corrosion, mechanical erosion and spalling [6].

A first step in refractory selection is modelling and characterization of the liquid phases produced in the combustor. The composition of the liquid phases affects how they will interact with other materials. As a rule of thumb, the acidity or basicity of a slag should be likewise matched with an acidic or basic refractory material, respectively [7]. For a silicate-based slag, the base-to-acid ratio can be calculated using the molar fractions of each species in the mixture according to Equation 1. Basic species are defined as those that are capable of donating oxygen, while acidic species can accept oxygen [8].

$$\frac{Base}{Acid} = \frac{Na_2O + K_2O + CaO + MgO + FeO}{SiO_2 + Al_2O_3 + Fe_2O_3 + TiO_2} \qquad \textbf{Equation 1}$$

Understanding the liquid properties such as surface tension, viscosity and contact angle are important when modelling and understanding how a solution will interact with potential refractory materials. The relationship between these factors is explained by Equation 2, developed by Lee and Zhang from Poiseulle's Law. Here, l is the liquid penetration depth into the refractory, r is the pore radius of the refractory assuming linear pores, θ is the contact angle of the liquid on the refractory, γ and η are the liquid surface tension and dynamic viscosity, respectively, and t is the time [7]. From this relationship, it is evident that liquid phases with a higher surface tension and lower viscosity have a greater potential to penetrate a refractory material.

$$l^2 = \frac{r\cos(\theta/2)\gamma t}{\eta} \qquad \textbf{Equation 2}$$

This work estimates the composition of inorganic deposits resulting from injection of FWKD into the combustor and elucidates their interactions with potential refractory materials to inform selection of an appropriate refractory for DCSG combustors. The high alkali content of the water results in a unique slag composition compared to coal combustion or gasification slags or metallurgical slags. Careful material selection is thus key to the technology's success to prevent costly shutdowns necessary for refractory replacement. Refractory corrosion is assessed by modelling two corrosion mechanisms: (1) slag penetration through cracks and pores and (2) dissolution of refractory in the slag. Modelling is supported with liquid phase property measurement and bench-scale corrosion tests.

2.3 Materials and Methods

2.3.1 Process water and refractory materials

A representative water sample from a SAGD facility in the Canadian oil sands (FWKD) was obtained and analyzed. Any hydrocarbons within the water were assumed to be converted to CO_2 and H_2O upon injection to the DCSG combustor, and thus were not considered in the analysis for this work. Table 2-1 shows the analysis of the major inorganic species, i.e., species representing ≥ 1 wt. % of total inorganics, contained within the FWKD.

Table 2-1. ICP-AES analysis of major inorganic species (excluding O and C) in FWKD.

Species	Wt %
B	4.1
Cl	17.0
K	3.9
Na	42.3
S	8.0
Si	21.8
Total inorganics (mg/kg water)	488

The composition of the refractory materials used for simulation and testing are given in Table 2-2. Samples of R1-R3 were obtained from manufacturers as pre-cast blocks of 0.1m x 0.1m x 0.1m in size. As required, samples pieces were cut using a wet saw or bored using a radial drill press. Cutting dust was rinsed away with water and samples were dried at ambient conditions before experiments commenced.

Table 2-2. Composition of refractory materials for modelling and experimental testing.

Refractory Material:	**Mullite-zirconia[1]**	**Silicon carbide[2]**	**Chromia corundum[3]**	**Spinel[4]**	**Corundum with TiO_2[5]**	**Chromia with P_2O_5[6]**	**Chromia spinel[6]**
Refractory ID:	**R1**	**R2**	**R3**	**R4**	**R5**	**R6**	**R7**
Component				**Wt %**			
Al_2O_3	51.3	20.6	24.7	64.7	97.5	4.7	
SiO_2	21.3	14.7	0.2				
ZrO_2	19.5						
SiC	3.9	62.1					
CaO	1.5	2.2	0.1				
MgO				35.3			17.4
Cr_2O_3			74.8			92.0	82.7
TiO_2	0.4				2.5		
Fe_2O_3		0.2	0.1				
P_2O_5						3.3	
Alkalies	1.5	0.2					
Other	0.3		0.1				

[1]Composition provided by manufacturer [9].
[2]Composition given by manufacturer [10].
[3]Composition provided by manufacturer [11].
[4]Composition given by Carlborg et al. excluding species <1 wt % [12].
[5]Composition given by Reinmöller *et al.* excluding species <1 wt % [13].
[6]Composition given by Bennett *et al.* excluding species <1 wt % [14].

2.3.2 Thermodynamic simulations

All thermodynamic simulations were completed using the Equilib module of FactSage version 7.0-8.0 [15]. All gases, pure solids and solution phases in the FactPS, FToxid and FTpulp databases were considered. When sulphur was present, the SLAGB solution phase was considered to incorporate sulphur as SO_4^{2-} in the slag; otherwise SLAGA was used. The MELTA solution phase

of the FTpulp database was selected to provide the best optimized thermodynamic solution for the major phases identified within the salt, when present.

2.3.2.1 Deposition models

The composition and quantity of inorganic phases forming in the combustor were modelled using flow rates determined by a simulation constructed in Aspen HYSYS to target a bulk combustor temperature of 1250 °C. On a basis of 1000 kg/h of FWKD (including species described in Table 2-1), other required feeds to the combustor are 124 kg/h of natural gas (97 mol % CH_4, 2 mol % C_2H_6, 1 mol % C_3H_8) and 494 kg/h of oxygen. These inputs were combined in FactSage at a temperature of 1250 °C and a pressure of 55 bar(g) (base case conditions). Computational fluid dynamics (CFD) models performed by CanmetENERGY-Ottawa (methodology explained in [16]; results shown in Figure 2-S1) showed that the wall temperature of the combustor in regions where inorganics are expected to contact the wall can range from 1075 to 1600 °C under base case conditions. The effect of temperature on the deposition composition was explored in FactSage at these two boundary temperatures, maintaining pressure at 55 bar(g). Pressure was then varied to 30 and 80 bar(g) at the base case temperature to establish its effect on the deposits. All other simulations in this work were performed within a subset of these discrete conditions.

2.3.2.2 Molten slag and/or salt penetration models

Simulation of molten slag and/or salt penetration into refractory materials was performed using a method previously described by Reinmöller *et al.* [13] with some modifications. In short, a step-wise approach was taken in which 100g of the molten slag and/or salt solution(s) (originally added in the proportions predicted in the deposition models) were combined with pure refractory material, starting with 100 g and then incrementally adding 20 g of refractory for each subsequent step. The consequent molten slag and/or salt composition prediction(s) from the previous step were used as the input for the subsequent step. Calculations proceeded for 15 calculation steps (resulting

in an addition of 380 g of refractory to 100 g slag and/or salt in the final step) or until no slag and/or salt solution remained, whichever occurred first. All simulations were carried out at 55 bar(g) and assumed isothermal conditions. At step 1, an oxygen partial pressure of 0.072 bar(a) was specified to represent the gaseous environment in the combustor. For subsequent steps, the partial pressure of oxygen was assumed to be more locally governed by the high amount of oxygen in the oxides of the slag and refractory, and thus was left unspecified for FactSage to calculate based upon the mass of each species inputted.

2.3.2.3 Refractory dissolution modelling

Refractory dissolution in the modelled slag phases was performed by estimation of the metastable diffusion factor, as described by Duchesne *et al.* [17]. Since the refractory materials are heterogeneous, analysis was done on individual phases within them that are expected to represent ≥ 10 wt % of the total refractory. The phases present in the refractory were estimated in FactSage using the refractory composition in Table 2-2 and the temperature and pressure of interest. Values of slag viscosity used to calculate the diffusion factor were those measured at the temperature of interest as described in Section 2.3.5. Note that diffusion factors could not be estimated for chromia-containing refractories because the SLAGB database used in FactSage, which is necessary to represent the Na_2SO_4 contained within the slag, does not include chromia.

2.3.3 Slag viscosity modelling

For slags that did not contain Na_2SO_4, all viscosity models in the Slag Viscosity Modeling Toolbox [18] were considered. The most appropriate model for each slag composition was determined by comparing the model's predictions to a range of measured viscosity values in literature that were similar in composition to the modelled mixture. The viscosity model that minimized the average absolute logarithmic error (AALE) was then applied to make the predictions. For slags that

contained Na_2SO_4, the Priven-2000 model [19] was used, since none of the other models consider Na_2SO_4 as a component.

2.3.4 Synthetic slag/salt preparation

All viscosity and corrosion tests were completed using synthetic preparations of the selected slag or salt solutions predicted by the deposition models. Note that for slags tested at 1250 °C or above, the powder preparations excluded Na_2SO_4 for safety reasons, to avoid the release of SO_x gases into the laboratory. Na_2CO_3, K_2CO_3, SiO_2, Na_2SO_4, Na_2CO_3, NaCl and K_2SO_4 powders (Sigma Aldrich) were combined such that the compositions met the targets following thermal decomposition of the carbonates and consequent release of CO_2 (hereafter referred to as de-gassing). Powders were mixed for 4 hours in a shaker mixer (Turbula Type T2 F).

2.3.5 Viscosity tests

Viscosity tests were conducted using the rotating bob method with alumina crucibles, alumina spindles and a continuous supply of air (62 SLPH). To limit contamination of the sample by the alumina crucibles (<2 wt % increase in Al_2O_3), the amount of time the sample spent at high temperatures (>1000 °C) was minimized. This method was validated through measurement of the composition of a post-test sample using x-ray fluorescence (XRF) as per ASTM D4632. The slag viscosity measurement device at CanmetENERGY-Ottawa has been previously described [20]. Approximately 130 g of synthetic slag powder was heated to 1000 °C overnight to allow the sample to equilibrate and de-gas. The next day, samples were heated to the maximum test temperature (either 1075 or 1250 °C) and left to equilibrate for a further 45 minutes. Viscosity measurements were then taken at 25 °C temperature decrements, allowing the sample to equilibrate at the target temperature for 10 minutes prior to each measurement, until the viscosity was ≥ 300 Pa·s. At each temperature point, the viscosity readings were allowed to stabilize, and then 3 measurements were taken at a high torque (roughly 80% of the instrument's maximum

measurement limit). The rotational speed was then halved, the measurements were allowed to stabilize, and 3 measurements were taken at a lower torque. Finally, the rotational speed was returned to the original speed, the readings were allowed to stabilize, and a final set of 3 measurements were taken. This was done to detect non-Newtonian behaviour, which would present as a difference (here taken to be >10 %) in average viscosity at different torques. If non-Newtonian behaviour was not detected, the viscosity reported was the average of all 9 measurements.

2.3.6 Refractory corrosion tests

Prior to corrosion tests, synthetic slag samples were degassed in an oven at 1050 °C in a platinum dish to remove CO_2. Dishes were manually agitated by swirling and tapping the dish every 30-45 minutes to free trapped bubbles and then returned to the oven. After 3 cycles of heating and agitation, samples were left to cool to room temperature and then weighed to ensure all CO_2 was removed. Degassed samples were then removed from the dish.

2.3.6.1 Cup tests

Cup tests were performed according to Method A in standard CEN/TS 15418:2006 [21] in air. De-gassed slag (60 g) was placed in each refractory cup and heated in a muffle furnace (Thermolyne F46240CM-33) to the target temperature at a rate of 15 °C/min. The temperature was held for a period of 5 hours. Samples were then cooled in the furnace at a rate of no greater than 20 °C/min.

2.3.6.2 Sessile drop tests

Approximately 0.15 g of powdered salt or de-gassed slag was used for these experiments. The salt was prepared by pressing it into a 6 mm diameter pellet under a force of 15.6 kN using a Carver manual press (model #4555.L). The initial slag sample was in the form of a glassy fragment following de-gassing and was used as-is. The slag or salt sample was placed on a square segment of refractory material approximately 15 mm x 15 mm in width and length, and 10 mm in height.

The refractory material was then placed onto a 25.4 mm diameter alumina disk and loaded into a tensiometer furnace. The equipment has been previously described [22]. Samples were heated to the target temperature under a continuous flow of air (115 gas changeovers per hour at standard conditions) and held for a period of 4 hours before cooling back to room temperature. A video was captured throughout the test to qualitatively assess the wettability of the refractory materials by the slag and salt solutions (due to sample spreading and spillover and/or reaction with the refractory causing bubbling, the contact angle could not be quantified).

2.3.6.3 Scanning electron microscopy and electron probe microanalysis (SEM-EPMA)

Following corrosion tests, cup test samples were cross-sectioned using a wet saw and then further cut to a suitable size using a Buehler IsoMet low speed saw. Sessile drop samples were cross-sectioned directly with the Buehler saw. Samples were cast into 25 mm diameter epoxy pucks and cleaned by sonication first in dish soap, and then in distilled water. Pucks were polished with a Buehler Power Pro 5000 and water-based diamond polish (6 µm, 3 µm and 1 µm solutions), and then carbon coated. Cross-sections were visualized and analyzed using a JEOL 8230 SuperProbe. A quantitative elemental composition was obtained for each point on the surface chosen for analysis. Line scans perpendicular to the slag-refractory interface were done with 50 µm spacing between points near the slag-refractory interface (the first 2-3 mm), and then at a spacing of 200-590 µm to traverse the remaining distance in the cross-section. Measured elements (and their calibration standards) were: K (sanidine), Ca (Diopside), Na (albite), Al (corundum), Si (zircon), Cr (chromite), S (celestine), Zr (zircon), Fe (hematite), Ti (Rutile), Hf (zircon) and Cl (vanadinite).

2.4 Results and Discussion

2.4.1 Deposition Models

Though the target bulk gas temperature is 1250 °C, the wall temperature of CanmetENERGY's pilot-scale DCSG combustor in the region where solids are expected to impact it is estimated to

range from 1075 to 1600 °C, depending on the proximity to the flame. Variation in wall temperature for the commercial combustor will depend on geometry and firing rate, however studying the range stated above is believed to be wide enough to inform commercial operation. It was assumed that inorganics adhering to the combustor wall reached equilibrium at that local wall temperature. The predicted compositions of the molten solutions forming in the combustor are shown in Figure 2-1 as a function of wall temperature. No solids were predicted in any of these cases. At all temperatures considered, formation of a silica-based slag that contains significant amounts of alkali oxides (> 8 wt %) was predicted. As the temperature decreased, increased amounts of Na_2SO_4 in the slag were predicted, along with a second distinct liquid phase – a molten salt rich in Na_2SO_4. At 1075 °C, the salt phase represents 20 wt % of the total inorganic phases, with the slag making up the balance. The transition wall temperature below which the salt phase is predicted to start forming is 1198 °C.

The modelled slag compositions are unique compared to typical power plant and metallurgical slags, particularly in the presence of Na_2SO_4 and high fraction of Na_2O. This difference thus creates uncertainty when selecting refractories for DCSG combustors. In selecting refractories, it may be appropriate to use biomass ash as an analogue, which also has a high alkali content, but typically potassium is the dominant alkali [12], [23]–[25]. High alkali content has been associated with problems such as corrosion and fouling of both metals and refractory components [25], [26].

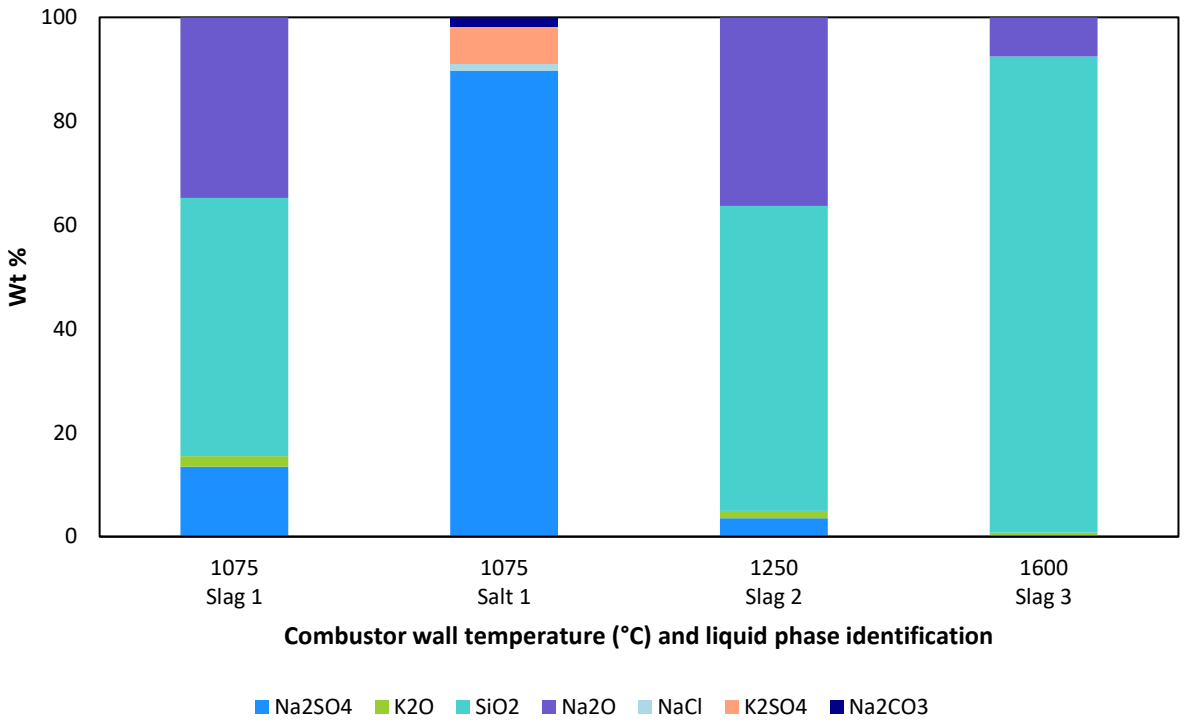

Figure 2-1. Effect of combustor local wall temperature on the composition of liquid phases at 55 bar(g).

Pressures ranging from 30 to 80 bar(g) were investigated in this work for commercial operation of the DCSG facility. Changes to the combustor pressure are shown to have very little effect on the composition of the liquid phases forming, with the exception of Na_2SO_4 (Figure 2-2). The concentration of Na_2SO_4 in the slag increased 7-fold between 30 and 80 bar(g), ranging from 1-7 wt %. This change, however, is already encompassed within the larger variation (0-13.5 wt %) of Na_2SO_4 concentration predicted in the 1075 – 1600 °C temperature range at constant pressure. Thus, by focussing on liquid properties predicted in Figure 2-1 at a moderate pressure for the experimental work in the remainder of this study, the full potential variability in the composition of the slag solution was captured.

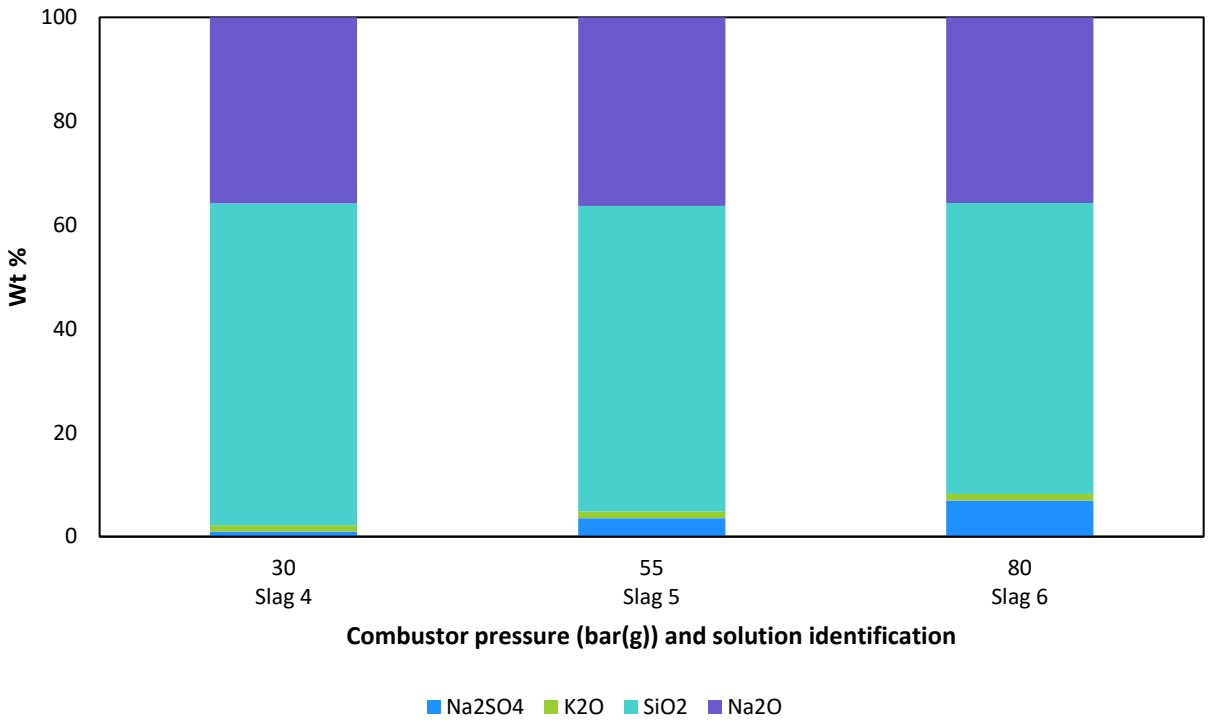

Figure 2-2. Effect of combustor operating pressure on the composition of the liquid phases at 1250 °C.

2.4.2 Liquid Phase Properties

Measurement of the surface tension and density of the slag and salt solutions are presented in Figure 2-S2 and Figure 2-S3, while viscosity results are presented below. There is not a significant amount of published data on the viscosity of slags containing high amounts of sulfur, particularly in the form of Na_2SO_4, nor with slags with such a high Na_2O content. Only one viscosity model, by Priven, could be identified that considered Na_2SO_4 as a constituent [19], but its range of validity did not extend to the 13.5 wt % Na_2SO_4 contained within Slag 1 (Figure 2-1) and its accuracy for the presented slag compositions is unknown. One other viscosity model, by Riboud, was identified that allows SO_3 concentrations of up to 5 wt % as an impurity, but does not use it as an input when calculating the viscosity [8], [18].

The effect of Na_2SO_4 in the slag on the solution's viscosity was investigated through slag viscosity modelling and measurement (Figure 2-3). The maximum temperature at which each slag was

measured represents the temperature at which that slag was predicted to form in the combustor in Section 2.4.1. The Priven-2000 model provides a good estimate for the measured viscosity of Slag 2. For Slag 1, the Na_2SO_4 content exceeds the model limits, and it was not possible to calculate a viscosity prediction outside of those limits. For this reason, the Priven model was applied on a Na_2SO_4-free basis for Slag 1, and is shown to overestimate the measured viscosity of the Na_2SO_4-containing slag.

If one re-calculates the composition of each of Slag 1 and Slag 2 to exclude Na_2SO_4, a similar composition is obtained in both cases (Na_2O and SiO_2 concentrations within 3.5 wt % and K_2O concentrations within 1 wt %). The Priven models for Slag 1 and Slag 2 were both calculated for these Na_2SO_4-free slag compositions, thereby showing that the minor compositional changes in Na_2O, K_2O and SiO_2 reduce the viscosity of Slag 1 relative to Slag 2 by 43-52 % in the temperature range of 850-1075 °C. By comparison, the experimental viscosity values for Slag 1 are reduced by 77-80 % relative to Slag 2 in the same temperature range. Since the reduction in viscosity is greater than predicted by the models for the changes in the other constituents, the addition of Na_2SO_4 is likely the cause of the additional decrease in the measured viscosity of Slag 1 compared to Slag 2. It can thus be hypothesized that Na_2SO_4 acts as a network modifier in glassy slags, much as Na_2O does, leading to depolymerisation of the silicate structure [27]. This can have a negative effect on the combustor, as a decreased slag viscosity facilitates slag penetration through cracks and pores and has the potential to increase the rate of dissolution of the refractory [7].

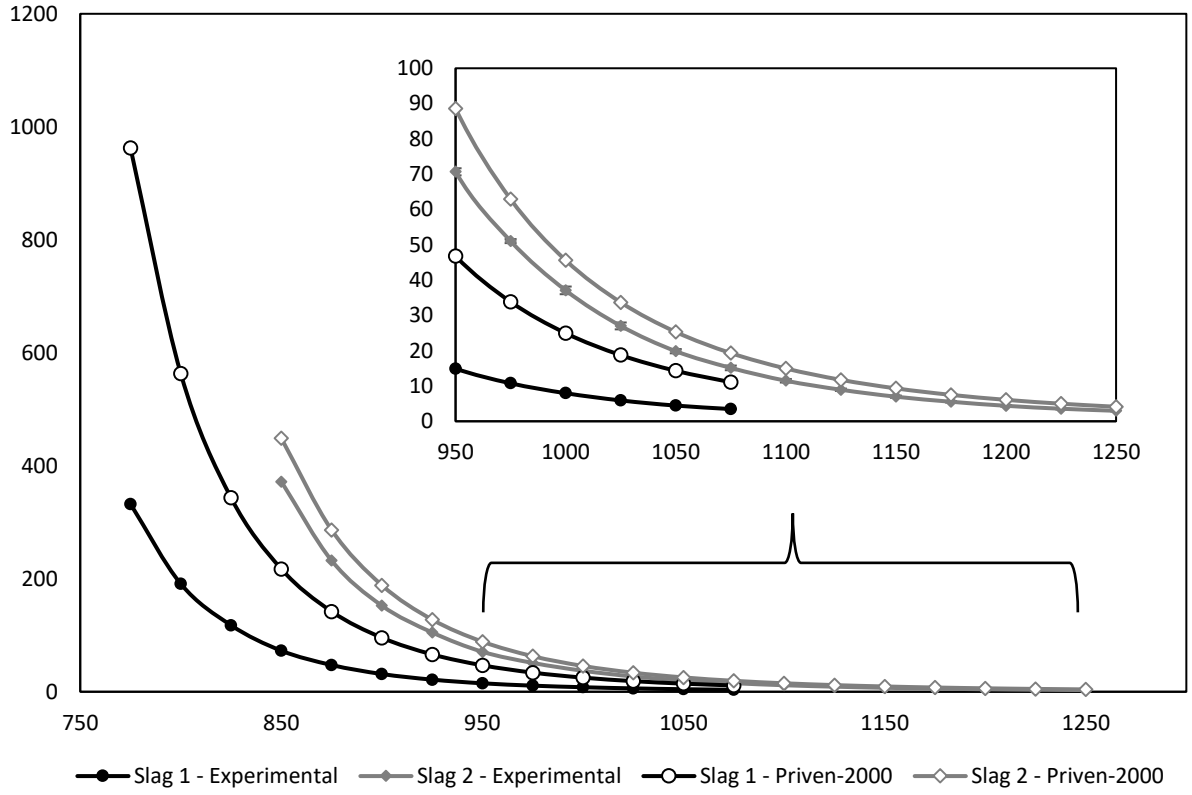

Figure 2-3. Average and modelled (Priven-2000 [19]) viscosity of synthetic preparations of Slag 1 (13.5 wt % Na_2SO_4) and Slag 2 (prepared on Na_2SO_4-free basis) in air at atmospheric pressure. Data points are the average of 9 repeat measurements, with a coefficient of variation ≤ 5 %. Viscosity estimates for Slag 1 exclude Na_2SO_4 because the wt % of Na_2SO_4 exceeds model limits.

A common heuristic advises targeting a slag viscosity of 2.5-25 Pa·s at the slag tap [17], [27]. This is a balance between having a low enough viscosity to prevent accumulation and plugging in the vessel, and having a slag that flows too quickly and causes erosion of the vessel internals. A temperature gradient exists along the length of the DCSG combustor, being hottest in the upper region near the flame, and coldest in the lower region approaching the slag tap into the quench. Simulations with FactSage modelled the cooling of Slag 1 and Slag 2 down to 1000 °C (the expected wall temperature at the pilot plant combustor outlet in Figure 2-S1) and verified that once the liquid phase forms in the combustor, its composition can be considered invariant as it flows down the walls through cooler regions of the combustor. For Slag 1 and Slag 2 to have a viscosity

of 25 Pa·s, this would require a minimum temperature at the slag tap for the commercial combustor of approximately 925 and 1025 °C, respectively.

2.4.3 Refractory corrosion models

Based on criteria presented by Vargas *et al.*[8], Slags 1-3 are all acidic despite the significant proportion of Na_2SO_4. This leads one to hypothesize that acidic or neutral refractories such as those based on SiO_2, Al_2O_3, and Cr_2O_3 would offer the greatest resistance to chemical attack by the FWKD slags. Given the results of the corrosion (penetration and dissolution) models below, the choice of refractory material is not as straightforward as this, likely due to the significant proportion of alkali in the mixture.

Simulations of refractory interactions with Slag/Salt 1 were performed at 1075 °C, with Slag 2 at 1250 °C, and with Slag 3 at 1600 °C. Table 2-3 shows a summary of the phases that may form over the course of penetration of the liquid phases within a number of refractory materials, while Table 2-4 shows the propensity of a particular phase to be dissolved by a slag through estimation of a diffusion factor. Diffusion factors could not be estimated for chromia-containing refractories since the SLAGB phase in FactSage's FToxid database does not consider chromia as a slag component. The slag penetration and dissolution models, as well as the changing composition and viscosity of the liquid phase throughout penetration, should be considered when screening potential refractory materials for corrosion resistance.

In the slag penetration models (Table 2-3), a key concern is the formation of new solid species that are lower in density than the refractory material, as this can cause damage to the refractory through volume expansion [12], [28]. Phases such as nepheline, feldspar, high albite and trydymite are all lower in density that the bulk phases of the refractory materials, and are expected to form upon reaction of the slag with a number of the refractory materials considered (R1, R2, R3 and R6). If

these phases form only at the surface, they have the potential to be protective by sealing off cracks and pores against further attack, but if they continue to form deeper into the material, as shown in Figure 2-4 with R1, this can severely reduce the lifetime of the refractory. Phases forming as a function of penetration depth for all other combinations of slag/salt and refractory materials considered can be seen in Figure 2-S4.

Alumina-based refractory materials (such as R5) have previously been shown to have poor corrosion resistance to high-alkali slags, becoming almost completely dissolved and severely deformed during the test period [12]. Alumina refractories have also been found to suffer greater dissolution with increasing concentration of Na_2O in the slag [29]. This is reflected in the high metastable diffusion factor calculated for R5 in Table 2-4. It has been previously reported that metastable diffusion factors greater than 100 K/Pa·s correlated to severe dissolution of the refractory under experimental conditions, while refractories with values less than 50 K/Pa·s were negligibly affected [17]. These results suggest that R1, R4 and R5 will be most susceptible to dissolution. R2 may offer a greater resistance due to the lower metastable diffusion factor of its the silicon carbide phase, which forms the largest proportion of that refractory material.

Based on slag penetration and dissolution models, and consultation with available literature on alkali-resistant materials [7], [12], [30], R3 and R7 (chromia based refractories), R2 (silicon carbide based) and R4 (magnesium aluminate spinel) may offer good corrosion resistance to FWKD-derived slags. The predicted viscosities of the slag solution as it reacts with and penetrates these refractories is presented in Figure 2-5. In many cases, Na_2SO_4 was eliminated from the slag upon reaction with the refractory material, allowing viscosity models other than the Priven-2000 model to be used to best suit the reacted slag composition. In the case of R2, it is believed that a protective silica layer may form at the refractory surface from passive oxidation of the silicon

carbide [30]. It also shows the sharpest increase in viscosity upon reaction with the refractory, which will decrease its ability to penetrate the refractory. Likewise, dense spinel phases like those predicted to form with R4 and R7 may also have protective effects, sealing off the refractory from further attack [7], [12]. The predicted viscosity of Slag 1 reacted with R4 remains low throughout penetration (<30 Pa·s) but beyond a refractory:slag ratio of 1.6 g/g the composition of the slag phase remains constant, indicating no further reaction with the refractory material. Slag penetration models with R3 led to rapid disappearance of molten slag or salt phases, suggesting that the slag-refractory interface may seal off quickly with formation of solids and also prevent deep slag/salt penetration into the refractory.

It is important to note that the penetrating slag compositions for R3 and R7 do not consider the addition of Cr_2O_3 to the slag, because this component was not included in FactSage's SLAGB database. It is likely that some Cr_2O_3 will be dissolved in the slag. Researchers have found that increasing Cr_2O_3 content tends to increase slag viscosity for silicate melts [31]–[34], though in one case with a SiO_2-Al_2O_3-CaO-Cr_2O_3 slag the effect was the opposite [35]. An increase in the reacted slag viscosity would further improve the resistance of the refractory material to penetration.

Table 2-3. Phases formed with the step-wise slag penetration simulations at 55 bar(g). New phases that are not predicted in the untreated refractory material at equilibrium at the temperature of interest are indicated in red. The formation of a gas in the first calculation step is excluded, since O_2 was added to the first mixture to reach the desired partial pressure (P_{O2} = 0.072 atm).

Refractory:			**R1**	**R1**	**R1**	**R2**	**R3**	**R4**	**R5**	**R6**	**R7**
Slag:			**1**	**2**	**3**	**2**	**2**	**2**	**2**	**2**	**2**
Salt:			**1**[1]	-	-	-	-	-	-	-	-
Temperature (°C):			**1075**	**1250**	**1600**	**1250**	**1250**	**1250**	**1250**	**1250**	**1250**
Phases Formed	**Chemical Formula**	**State**[2]									
Slag	-	ls		**X**	X	**X**	**X**	**X**	**X**	**X**	**X**
Salt solution	-	ls	**X**	**X**		**X**		**X**		**X**	**X**
Gas	-	g	**X**								
Chromia	Cr_2O_3	s									X
Chromium oxide	CrO_2	s					**X**			**X**	
Rutile	TiO_2	ss							X		
Corundum	M_2O_3	ss					X		X	X	
Beta-alumina	$NaAl_9O_{14}$	s							**X**		
Spinel	$Mg(Al,Cr)_2O_4$	ss						X			X
Magnesium oxide	MgO	s						X			
Silicon carbide	SiC	s			X	X					
Zirconia - monoclinic	ZrO_2	s	X								
Zirconia - tetragonal	ZrO_2	ss		X	X						
Mullite	$Al_6O_{13}Si_2$	ss		X	X						
Forsterite	$MgSiO_4$	s						**X**			
Disodium tricalcium aluminum oxide	$Na_2Ca_3Al_{16}O_{28}$	s	**X**								
Sodium aluminate	$NaAlO_2$	ss						**X**	**X**		
Feldspar	$(K,Na,Ca)(Al,Si)_4O_8$	ss				**X**				**X**	
Sodium chromate	Na_2CrO_4	ls					**X**			**X**	**X**
Nepheline	$Na_3KAl_4Si_4O_{16}$	ss	**X**	**X**		**X**	**X**		**X**	**X**	
High albite	$NaAlSi_3O_8$	s				**X**				**X**	

Refractory:			**R1**	**R1**	**R1**	**R2**	**R3**	**R4**	**R5**	**R6**	**R7**
Slag:			**1**	**2**	**3**	**2**	**2**	**2**	**2**	**2**	**2**
Salt:			**1**[1]	**-**	**-**	**-**	**-**	**-**	**-**	**-**	**-**
Temperature (°C):			**1075**	**1250**	**1600**	**1250**	**1250**	**1250**	**1250**	**1250**	**1250**
Phases Formed	**Chemical Formula**	**State**[2]									
Berlinite - D	$AlPO_4$	s								X	
Trisodium monophosphate - beta	Na_3PO_4	s								**X**	
Sodium sulfate	Na_2SO_4	l					**X**			**X**	
Sodium triphosphate	$Na_5P_3O_{10}$	s								**X**	
Tridymite	SiO_2	s								**X**	
Graphite	C	s				**X**					
Silicon sulfide	SiS	s				**X**					
Sodium silicon phosphorous oxide	$Na_{18}Si_6P_4O_{31}$	s								**X**	
No. calculation steps completed:			11	2	15	2	2	15	15	5	15

[1]Slag 1 = 80.4 g; Salt 1 = 19.6 g as inputs to Step 1 to reflect the same ratio at which slag and salt form in the deposition models at 1075 °C and 55 bar(g).

[2] s: pure solid; l: pure liquid: g: gas; ss: solid solution; ls: liquid solution

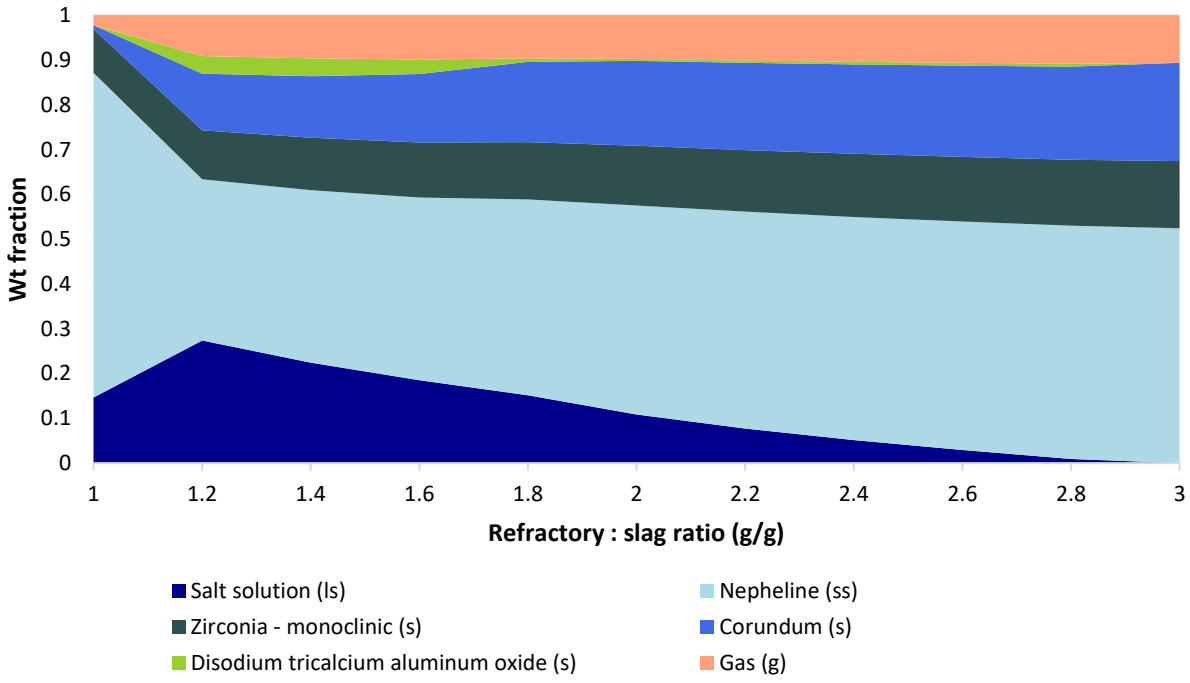

Figure 2-4. Phases formed during the stepwise addition of Slag 1 and Salt 1 to R1 at 1075 °C and 55 bar(g).

Table 2-4. Predicted diffusion factors of major refractory phases in slag solutions. Phases representing <10 wt % of the refractory were not considered. Values are reported for initial contact between pure slag and pure refractory.

Slag	Temperature (°C)	Refractory	Refractory Phase	Wt % Phase	Slag viscosity (Pa·s)	Metastable diffusion factor (K/Pa·s)
Slag 1	1075	R1	Mullite	67.4	3.47	219
			Zirconia	20.0	3.47	0.560
Slag 2	1250	R1	Mullite	68.3	3.02	310
			Zirconia	20.0	3.02	1.80
		R2	Silicon carbide	63.2	3.02	5.90
			Mullite	19.8	3.02	310
			Corundum	17.1	3.02	239
		R4	Magnesium aluminate spinel	90.1	3.02	210
		R5	Corundum	97.5	3.02	239
Slag 3[1]	1600	R1	Mullite	63.9	24.7	22.2
			Zirconia	19.5	24.7	1.04

[1]Viscosity values for this slag were calculated using the Lakatos model [18] instead of experimentally determined values.

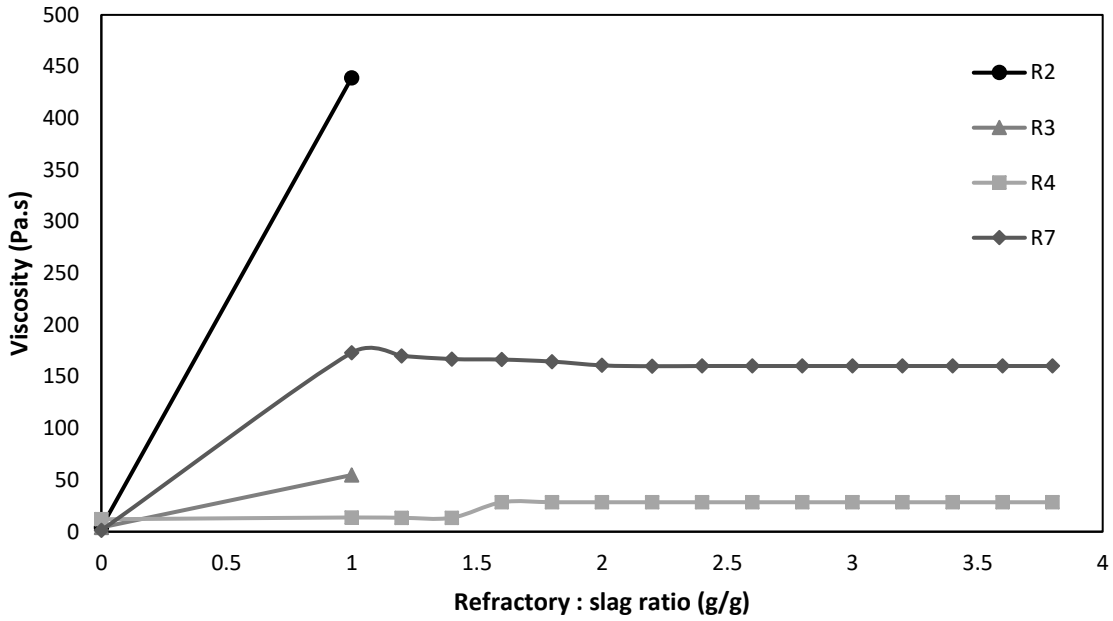

Figure 2-5. Predicted viscosity of Slag 2 as it reacts with and penetrates various refractory materials at 1250 °C and 55 bar(g). Applied viscosity models: Priven-2000 for R2 and R3, Urbain for R4 and Duchesne model for R5 [18], [19]. The effect of chromia was not considered for R3 and R7 because its concentration in the slag could not be estimated using FactSage's FToxid-SLAGB database.

2.4.4 Refractory corrosion tests

2.4.4.1 Baseline analysis of refractory materials

Three refractory materials (R1, R2 and R3) were obtained for laboratory testing. To establish the background concentration of each element of interest in the refractory materials and identify the individual phases within the bulk material, untreated refractories were first analyzed by EPMA. SEM images of each refractory are presented below in Figure 2-6, while the composition of identified points are given in Table 2-5. R1 consists of an aluminosilicate binder phase with individual alumina, zirconia and silicon carbide grains. R2 likewise has an aluminosilicate binder phase with larger interspersed silicon carbide grains. R3 has an alumina-chromia binder phase with high-chromia grains. The pore size of each refractory was characterized (Figures 2-S5 to 2-S7, and Table 2-S1) and showed that R2 had the greatest average Barret-Joyne-Halenda (BJH) pore size

(4V/A) and greatest cumulative pore volume. The interconnected pores in both R1 and R2 were larger in width that those in R3, based on SEM analysis (Figure 2-S7).

A)

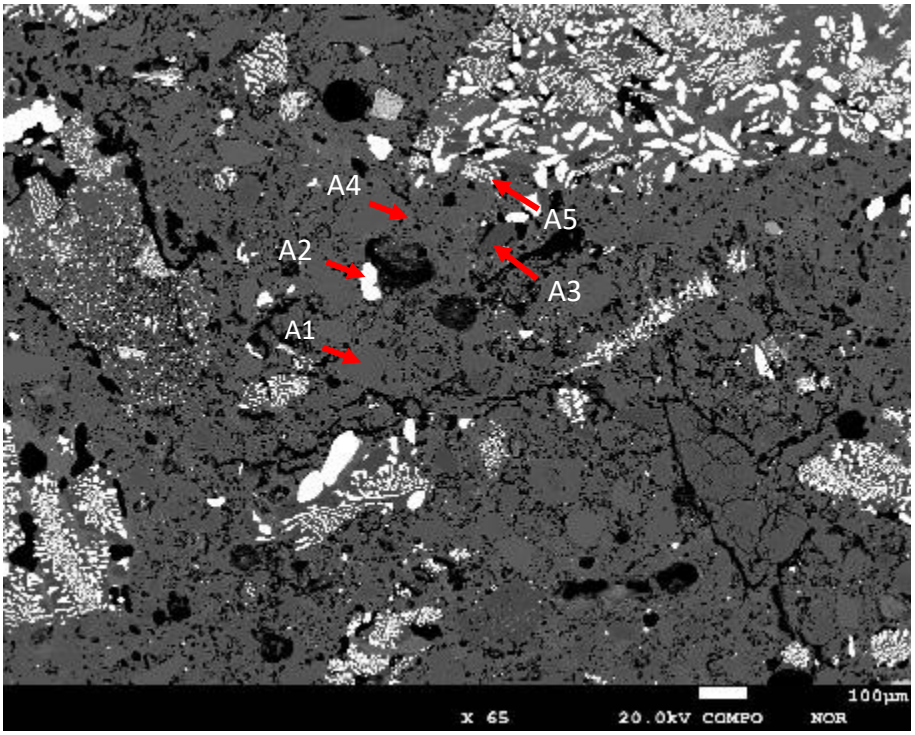

B)

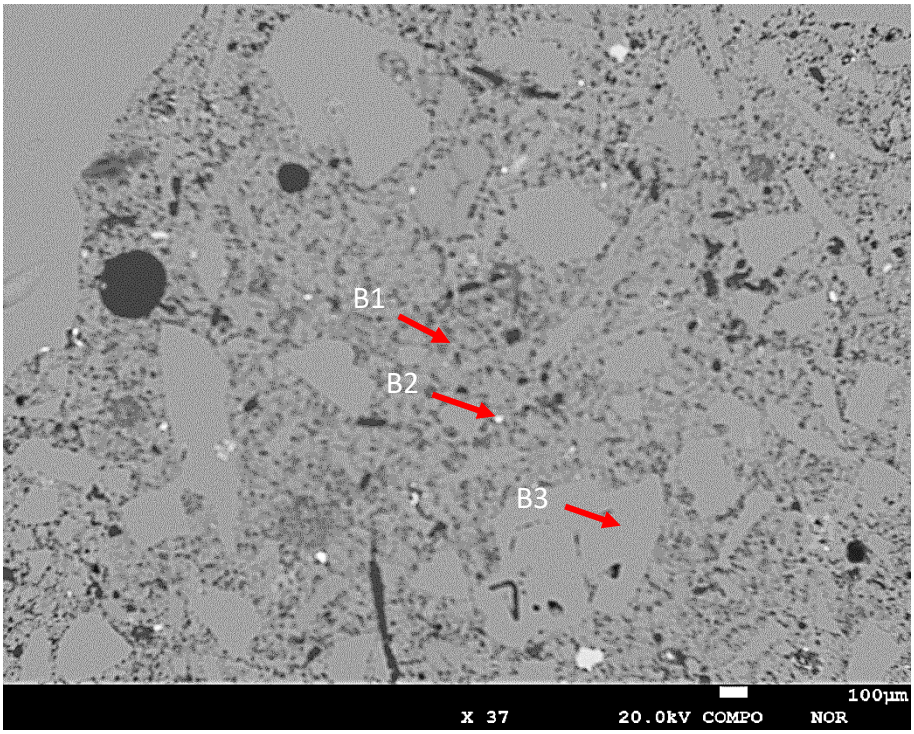

C)

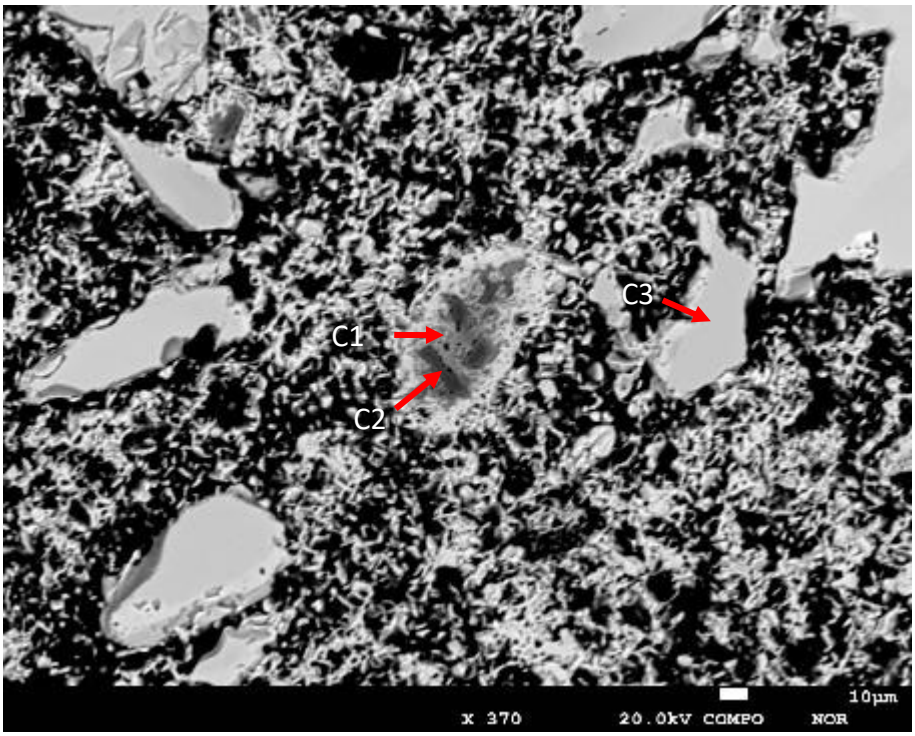

Figure 2-6. Baseline SEM images of A) R1, B) R2 and C) R3 with key phases identified.

Table 2-5. Composition of key points identified in Figure 2-6 as determined by EPMA.

	Wt %											
Label	**K_2O**	**CaO**	**Na_2O**	**Al_2O_3**	**SiO_2**	**Cr_2O_3**	**SO_3**	**ZrO_2**	**FeO**	**TiO_2**	**HfO_2**	**SiC[1]**
A1	0.1	0.9	0.4	61.6	34.2	0.0	0.0	0.1	0.5	2.2	0.0	0.0
A2	0.0	0.0	0.0	0.0	0.0	0.0	0.0	98.3	0.0	0.0	1.6	0.0
A3	0.0	0.0	0.0	100.0	0.0	0.0	0.0	0.0	0.0	0.0	0.0	0.0
A4	0.0	0.0	0.0	0.1	0.0	0.0	0.0	0.0	0.0	0.0	0.0	99.9
A5	0.0	0.0	0.0	54.8	0.0	0.0	0.0	44.3	0.1	0.0	0.8	0.0
B1	0.0	0.7	0.0	58.7	38.8	0.0	0.1	0.0	0.6	1.2	0.0	0.0
B2	0.0	0.7	0.0	58.7	0.0	0.0	0.1	0.0	0.6	1.2	0.0	41.2
B3[2]	0.0	0.0	0.0	0.0	0.0	0.0	0.0	0.0	0.0	0.0	0.0	99.9
C1	0.0	1.0	0.0	60.7	0.0	38.2	0.0	0.0	0.0	0.0	0.0	0.0
C2	0.0	1.8	0.1	96.2	0.0	1.9	0.0	0.0	0.0	0.0	0.0	0.0
C3[2]	0.0	0.0	0.0	11.5	0.0	88.1	0.0	0.1	0.0	0.2	0.0	0.0

[1]Samples were carbon coated; SiC content was inferred when totals for all elements in the oxide form exceeded 100 wt %.
[2]These measurement points were not taken in the field of view of the displayed images. Homologous points were identified in Figure 2-6.

2.4.4.2 Cup tests

Cross-sections of refractory materials following cup corrosion tests at 1250 °C are presented in Figure 2-7. On a macroscopic scale, R1 (Figure 2-7A) appears to have been the most heavily affected, with a darker grey discoloration that extends almost to the edges of the test piece. On a microscopic scale (Figure 2-7B), this refractory also appears to be the most affected. The red arrow indicates a zirconia/alumina grain that appears to be dislodged as as result of dissolution of the binder around it. Infiltration of slag into the refractory can be observed by the reduction in the refractory's porosity just below the slag-refractory interface. R3 (Figure 2-7F) also had some grains dislodged from the refractory surface and dissolution of chromia in the slag phase, but the microstructure below the slag-refractory interface appears minimally affected.

Observed penetration depths of key species contained within the slag phase are presented in Table 2-6. R3 suffered significantly less penetration by all species compared to the other refractories tested. R1 was tested at two different temperatures (1075 °C and 1250 °C with Slag 1 and Slag 2, respectively), and in both cases showed the greatest penetration by Na_2O. Despite the significant proportion of Na_2SO_4 in Slag 1, no penetration of sulfur was observed in the refractory material. It is hypothesized that as the sodium reacted with the refractory to form other species, the sulfur was released as a gas. This theory is corroborrated by the bubbling that was observed upon melting of the slag during a sessile drop corrosion test with Slag 1 and R1 (data not shown). The slag did not significantly bubble upon melting when a platinum disk was used as the substrate for surface tension measurements (Figure 2-S2A) and only showed 2% mass loss over the duration of the experiment.

The average concentration of Na_2O and K_2O as a function of depth in R1 for the 1250 °C cup test is shown in Figure 2-8. While K_2O was present at a much lower concentration than Na_2O in the

starting slag composition, and as a result throughout the refractory, it trends closely with Na_2O throughout the depth of the refractory. Based on images of the refractory microstructure near the slag-refractory interface compared to deeper in the test piece, it is hypothesized that the alkali species are transported through the refractory through a mechanism other than penetration by the bulk liquid, such as gas-phase transport through pores followed by condensation, or selective diffusion. The liquid-phase infiltration of R1 appears to traverse only about 0.4 mm into the refractory (Figure 2-7B), and beyond this point the microstucture appears similar to the untreated refractory in Figure 2-6A. This is also where the concentration of alkalis in the refractory rapidly drops off (Figure 2-8).

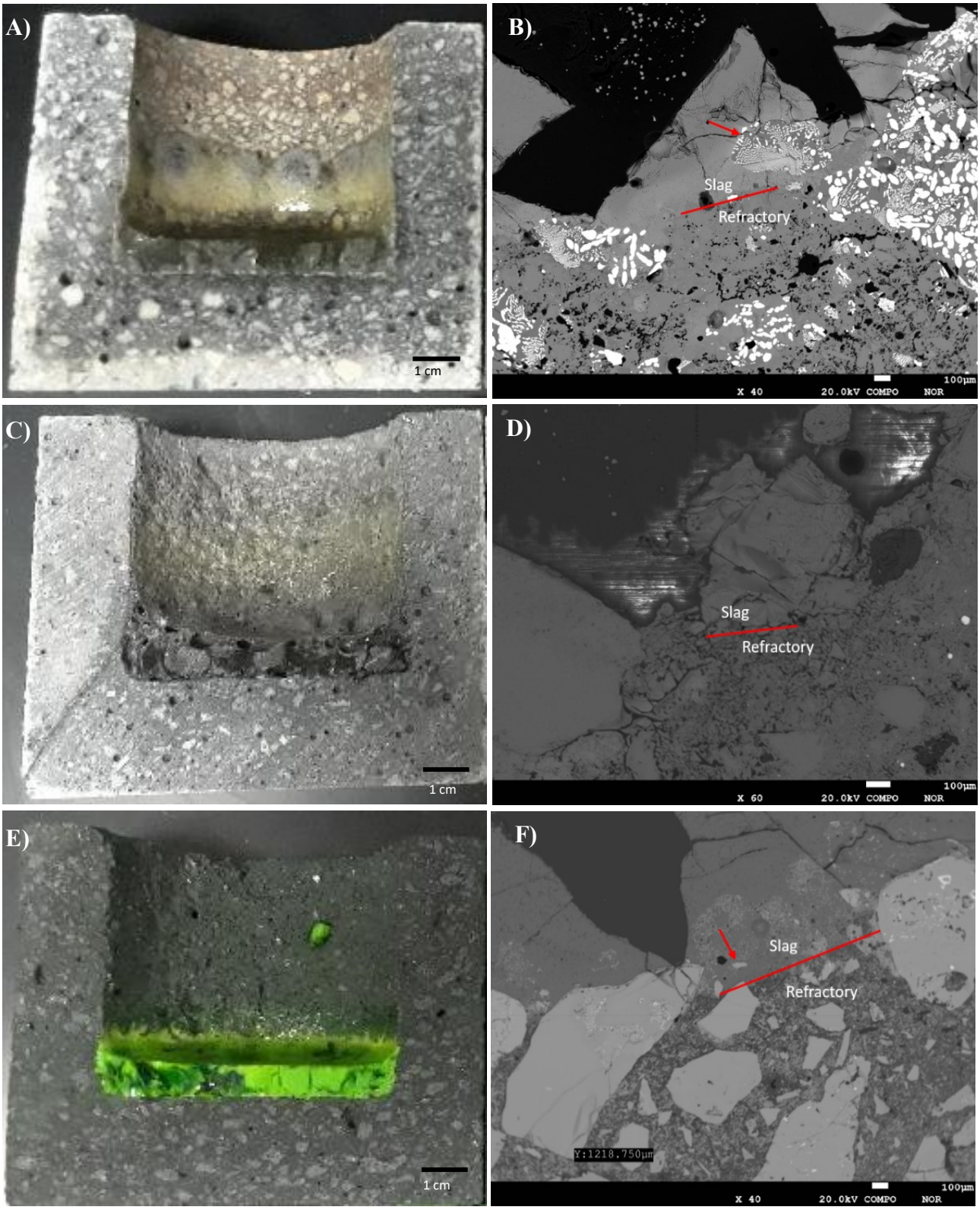

Figure 2-7. Cross-sections of refractory cups (A, C, E) and SEM images of cross-sections near slag-refractory interface (B, D, F) following corrosion cup tests with Na_2SO_4-free Slag 2 at 1250 °C for 5 h. Refractory samples R1 (A, B), R2 (C, D) and R3 (E, F) are shown. The red arrows indicate dislodged refractory grains.

Table 2-6. Observed penetration depth of species found in Slag 1 and 2 into refractory materials following 5 h corrosion cup tests (Tests with Slag 2 (Na2SO4-free basis) at 1250 °C; test with Slag 1 at 1075 °C). A threshold concentration of 1 wt % was used for determination of penetration depth.

Refractory:	R1	R1	R2	R3
Slag formulation:	**Slag 1**	**Slag 2**	**Slag 2**	**Slag 2**
Species	**Penetration depth (mm)**			
Na_2O	≥14.30[1]	≥10.65[1]	6.65	0.55
K_2O	0.05	0.40	1.20	0.23
SiO_2	-	-	-	0.95
SO_3	0.00	-	-	-

[1]Na_2O penetrated the full depth of the sample area analyzed, but the area analyzed did not constitute the full depth of the cup.

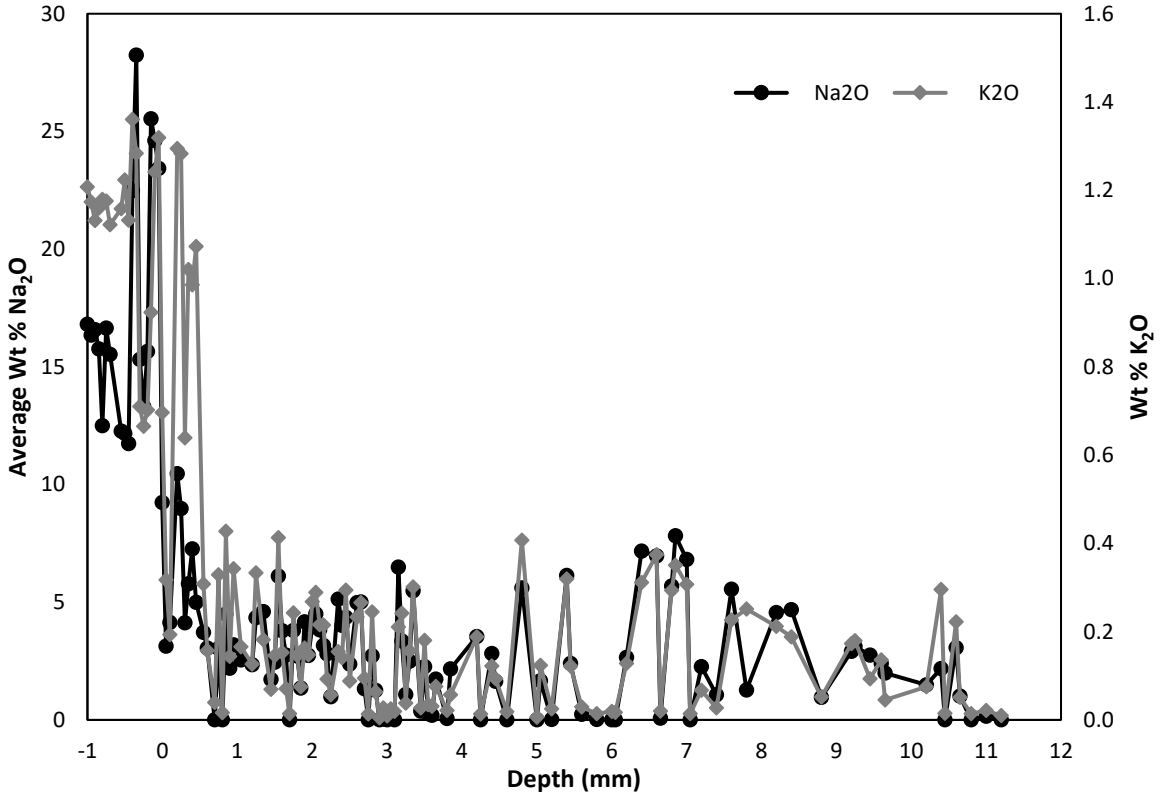

Figure 2-8. Average concentration of alkali species as a function of depth into R1 during 5 h corrosion cup test at 1250 °C with Na2SO4-free Slag 2.

From the results of the slag penetration models (Table 2-3), the low-density solid nepheline was predicted to form with each of the three refractory materials tested, though it was expected to form at a greater depth below the surface of R1 at 1075 °C since the liquid phase persisted beyond the first two calculation steps (Figure 2-4). Based on elemental ratios measured by EPMA, a number

of points in the cup test cross-sections were identified that may contain nepheline in both R1 and R2 (Table 2-7). Most of these points are in the slag layer, indicating dissolution and diffusion of components of the refractory through the slag. In one instance, nepheline appears to have formed well within R2 (depth of 1.55 mm), where it has the potential to be more damaging due to volume expansion. Formation of aluminoscilicates, such as nepheline, anorthite and leucite, upon reaction of silica-containing refractories with alkali-rich slags has previously been observed in literature [26], [36].

Dissolution of Cr_2O_3 from R3 was observed when contacted with Slag 2 (Table 2-7). A known corrosion mechanism of chromium–containing materials is as follows [37]:

$$Cr_2O_3 + 4Na^+ + \frac{5}{2}O_2 \rightarrow 2Na_2CrO_4$$

Sodium chromate was also predicted to form by the slag penetration models (Table 2-3). This may be the cause of the chromia dissolution observed here. Chromium-based species have been shown to be less reactive and volatile when chromium is a constituent in a spinel lattice instead of in a Cr_2O_3 grain [36], [38]. This is likely a result of the closer packing of atoms in the spinel structure and stronger intermolecular forces. It is thus hypothesized that dissolution may also be reduced for a chromia spinel refractory compared to a Cr_2O_3 refractory. Thus, it is possible that a chromia spinel refractory may show superior performance compared to R3.

Table 2-7. Composition of key points measured by EPMA from corrosion cup tests. Depth is relative to the slag-refractory interface.

			Wt % of species							
Refractory	**Slag**	**Depth (mm)**	**K_2O**	**CaO**	**Na_2O**	**Al_2O_3**	**SiO_2**	**Cr_2O_3**	**ZrO_2**	**Comment**
R1	1	-0.2	4.05	-	14.33	31.37	50.25	-	-	May contain nepheline
R1	2	-0.15	-	-	24.79	26.49	44.90	-	3.82	May contain nepheline
R1	2	-0.1	1.23	-	24.00	25.02	45.76	-	3.99	May contain nepheline
R1	2	-0.05	1.11	-	23.48	26.05	45.84	-	3.52	May contain nepheline
R2	2	0.4	1.11	1.64	14.95	30.93	51.36	-	-	May contain nepheline
R2	2	1.55	-	6.36	12.29	29.35	52.00	-	-	May contain nepheline
R3	2	-2.6	1.36	-	11.85	2.15	78.72	5.92	-	Slag furthest from refractory showing dissolution of Cr_2O_3 in slag

2.4.4.3 Sessile drop corrosion tests

All cup test experiments were repeated as sessile drop corrosion tests to both assess wettability of the refractory, and to validate use of the sessile drop tests as a screening for refractory corrosion in lieu of cup tests. The wettability could only be qualitatively characterized. Upon melting, all slag samples immediately flattened and spread across the refractory surface, spilling over the edges. This is indicative of a low contact angle and high wettability, though it was not possible to measure it due to the spillover.

In terms of refractory corrosion, cross-sections of the refractory samples following sessile drop tests were analyzed by SEM-EPMA and compared to the cup tests (Figure 2-S8 shows one example). The same conclusions on refractory performance were drawn from both tests, though penetration depth could not be as easily quantified from the sessile drop tests due to overflow and pooling of the slag samples at the bottom of the refractory sample during testing. Despite the slag spillover, similar changes in refractory microstructure near the slag layer were observed and phases predicted by the slag penetration models were also identified in analysis of the sessile drop test samples. This method is thus appropriate for observing phenomena relating to refractory corrosion occurring near the slag-refractory interface when less sample material is available for testing. Provided there is no spillover of the molten solution (i.e. there is a larger contact angle between the molten solution and the refractory), this method would also be appropriate for comparing slag or salt penetration depth.

With the corrosion screening method validated, additional sessile drop tests were performed with Salt 1 and R1, R2 and R3 at 1075 °C. Immediately upon melting, the salt solution in all tests bubbled as it spread across the refractory and after a short time, no liquid phase appeared to remain. Thus, similar to the slag wettability tests, the wettability of the salts on the refractories could not

be measured. Figure 2-9 shows cross-sections of R1, R2 and R3 following exposure to the salt. No apparent liquid layer remained, but structural changes were noted as follows. For R1 (Figure 2-9A, D), a large horizontal void formed along the surface exposed to the salt, leaving a roughly 250 μm shell that could easily spall. For R2 (Figure 2-9B, E), the refractory appeared to foam upon reaction with the salt, leading to breakdown and increased porosity of the refractory in the region contacting the salt. With a macroscopic view, the affected area of the refractory appears to extend 3.7 mm down into the material (total refractory depth = 12.4 mm). No structural changes were observed in R3 as a result of salt exposure.

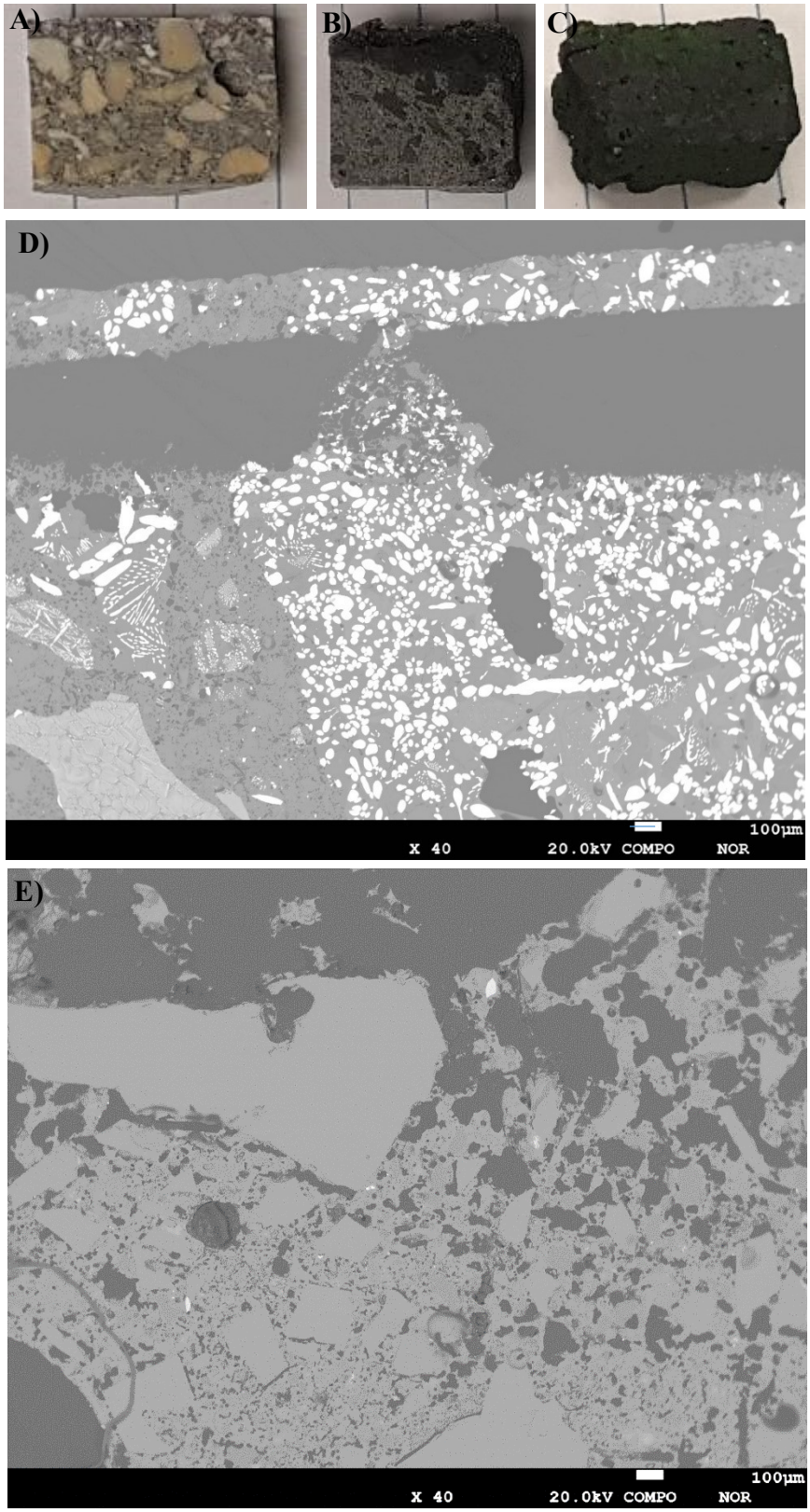

Figure 2-9. Cross sections of refractory pieces (A, B, C) and SEM images near salt-refractory interfaces (D, E) following sessile drop corrosion tests and with Salt 1 at 1075 °C for 4 hr. Refractory pieces R1 (A, D), R2 (B, E) and R3 (C).

2.5 Conclusions

The deposits forming in the DCSG combustor when injecting FWKD as the water source for steam production are expected to be high in SiO_2 (≥50 wt %) and Na_2O (≥30 wt %) at intended operating temperatures, with greater incorporation of Na_2SO_4 at lower temperatures, and formation of a Na_2SO_4-rich molten salt phase at temperatures below 1198 °C. The measured viscosity of Slags 1 and 2 were quite low at their formation temperatures in the combustor (<4 Pa·s), meaning they will flow easily and have a greater opportunity to penetrate and dissolve the refractory. They are also close to the suggested minimum viscosity of 2.5 Pa·s, meaning that refractory erosion could occur more quickly in regions of the combustor where the wall temperature exceeds 1250 °C.

Corrosion model results agreed well with experimental work. EPMA results gave evidence to support the formation of nepheline during the corrosion tests with Slag 1 with R1, as well as Slag 2 and both R1 and R2. This phase was also predicted to form for these tests by the slag penetration models. Dissolution of the R1 binder was predicted based on the high calculated metastable diffusion factor of the mullite phase, and was observed to have occurred during both the cup and sessile drop corrosion tests. Finally, R3 was expected to show the greatest corrosion resistance of the three refractories tested because all liquid phases were quickly consumed after only two calculation steps in the slag penetration models, which could indicate only shallow penetration, and because, while a low density solid phase was predicted to form, it would likely only form at the surface. This refractory did, in fact, have the greatest resistance to penetration of all of the refractories tested, and no nepheline was identified.

Two methods of testing corrosion were presented in this work – a sessile drop test and a cup test. Comparison of the same conditions tested through both methods yielded the same conclusions in terms of overall refractory performance, though slag penetration depth was more clearly

demonstrated in the cup tests. Validation of the two methods allows for a greater number of conditions to be tested using the sessile drop method while requiring less material. Sessile drop testing is a good option for screening of refractories before more rigorous testing.

Two of the three refractories suffered severe structural changes as a result of corrosion tests with the salt. For this reason it is recommended that the operating temperature of the combustor be sufficiently high to avoid formation of this corrosive salt phase. Contrary to this, in terms of reducing the rate of refractory corrosion, avoiding excessively low slag viscosities and maximizing steam throughput for a given combustor size and firing rate, the combustor operating temperature should be minimized. Thus, to meet all of these criteria, it is recommended that the combustor wall temperature be maintained between 1200 and 1250 °C in regions where inorganics will be contacting the walls.

In terms of refractory material selection, of those tested, the chromia-corundum refractory offered the greatest resistance to penetration by both the slag and salt phases. There was, however, dissolution of Cr_2O_3 (~6 wt% in the bulk slag phase), and thus further testing with this refractory is warranted. Based on the corrosion models, a chromia spinel refractory (such as R7) also suggested promising results and may offer greater resistance to dissolution due to the close-packed spinel structure. Due to the higher costs and potential environmental concerns associated with chromium-based refractories [39], [40], as well as its good performance in the corrosion models, a high-density magnesium aluminate spinel (such as R4 in this work) should also be considered.

Conversely, the mullite-zirconia refractory yielded the poorest resistance of those tested to the FWKD slags, contrary to the rule of thumb that acidic refractory materials are best suited for acidic slags. Corrosion tests with this refractory showed dissolution of the alumina-silica binder phase, mobilization of the zirconia grains, and formation of nepheline, a low-density solid. Likewise,

evidence of nepheline formation was also found upon reaction of the alumina-silica binder phase of the silicon carbide refractory with the slag. For this reason, aluminosilicate-based refractory materials should be avoided for this application using FWKD as the feedstock.

2.6 References

[1] B. Clements, "High pressure direct contact oxy-fired steam generator," CA 2744825 C, May 05, 2015.

[2] P. E. C. Cairns *et al.*, "High-pressure oxy-firing (HiPrOx) of fuels with water for the purpose of direct contact steam generation," *Energy Fuels*, vol. 29, no. 7, pp. 4522–4533, Jul. 2015, doi: 10.1021/ef502754h.

[3] J. Seaba, D. Wissmiller, and S. Alavandi, "Advanced steam generation: Technologies for Canadian oil sands," Gas Technology Institute, 2017. Accessed: Apr. 30, 2020. [Online]. Available: https://www.cosia.ca/uploads/documents/id46/COSIA%20Advanced%20Steam%20Generation%20-%20Technologies%20for%20Canadian%20Oil%20Sands.pdf.

[4] M. Wolinetz, "DCSG market analysis," Navius Research, 2013.

[5] R. G. Pillai, N. Yang, S. Thi, J. Fatema, M. Sadrzadeh, and D. Pernitsky, "Characterization and comparison of dissolved organic matter signatures in steam-assisted gravity drainage process water samples from Athabasca oil sands," *Energy Fuels*, vol. 31, no. 8, pp. 8363–8373, Aug. 2017, doi: 10.1021/acs.energyfuels.7b00483.

[6] J. Nakano, S. Sridhar, J. Bennett, K.-S. Kwong, and T. Moss, "Interactions of refractory materials with molten gasifier slags," *Int. J. Hydrog. Energy*, vol. 36, no. 7, pp. 4595–4604, Apr. 2011, doi: 10.1016/j.ijhydene.2010.04.117.

[7] W. E. Lee and S. Zhang, "Melt corrosion of oxide and oxide–carbon refractories," *Int. Mater. Rev.*, vol. 44, no. 3, pp. 77–104, Mar. 1999, doi: 10.1179/095066099101528234.

[8] S. Vargas, F. J. Frandsen, and K. Dam-Johansen, "Rheological properties of high-temperature melts of coal ashes and other silicates," *Prog. Energy Combust. Sci.*, vol. 27, no. 3, pp. 237–429, Mar. 2001, doi: 10.1016/S0360-1285(00)00023-X.

[9] Allied Mineral Products, Inc., "TUFFCRETE® AZS 4 X," Columbus, United States, TUFCAZS4X, Jan. 2016.

[10] "THOR 60 ADTECH." Harbison Walker International.

[11] PD Refratories GmbH, "Chromium Corundum Bricks," 2017. https://www.pd-refractories.com/website/en/products/chromium_bricks/chromium_corundum_bricks.php (accessed Nov. 28, 2017).

[12] M. Carlborg, F. Weiland, C. Ma, R. Backman, I. Landälv, and H. Wiinikka, "Exposure of refractory materials during high-temperature gasification of a woody biomass and peat mixture," *J. Eur. Ceram. Soc.*, vol. 38, no. 2, pp. 777–787, Feb. 2018, doi: 10.1016/j.jeurceramsoc.2017.09.016.

[13] M. Reinmöller, M. Klinger, E. Thieme, and B. Meyer, "Analysis and prediction of slag-induced corrosion of chromium oxide-free refractory materials during fusion of coal and biomass ash under simulated gasification conditions," *Fuel Process. Technol.*, vol. 149, pp. 218–230, 2016, doi: 10.1016/j.fuproc.2016.04.022.

[14] J. Bennett, A. Nakano, J. Nakano, and H. Thomas, "Gasification slag and the mechanism by which phosphorous additions reduce slag wear and corrosion in high Cr_2O_3 refractories," in *Advances in Molten Slags, Fluxes and Salts: Proceedings of the 10th International Conference on Molten Slags, Fluxes and Salts*, 2016, pp. 1109–1116.

[15] C. W. Bale *et al.*, "FactSage thermochemical software and databases, 2010–2016," *Calphad*, vol. 54, pp. 35–53, Sep. 2016, doi: 10.1016/j.calphad.2016.05.002.

[16] P. Geddis *et al.*, "DCSG phase 2, sub-program 5 - Burner design and computational fluid dynamics validation," CanmetENERGY-Ottawa, Ottawa, ON, 2020.

[17] M. A. Duchesne, A. D. Hall, R. W. Hughes, D. J. McCalden, E. J. Anthony, and A. Macchi, "Fate of inorganic matter in entrained-flow slagging gasifiers: Fuel characterization," *Fuel Process. Technol.*, vol. 118, pp. 208–217, Feb. 2014, doi: 10.1016/j.fuproc.2013.09.004.

[18] M. A. Duchesne, A. M. Bronsch, R. W. Hughes, and P. J. Masset, "Slag viscosity modeling toolbox," *Fuel*, vol. 114, pp. 38–43, Dec. 2013, doi: 10.1016/j.fuel.2012.03.010.

[19] A. I. Priven, "General method for calculating the properties of oxide glasses and glass forming melts from their composition and temperature," vol. 45, no. 6, p. 11, 2004.

[20] M. A. Duchesne *et al.*, "Flow behaviour of slags from coal and petroleum coke blends," *Fuel*, vol. 97, pp. 321–328, Jul. 2012, doi: 10.1016/j.fuel.2012.02.019.

[21] "Methods of test for dense refractory products - Guidelines for testing the corrosion of refractories caused by liquids (CEN/TS 15418:2006)." European Committee for Standardization, 2006.

[22] M. A. Duchesne and R. W. Hughes, "Slag density and surface tension measurements by the constrained sessile drop method," *Fuel*, vol. 188, pp. 173–181, Jan. 2017, doi: 10.1016/j.fuel.2016.10.023.

[23] J. Fagerström, "Fine particle emissions and slag formation in fixed-bed biomass combustion aspects of fuel engineering," Ph.D. thesis, Umeå University, Umeå, Sweden, 2015.

[24] G. Zając, J. Szyszlak-Bargłowicz, W. Gołębiowski, and M. Szczepanik, "Chemical characteristics of biomass ashes," *Energies*, vol. 11, no. 11, p. 2885, Oct. 2018, doi: 10.3390/en11112885.

[25] M. Hupa, "Ash-related issues in fluidized-bed combustion of biomasses: Recent research highlights," *Energy Fuels*, vol. 26, no. 1, pp. 4–14, Jan. 2012, doi: 10.1021/ef201169k.

[26] D. N. Togobitskaya, A. F. Khamkhot'ko, N. A. Tsivataya, and D. A. Stepanenko, "Corrosion activity of alkali-containing slags with respect to a blast furnace refractory lining," *Refract. Ind. Ceram.*, vol. 54, no. 3, pp. 155–159, Sep. 2013, doi: 10.1007/s11148-013-9568-9.

[27] X. Chen *et al.*, "The key for sodium-rich coal utilization in entrained flow gasifier: The role of sodium on slag viscosity-temperature behavior at high temperatures," *Appl. Energy*, vol. 206, pp. 1241–1249, Nov. 2017, doi: 10.1016/j.apenergy.2017.10.020.

[28] R. Boris, V. Antonovič, J. Keriene, R. Stonys, A. Kudžma, and P. Zdanevičius, "Study of alkali resistance of refractory materials used in boilers operating on wood fuel," *Refract. Ind. Ceram.*, vol. 57, no. 6, pp. 651–654, Mar. 2017, doi: 10.1007/s11148-017-0039-6.

[29] Q. Shu, Y. Wang, J. Li, Y. Liu, P. Li, and K. Chou, "Effect of Na_2O on dissolution rate of alumina in CaO–Al_2O_3–MgO–SiO_2 Slag," *ISIJ Int.*, vol. 55, no. 11, pp. 2297–2303, 2015, doi: 10.2355/isijinternational.ISIJINT-2015-211.

[30] J. Roy, S. Chandra, S. Das, and S. Maitra, "Oxidation behaviour of silicon carbide - a review," *Rev. Adv. Mater. Sci*, vol. 38, pp. 29–39, 2014.

[31] R. Z. Xu, J. L. Zhang, Z. Y. Wang, and K. X. Jiao, "Influence of Cr_2O_3 and B_2O_3 on Viscosity and Structure of High Alumina Slag," *Steel Res. Int.*, vol. 88, no. 4, p. 1600241, 2017, doi: 10.1002/srin.201600241.

[32] G. Qiu, L. Chen, J. Zhu, X. Lv, and C. Bai, "Effect of Cr_2O_3 Addition on Viscosity and Structure of Ti-bearing Blast Furnace Slag," *ISIJ Int.*, vol. 55, no. 7, pp. 1367–1376, 2015, doi: 10.2355/isijinternational.55.1367.

[33] L. Deng *et al.*, "Influence of Cr_2O_3 on the viscosity and crystallization behavior of glass ceramics based on blast furnace slag," *Mater. Chem. Phys.*, vol. 240, p. 122212, Jan. 2020, doi: 10.1016/j.matchemphys.2019.122212.

[34] Q. Li, J. Gao, Y. Zhang, Z. An, and Z. Guo, "Viscosity measurement and structure analysis of Cr_2O_3-bearing CaO-SiO_2-MgO-Al_2O_3 slags," *Metall. Mater. Trans. B*, vol. 48, no. 1, pp. 346–356, Feb. 2017, doi: 10.1007/s11663-016-0858-8.

[35] T. Wu, Y. Zhang, F. Yuan, and Z. An, "Effects of the Cr_2O_3 content on the viscosity of CaO-SiO_2-10 Pct Al_2O_3-Cr_2O_3 quaternary slag," *Metall. Mater. Trans. B*, vol. 49, no. 4, pp. 1719–1731, Aug. 2018, doi: 10.1007/s11663-018-1258-z.

[36] S. Schaafhausen, E. Hugon, E. Yazhenskikh, B. Wilhelmi, and M. Müller, "Corrosion of refractory materials in fluidised bed gasification of alkali rich fuels," *Adv. Appl. Ceram.*, vol. 114, no. 1, pp. 55–64, Jan. 2015, doi: 10.1179/1743676114Y.0000000191.

[37] Y. Niu, H. Tan, and S. Hui, "Ash-related issues during biomass combustion: Alkali-induced slagging, silicate melt-induced slagging (ash fusion), agglomeration, corrosion, ash utilization, and related countermeasures," *Prog. Energy Combust. Sci.*, vol. 52, pp. 1–61, Feb. 2016, doi: 10.1016/j.pecs.2015.09.003.

[38] P. Biedenkopf *et al.*, "Vaporization and corrosion of refractories in the presence of pressurized pulverized coal combustion slag," *J. Am. Ceram. Soc.*, vol. 84, no. 7, pp. 1445–1452, Dec. 2004, doi: 10.1111/j.1151-2916.2001.tb00858.x.

[39] C. Wang, J. K. Yu, and L. Yuan, "Reaction mechanism of MgO–ZrO_2 refractory with CaO–SiO_2 –Al_2O_3 –Fe_tO slag," *Mater. Res. Innov.*, vol. 18, no. sup2, pp. S2-498-S2-503, May 2014, doi: 10.1179/1432891714Z.000000000444.

[40] J. P. Bennett and K.-S. Kwong, “Failure mechanisms in high chrome oxide gasifier refractories,” *Metall. Mater. Trans. A*, vol. 42A, pp. 888–904, 2011, doi: 10.1007/s11661-011-0635-x.

[41] G. J. Janz, G. M. Dijkhuis, G. R. Lakshminarayanan, R. P. T. Tomkins, and J. Wong, “Molten salts : Volume 2, Section 1. Electrochemistry of molten salts: Gibbs free energies and excess free energies from equilibrium-type cells, Section 2. Surface tension data,” National Bureau of Standards. Accessed: May 19, 2017. [Online]. Available: http://archive.org/details/moltensaltsvolum28janz.

2.7 Supplementary Data

2.7.1 Supplementary materials and methods

2.7.1.1 Surface tension and density

Surface tension and density were measured using the same equipment as the sessile drop tests described in Section 2.3.6.2. Approximately 0.15 g of sample was placed onto an 8 mm diameter platinum disk and heated in the tensiometer furnace under a constant flow of 31 SLPH of air at atmospheric pressure. A video was captured while heating throughout the temperature range of interest while maintaining a heating/cooling rate of 5-10 °C/min. For all samples except for Slag 2, all measurements were taken upon heating the sample. For Slag 2, due to the large quantity of bubbles in the sample even after degassing, measurements were taken upon cool-down from the maximum target temperature, when fewer bubbles remained. Frames from the video at the temperatures of interest were fitted with the Laplace-Young equation using the software ADSA-SD to calculate the surface tension and density of the drop [1].

2.7.1.2 Refractory characterization

To characterize pores up to 1780 Å in size, each refractory was coarsely crushed and then nitrogen sorption-desorption measurements were performed at -196 °C with a Micromeritics Tristar 3020 II analyzer (USA). Before the measurements, the samples were degassed under a continuous nitrogen flow at 300°C for 15 h. The Brunauer-Emmett-Teller (BET) method was adopted to calculate specific surface area (SBET) through the adsorption data using a relative pressure (P/P0) range from 0.05 to 0.25. By using the Barrett-Joyner-Halenda (BJH) model, the pore volume and pore size distribution were derived from the adsorption branch of the isotherms, and the total pore volume (Vt) was estimated from the adsorbed amount at P/P0 = 0.992.

To characterize the size, shape and interconnectivity of larger pores, scanning electron microscopy (SEM) images of each refractory were taken. Prior to imaging, pieces of each refractory were cut

to sizes of approximately 15 mm x 15 mm x 10 mm and embedded in a 25 mm epoxy disk. The refractory surface of the samples was then polished, ion milled and carbon coated. Atlas 5 BBV was used to view the images and measure the pore sizes.

2.7.2 Supplementary results

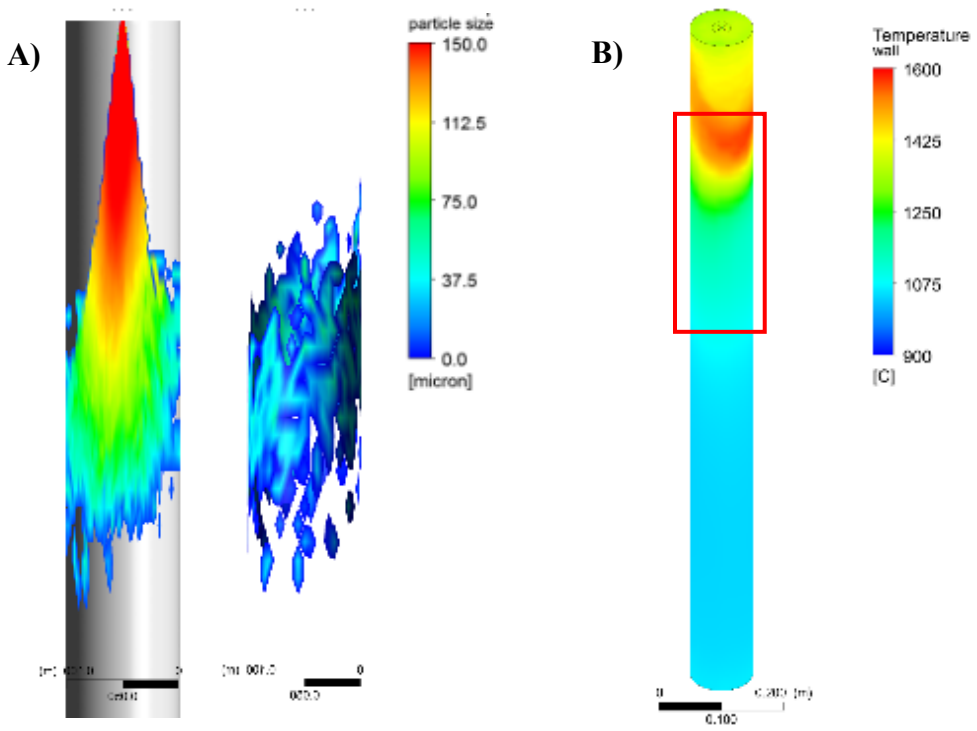

Figure 2-S1. Computational fluid dynamics (CFD) model of the DCSG combustor showing A) location and size of particles contacting the wall and; B) temperature of the wall, highlighting the region of particle impact at 55 bar(g).

A)

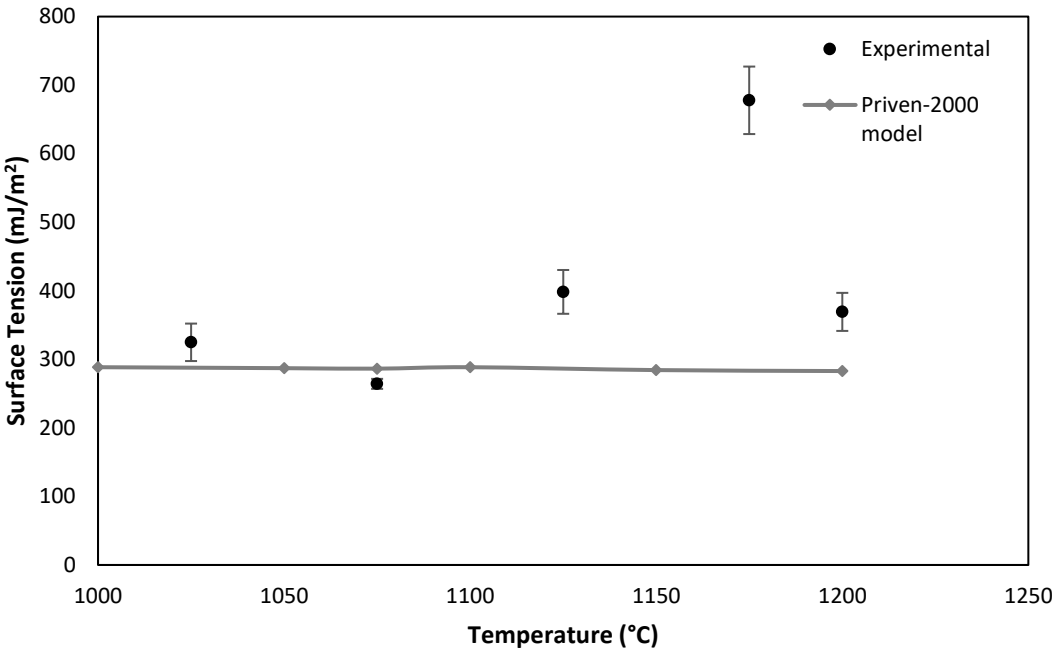
Experimental
Priven-2000 model
Surface Tension (mJ/m²)
Temperature (°C)
800
700
600
500
400
300
200
100
0
1000
1050
1100
1150
1200
1250

B)

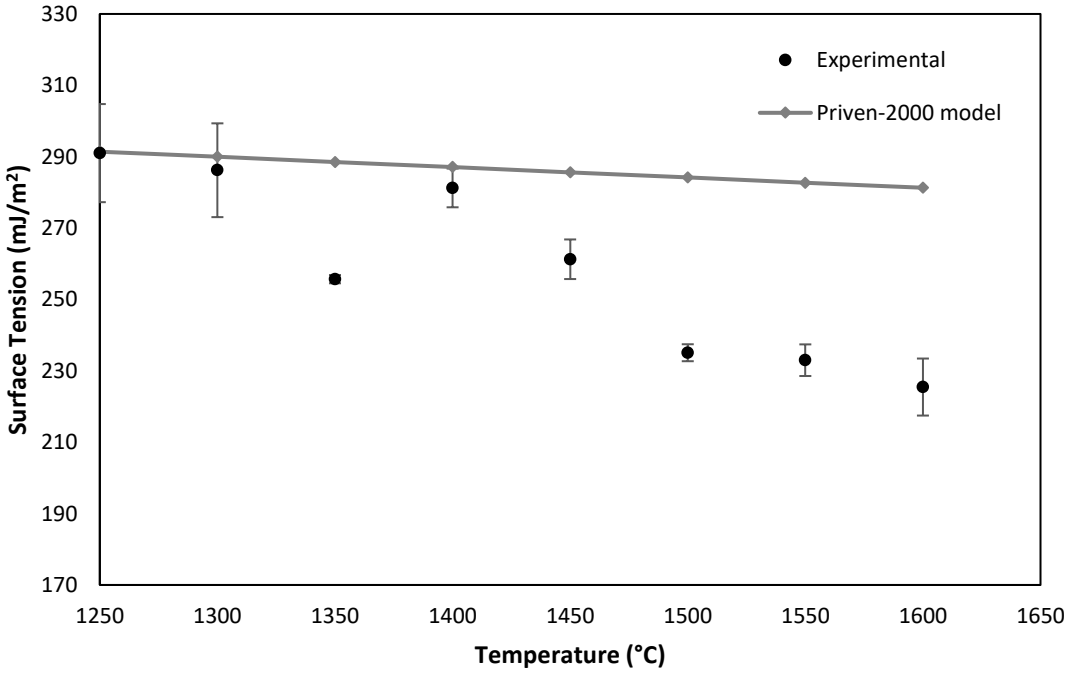
Experimental
Priven-2000 model
Surface Tension (mJ/m²)
Temperature (°C)
330
310
290
270
250
230
210
190
170
1250
1300
1350
1400
1450
1500
1550
1600
1650

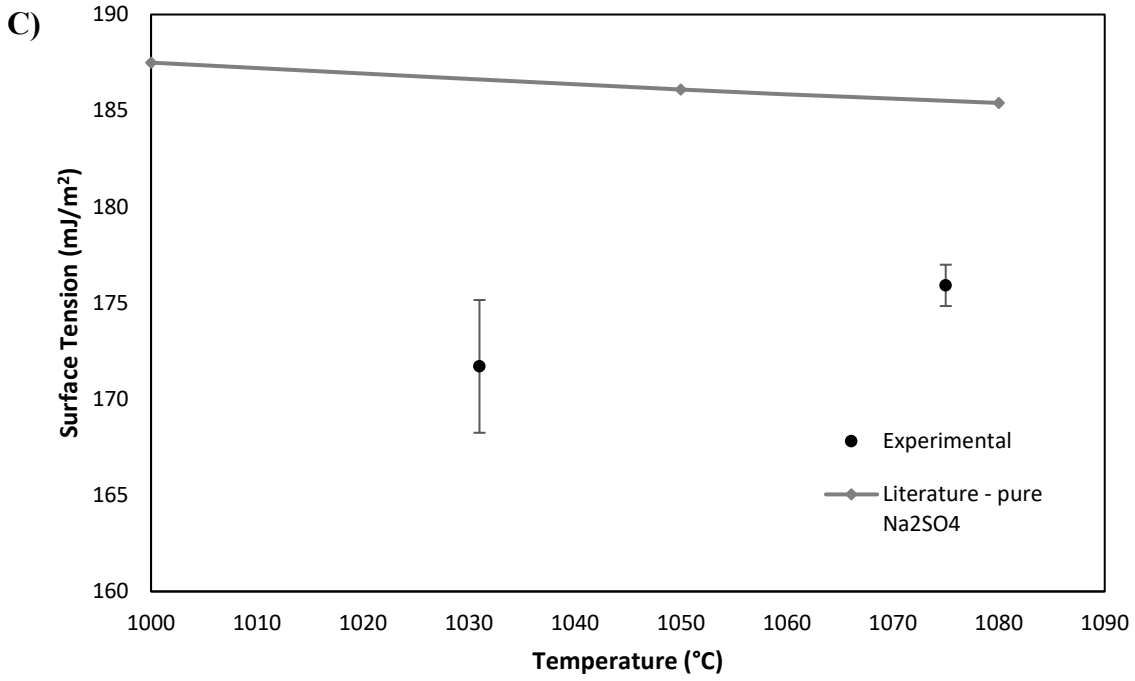

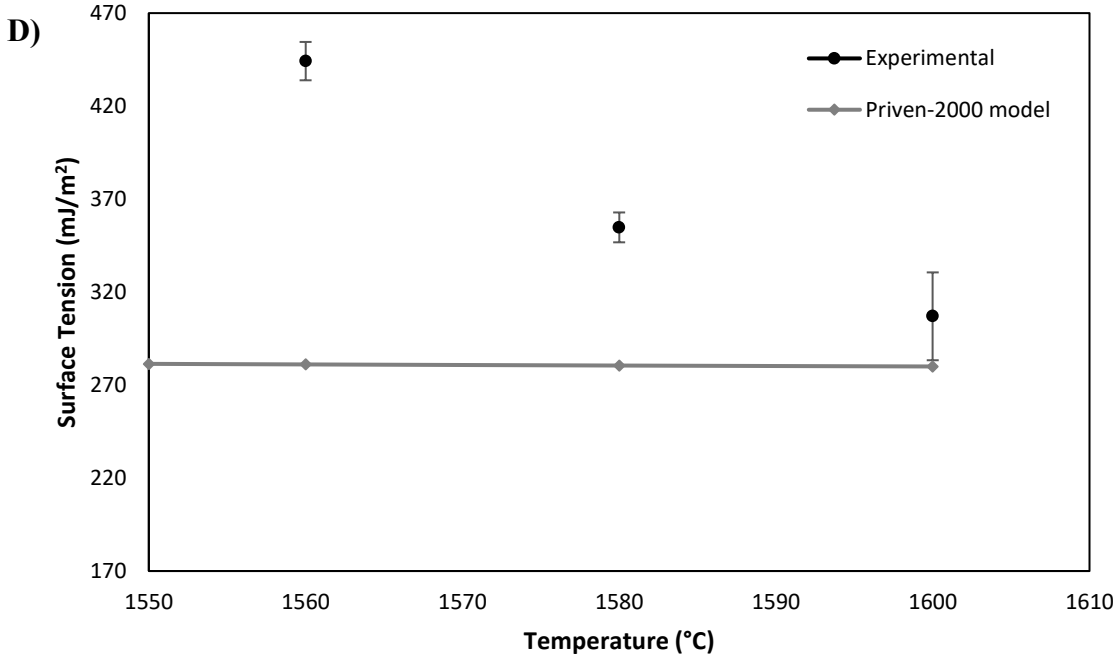

Figure 2-S2. Average surface tension of A) Slag 1; B) Slag 2; C) Slag 3; and D) Salt 1 as a function of temperature. Error bars show ± 2σ of 5 repeat measurements. Literature data for Na_2SO_4 from Janz *et al.* [41] and surface tension modelling done using the Priven-2000 model [19].

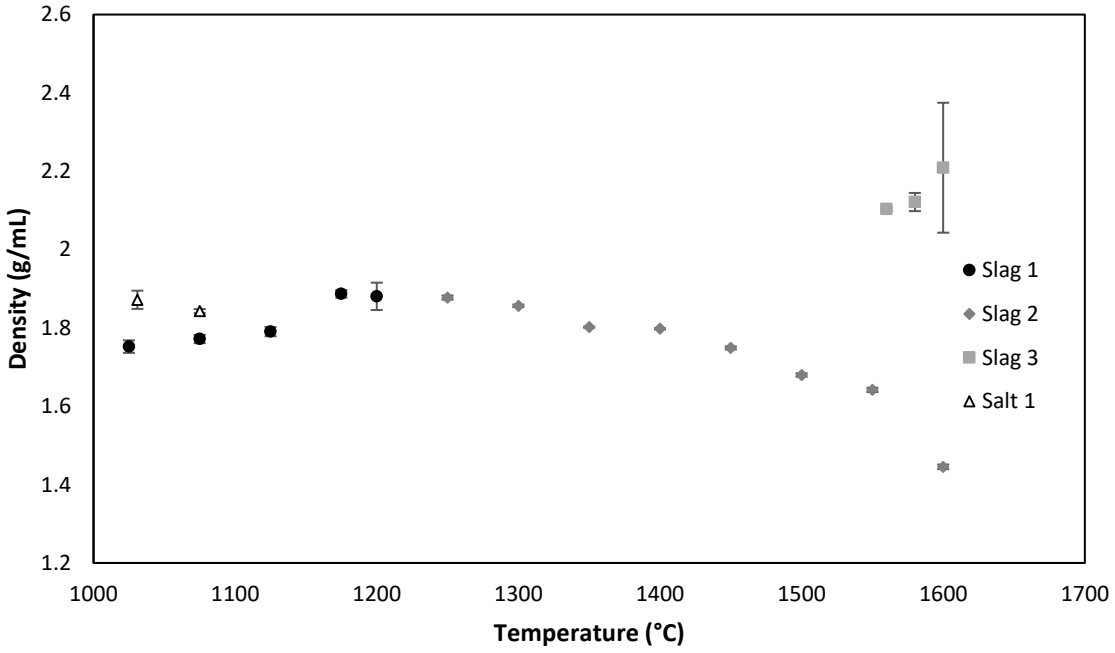

Figure 2-S3. Average density of liquid phases as a function of temperature. Error bars show ± 2σ of 5 repeat measurements.

A)

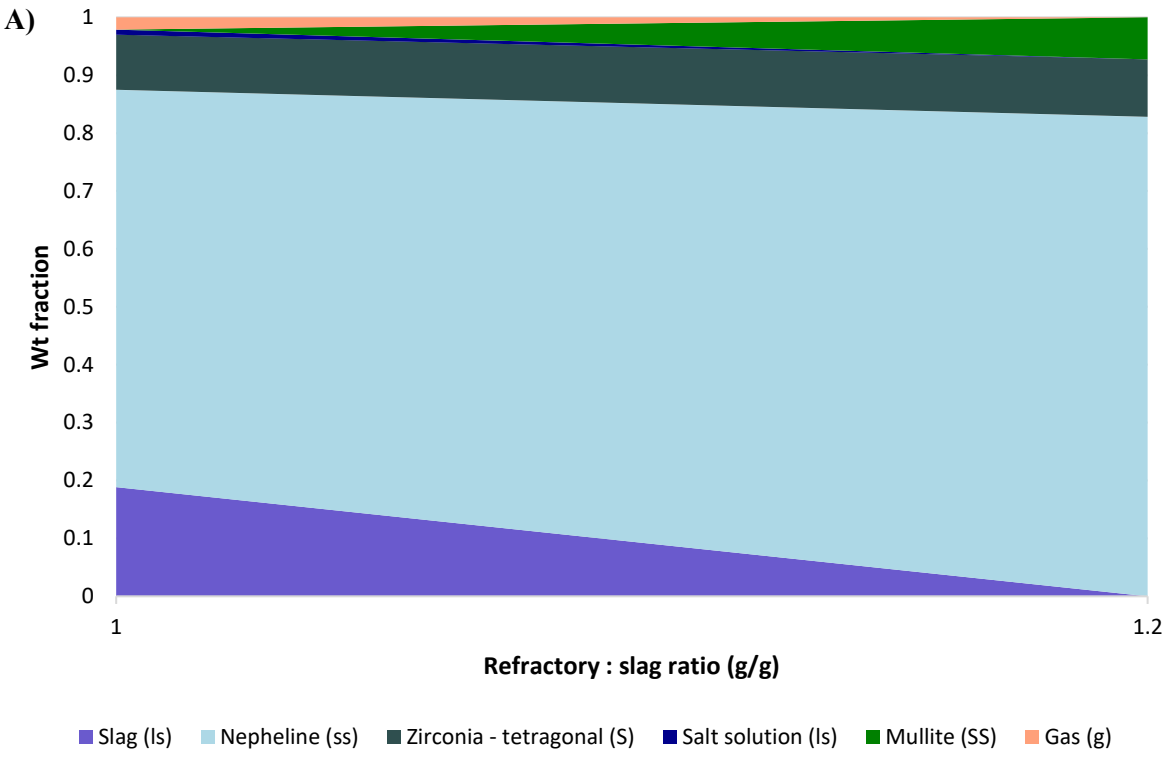
1
0.9
0.8
0.7
0.6
0.5
0.4
0.3
0.2
0.1
0
Wt fraction
1
1.2
Refractory : slag ratio (g/g)
Slag (ls)
Nepheline (ss)
Zirconia - tetragonal (S)
Salt solution (ls)
Mullite (SS)
Gas (g)

B)

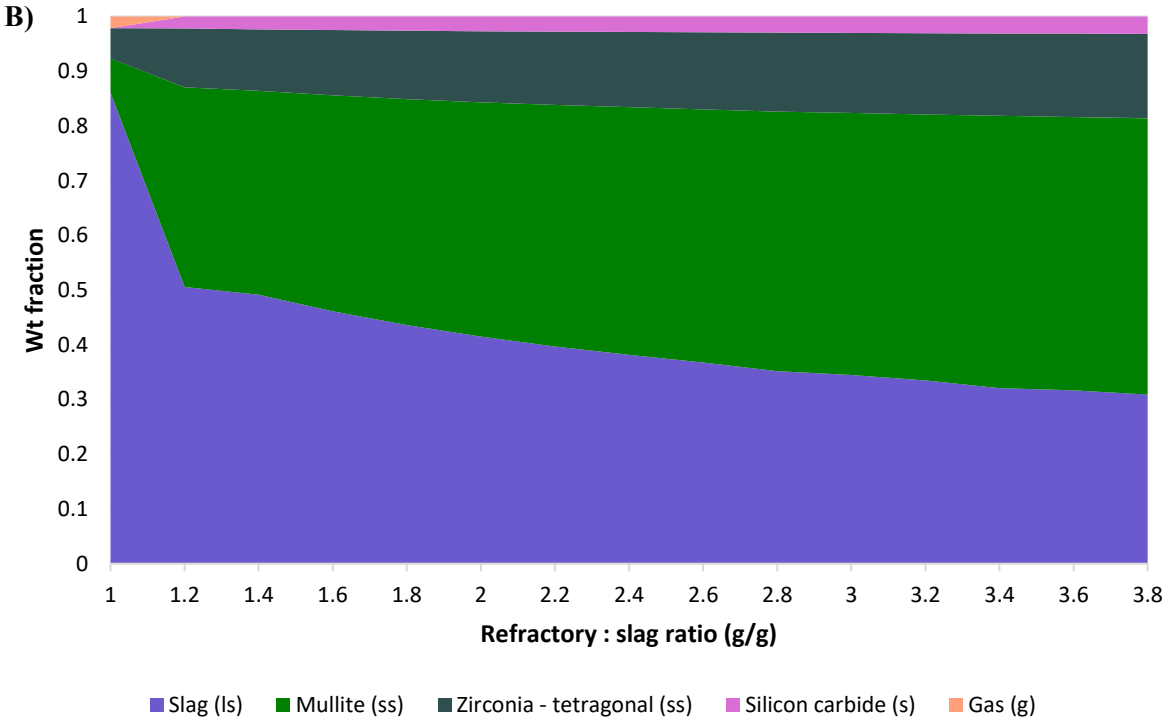
1
0.9
0.8
0.7
0.6
0.5
0.4
0.3
0.2
0.1
0
Wt fraction
1
1.2
1.4
1.6
1.8
2
2.2
2.4
2.6
2.8
3
3.2
3.4
3.6
3.8
Refractory : slag ratio (g/g)
Slag (ls)
Mullite (ss)
Zirconia - tetragonal (ss)
Silicon carbide (s)
Gas (g)

C)

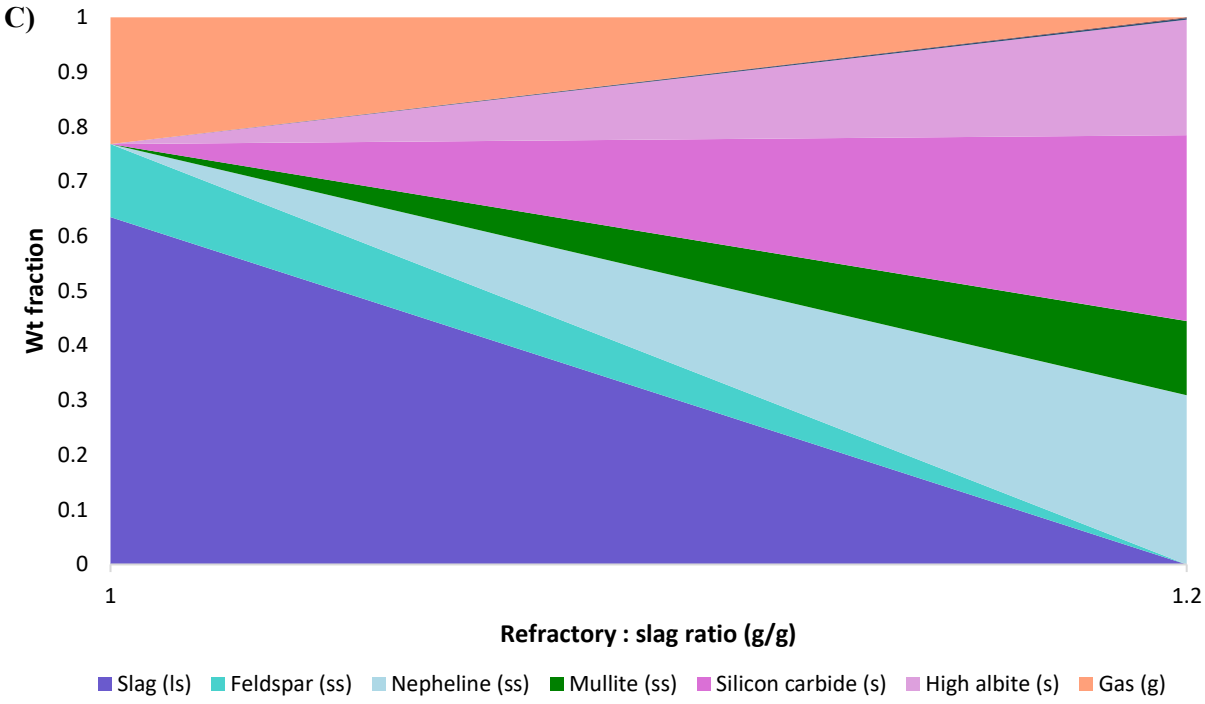
1
0.9
0.8
0.7
0.6
0.5
0.4
0.3
0.2
0.1
0
Wt fraction
1
1.2
Refractory : slag ratio (g/g)
Slag (ls)
Feldspar (ss)
Nepheline (ss)
Mullite (ss)
Silicon carbide (s)
High albite (s)
Gas (g)

D)

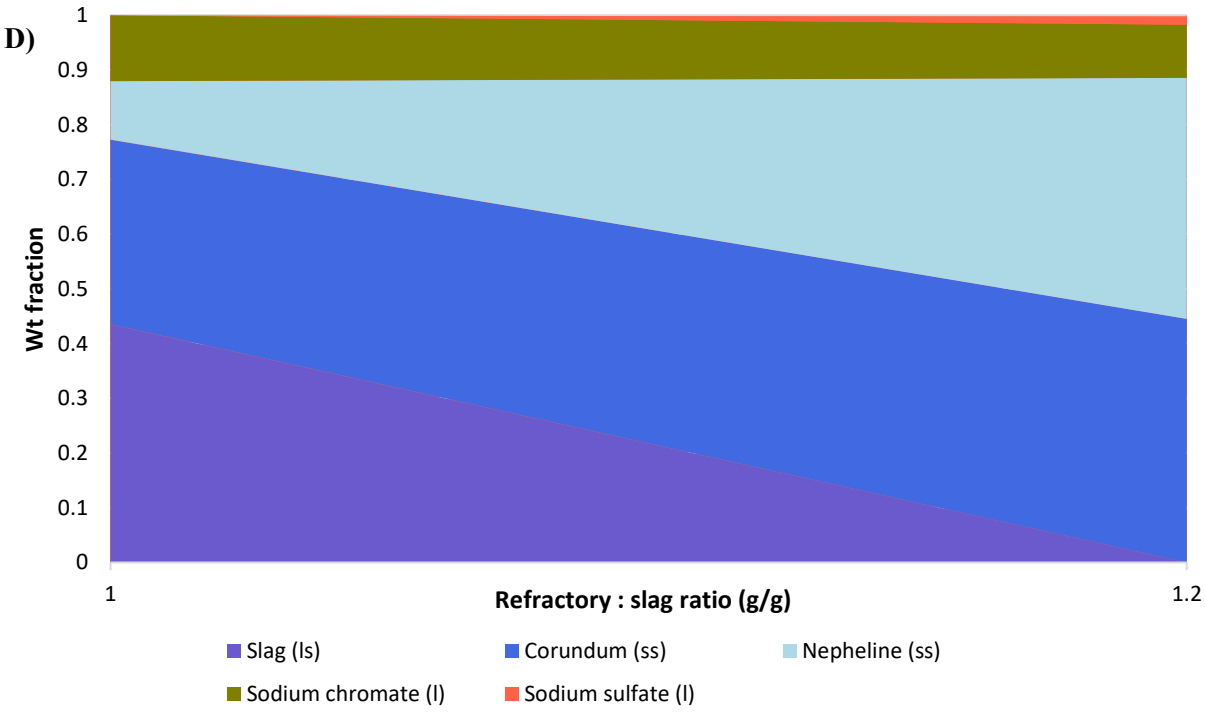
1
0.9
0.8
0.7
0.6
0.5
0.4
0.3
0.2
0.1
0
Wt fraction
1
1.2
Refractory : slag ratio (g/g)
Slag (ls)
Corundum (ss)
Nepheline (ss)
Sodium chromate (l)
Sodium sulfate (l)

E)

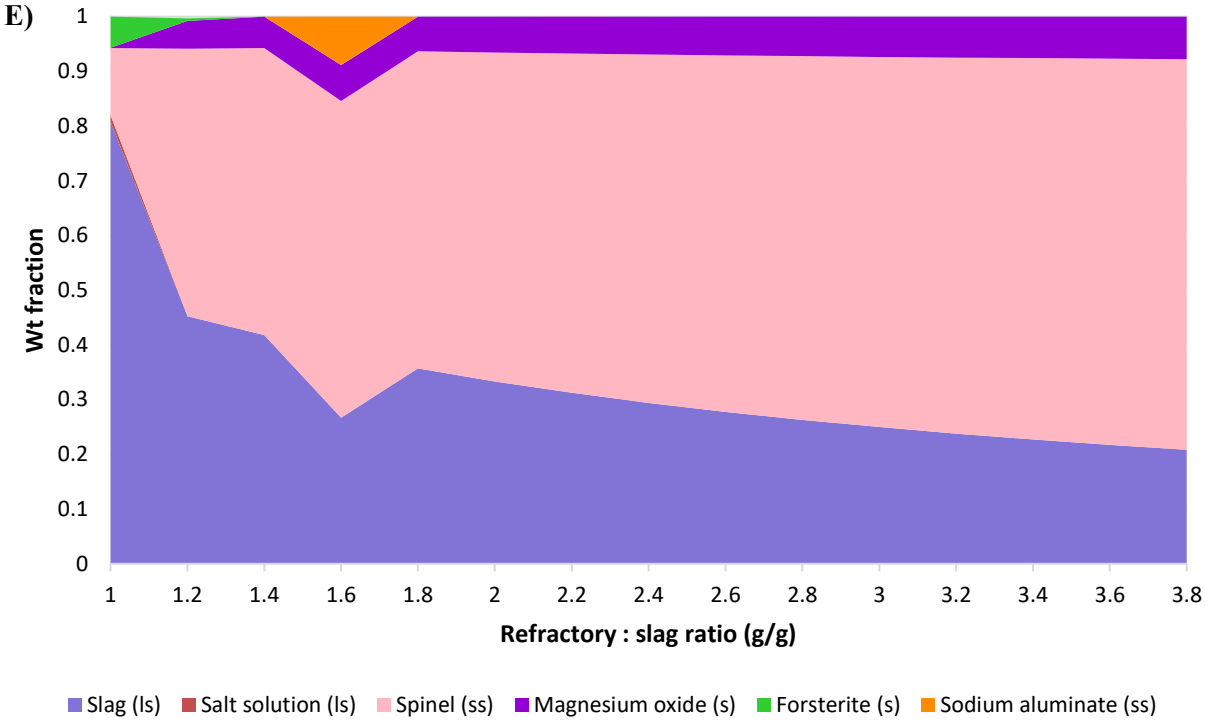
Wt fraction
1
0.9
0.8
0.7
0.6
0.5
0.4
0.3
0.2
0.1
0
1
1.2
1.4
1.6
1.8
2
2.2
2.4
2.6
2.8
3
3.2
3.4
3.6
3.8
Refractory : slag ratio (g/g)
Slag (ls)
Salt solution (ls)
Spinel (ss)
Magnesium oxide (s)
Forsterite (s)
Sodium aluminate (ss)

F)

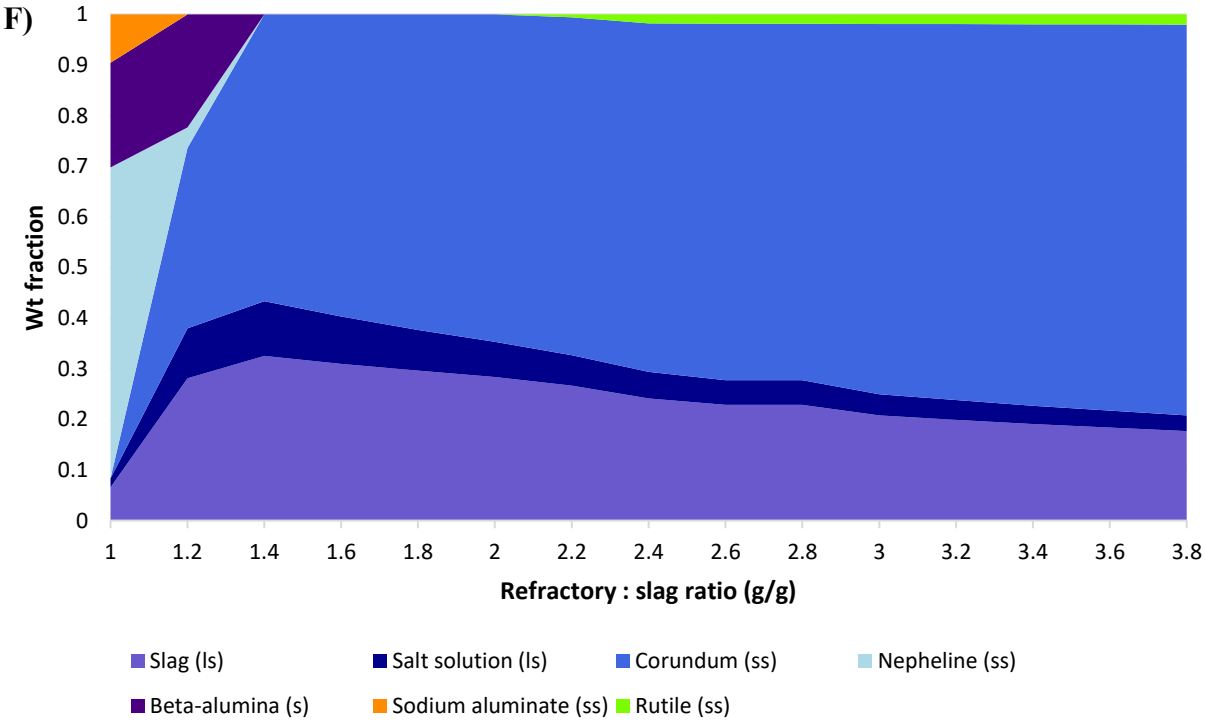
Wt fraction
1
0.9
0.8
0.7
0.6
0.5
0.4
0.3
0.2
0.1
0
1
1.2
1.4
1.6
1.8
2
2.2
2.4
2.6
2.8
3
3.2
3.4
3.6
3.8
Refractory : slag ratio (g/g)
Slag (ls)
Salt solution (ls)
Corundum (ss)
Nepheline (ss)
Beta-alumina (s)
Sodium aluminate (ss)
Rutile (ss)

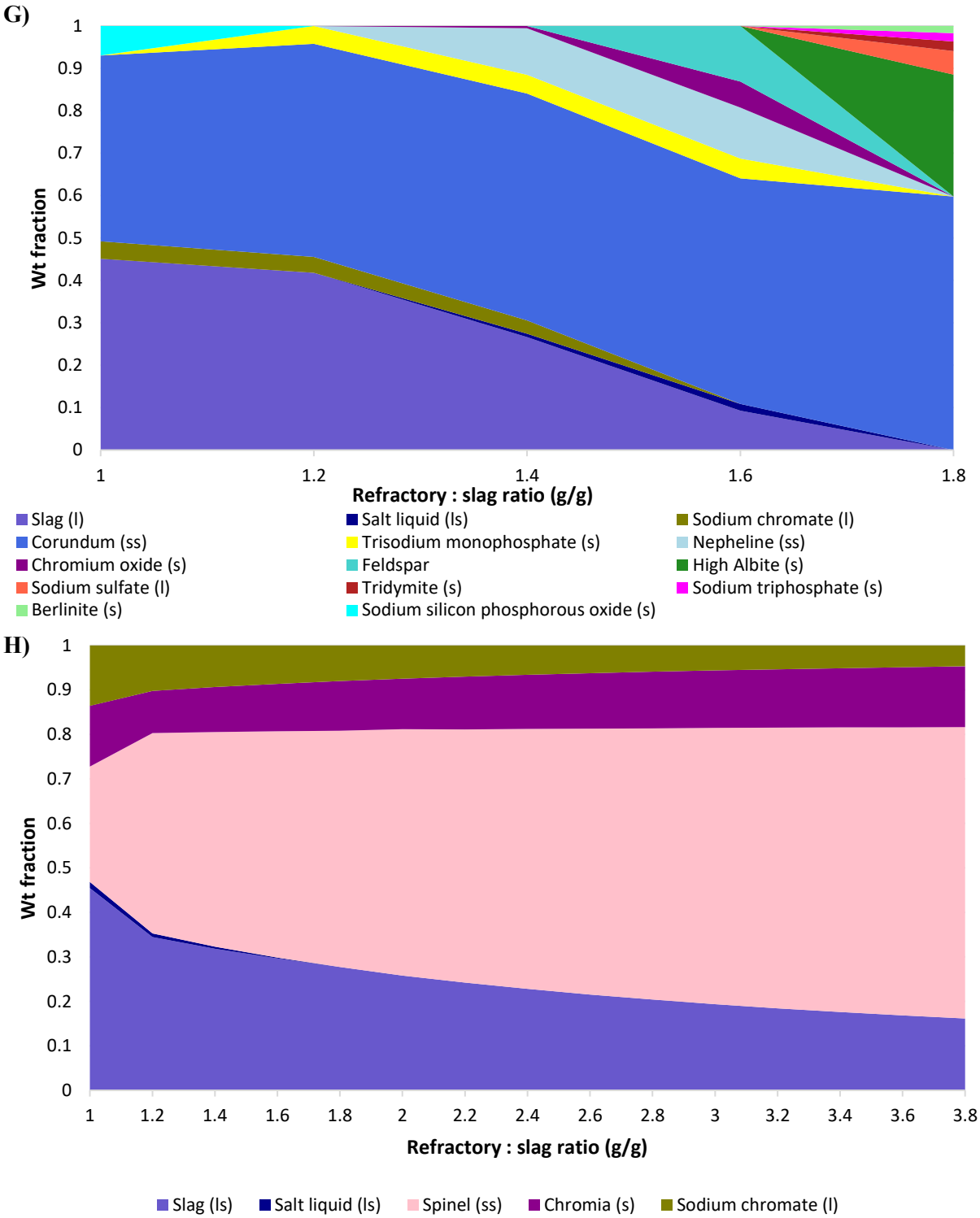

Figure 2-S4. Phases formed during the stepwise addition of A) R1 with Slag 2; B) R1 with Slag 3; C) R2 with Slag 2 ; D) R3 with Slag 2; E) R4 with Slag 2; F) R5 with Slag 2; G) R6 with Slag 2 and; H) R7 with Slag 2 at 55 bar(g). Simulations with Slag 2 were at a temperature of 1250 °C, and the simulation with Slag 3 was at 1600 °C. Phases less than 1 wt % are excluded.

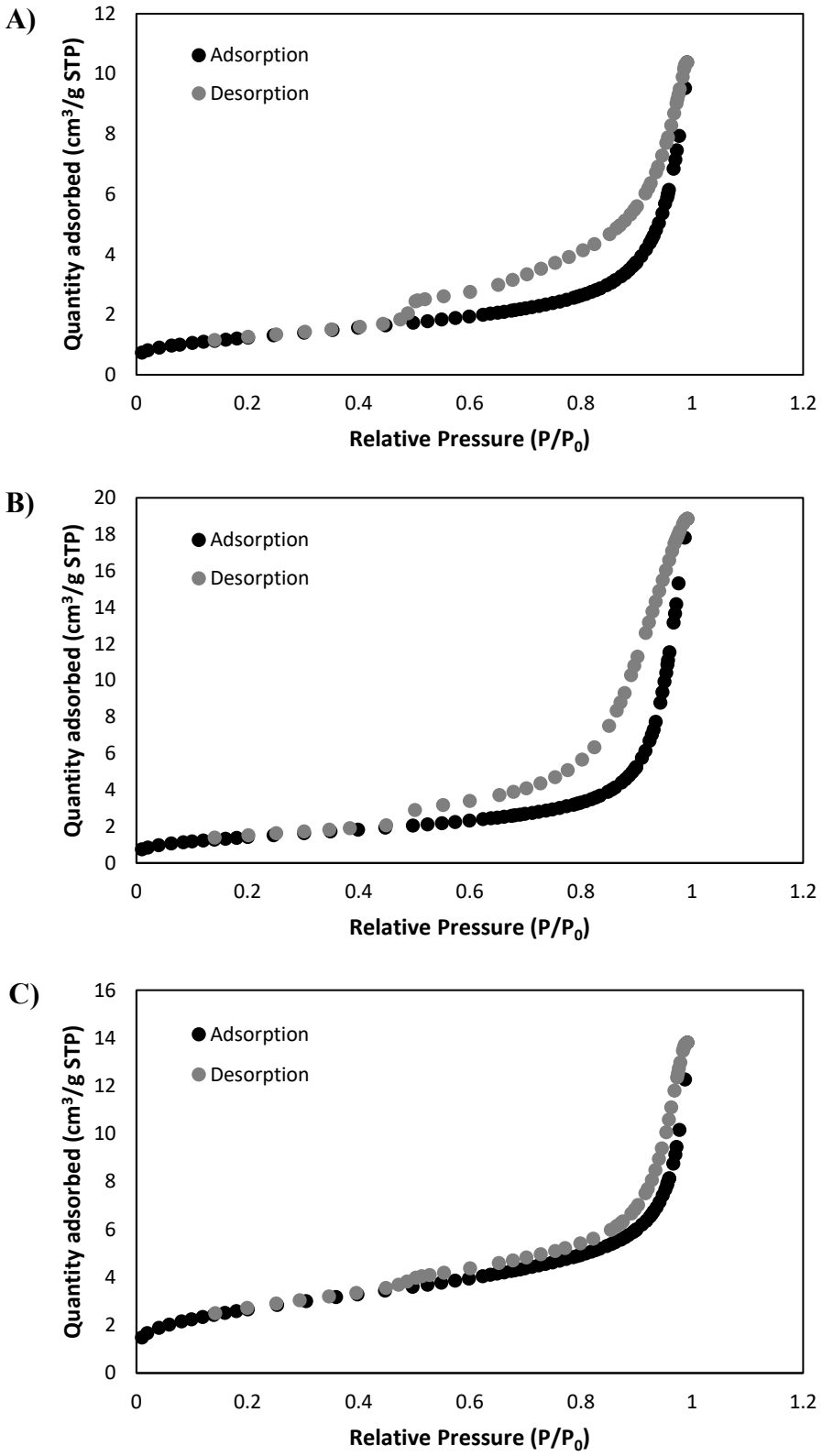

Figure 2-S5. BET isotherm plot for A) R1; B) R2 and C) R3.

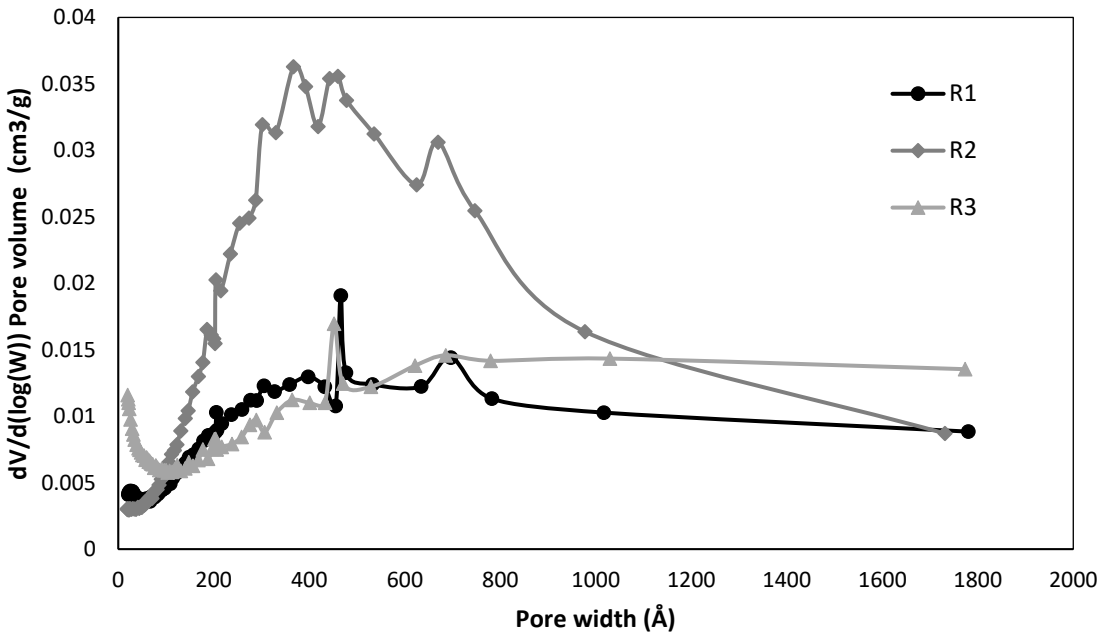

Figure 2-S6. Pore size distributions by volume of refractory materials characterized by the BJH model.

Table 2-S1. BET specific surface area, BJH adsorption cumulative pore volume and BJH adsorption average pore width of refractory materials.

Parameter	R1	R2	R3
Specific surface area (m^2/g)	4.42	5.20	9.58
Cumulative pore volume (cm^3/g)	0.016	0.029	0.021
Average pore width (4V/A) (Å)	154	215	107

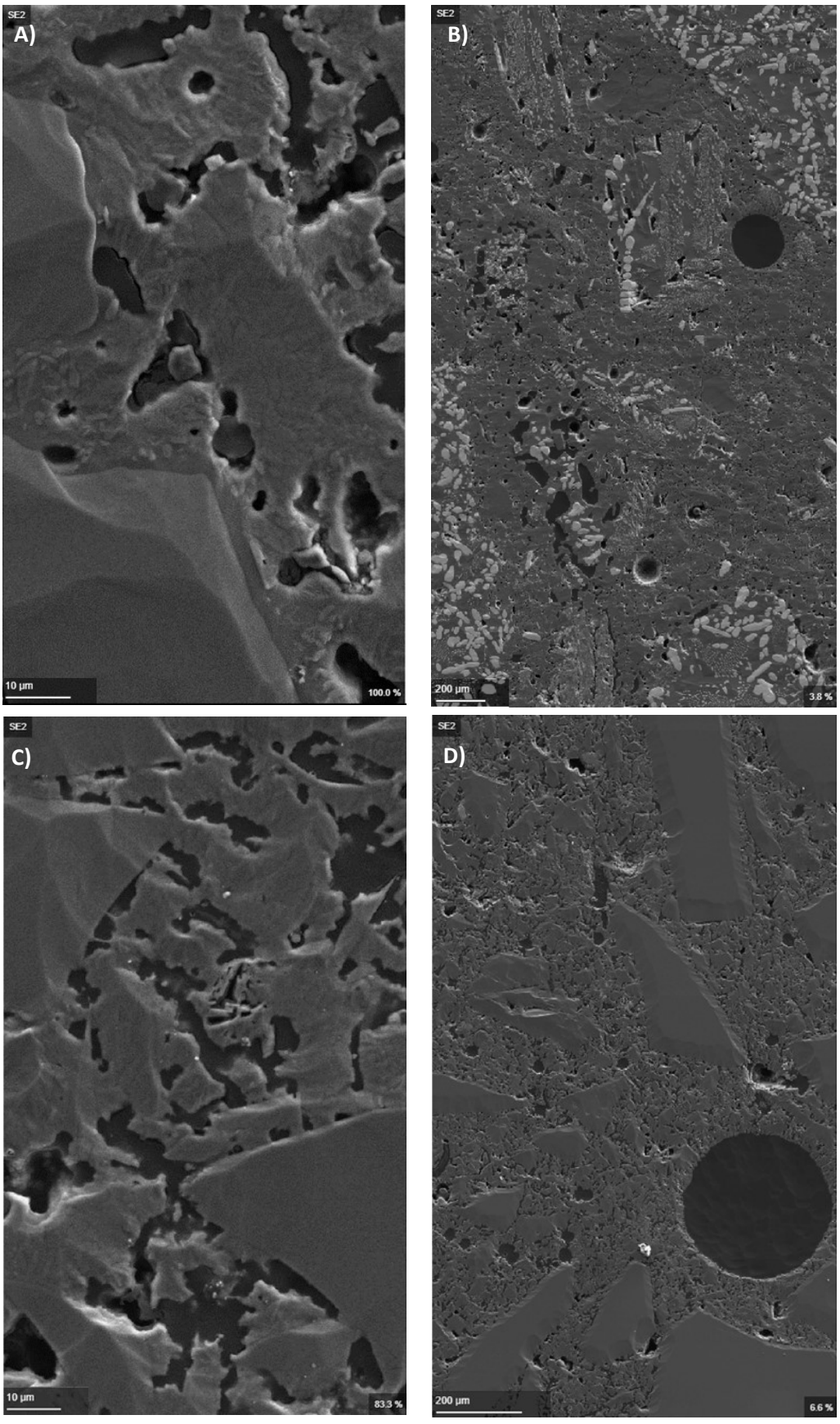
SE2
A)
10 µm
100.0 %
SE2
B)
200 µm
3.8 %
SE2
C)
10 µm
83.3 %
SE2
D)
200 µm
6.6 %

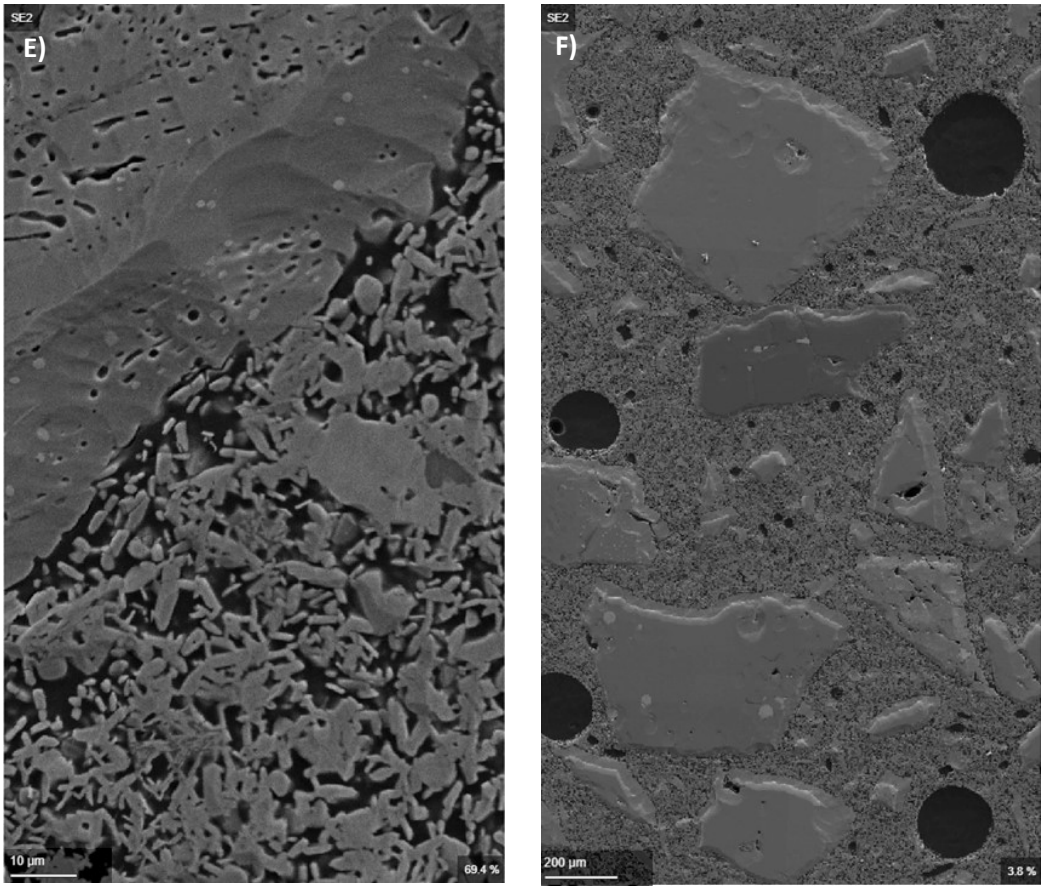

Figure 2-S7. SEM images showing R1 (A, B), R2 (C, D) and R3 (E, F) at high (A, C, E) and low (B, D, F) magnification.

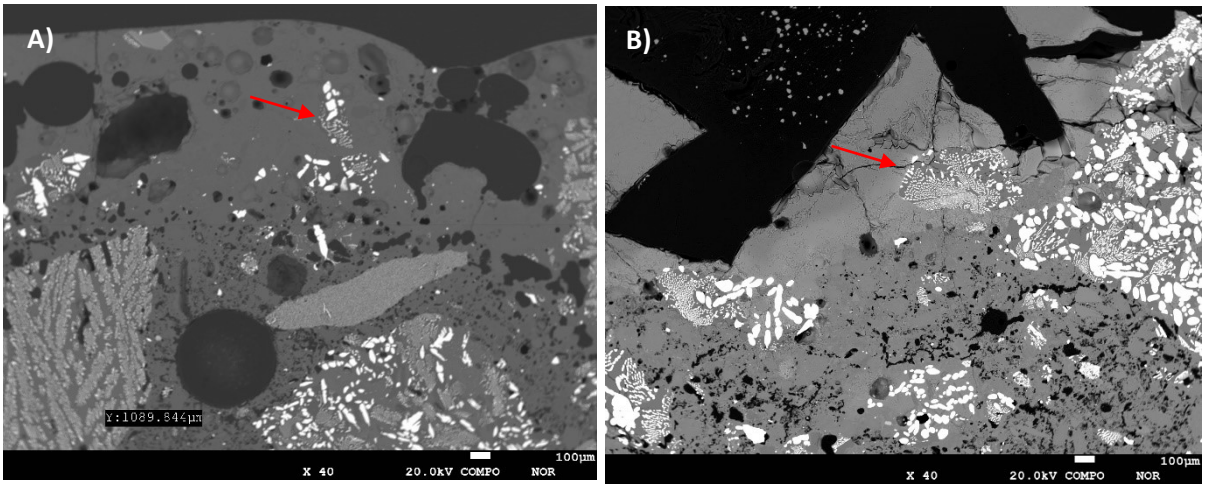

Figure 2-S8. Comparison of cross-section of slag-refractory interface between corrosion tests with Slag 2 and R1 using A) the sessile drop and B) the cup corrosion method. Arrows indicate dislodged zirconia grains as a result of dissolution of the binder phase.

2.7.3 References for supplementary data

[1] M. A. Duchesne and R. W. Hughes, “Slag density and surface tension measurements by the constrained sessile drop method,” *Fuel*, vol. 188, pp. 173–181, Jan. 2017, doi: 10.1016/j.fuel.2016.10.023.

Chapter 3. Direct contact steam generation for surface mining: Behaviour of inorganic phases in the combustor

3.1 Abstract

Oxy-direct contact steam generation is a technology that can be used both to produce steam with lower greenhouse gas emissions than traditional once-through steam generators and to treat the water from oil sands mining operations. Steam is produced by injecting process water, in this case mature fine tailings (MFT) blended with oil-sands processing water (OPW), directly into the combustor along with oxygen and fuel at high pressure. The high inorganics content of the MFT-OPW, the high liquidus point of the deposits (>1600 °C) and the high viscosity of the deposits pose challenges in operation of the combustor. To decrease the liquidus point and viscosity of the MFT-OPW slag, dolomite, limestone and fluorite were considered as fluxants. Based on models, an optimal dolomite concentration of 20 wt % $CaMgO_2$ in the slag was selected. Measurements on a synthetic slag preparation confirmed that at temperatures ≥ 1300 °C, the viscosity of the fluxed slag is ≤ 25 Pa·s. Based on the identified properties of the fluxed slag, a number of refractory materials were assessed for their corrosion resistance through modelling and laboratory-scale experimental work. Of the three refractories tested, chromia-corundum offered the greatest resistance to penetration by the slag, while mullite-zirconia was penetrated most deeply, particularly by Na_2O. Aluminosilicate refractories should be avoided due to their potential to form low-density solid phases upon reaction with the alkalis in the slag, which could lead to damage of the refractory. Magnesium aluminate spinel ($MgAl_2O_4$) and chromia spinel ($MgCr_2O_4$) also offered promising results in the models and warrant further testing.

3.2 Introduction

One of the major environmental concerns associated with Canadian oil sands operations is in the creation of tailings ponds. For every cubic meter of oil sands that is mined, approximately 0.25 m^3 of waste water is added to a tailings pond [1]. The largest water demand in mining operations is for the hot water extraction process, and while much of this demand (80-85 %) is met by recycled process water, fresh water requirements are still high and tailings ponds continue to grow [2]. In 2015, approximately 180 km^2 of land in Alberta was occupied by tailings ponds and only 1 % of that area had been reclaimed [1]. In addition to land use, tailings ponds raise concerns associated with toxicity to aquatic life (mainly due to naphthenic acids), seepage into and contamination of groundwater, and release of greenhouse gases. Due to the slow consolidation of tailings ponds, and the build-up of contaminants in recycled process water that can decrease bitumen extraction efficiency, on-going research in tailings water treatment and reclamation is of high importance to the oil sands industry [2], [3].

Oxy-direct contact steam generation (DCSG) is a high pressure, oxygen-fired process under development by CanmetENERGY-Ottawa that produces steam through direct contact of fuel and an oxidant with an untreated water source. This process has many advantages, including decreased greenhouse gas (GHG) emissions, decreased feed water treatment requirements and decreased fresh water consumption relative to steam production through traditional once-through steam generators (OTSG) [4]–[6]. As a means of both producing steam for mining operations, while also consuming water from existing tailings ponds, DCSG was investigated herein for use with mature fine tailings water (MFT). Produced steam can be used to heat the water required for the hot water extraction process, which separates the mined bitumen from sand and clay [7], [8]. MFT typically has a high solids content (30-35 wt % after settling for several years) and is rich in clays such as kaolinite and muscovite. It also contains sand, dissolved salts and residual bitumen [2]. Due to the

high solids content (and resultant high inorganics content) of the water, deposition prediction and management within the DCSG combustor becomes increasingly important. Fouling on surfaces can lead to poor heat transfer out of the vessel, creating over-temperature situations, can cause plugging of the vessel, and can contribute to corrosion of the refractory lining [9]. To partially counteract the operational challenges associated with the high solids content, the MFT can be diluted with other wastewater from oil sands operations, avoiding the use of further fresh water for steam production.

This work studied the deposits resulting from injection of MFT combined with oil sands processing water (OPW) into the DCSG combustor in order to define a potential operating state for the combustor. The MFT-OPW resulted in deposits with a high liquidus point and viscosity, therefore, a number of fluxing agents were considered for co-injection. Fluxants are commonly used in steelmaking and slagging combustion and gasification to reduce the viscosity of the slag and increase the solubility of impurities. This reduction of viscosity occurs when the ions in the fluxant disrupt the network structure of the slag. In silicate melts, these so-called "network modifiers" prevent close-packing of atoms in the tetrahedral silica network. Ions that are considered network modifiers and thus may be candidates for fluxing agents are Ca^{2+}, Na^{+}, K^{+}, Mg^{2+}, Fe^{2+}, Cr^{3+}, Ti^{4+}, V^{5+}, Ba^{2+} and Sr^{2+} [10]. Common materials used as fluxants include limestone, dolomite and fluorite. Limestone and dolomite were considered as the main contenders due to their availability in proximity to the oil sands operations and low cost. This work further studied refractory corrosion by fluxed inorganic deposits to choose an appropriate refractory lining for the DCSG combustor in this application.

3.3 Materials and Methods

3.3.1 Process water and refractory materials

Oil-sands processing waters were obtained from commercial operations in Western Canada. Table 3-1 shows the inorganic composition of the suspended and dissolved solids in OWP, MFT, and the 96 wt % OPW – 4 wt % MFT mixture used for this work. While representing very little of the total fraction of the mixture, the suspended and dissolved inorganics in the MFT comprised > 90 % of the total inorganics in the mixture. Thus, the actual dilution factor employed could be optimized to maximise MFT usage based on the solids handling capabilities of the plant with negligible impact on the slag composition or behaviour. Literature values for the average composition of pond recycle water (RCW) have also been provided for comparison to the OPW used in this work, and are shown to be quite similar.

Table 3-1. Composition of major solid and dissolved inorganic species in oil sands produced waters (carbon and oxygen-free basis). Species representing ≥ 1 wt% of total inorganics are shown.

	OPW[1]	**MFT[2]**	**MFT-OPW[3]**	**RCW**[11]
Species		**Wt %**		
Cl	46		11	41
K		6	3	
Na	45		11	57
S	5			3
Si	1	64	51	
Al		26	20	
Fe		4	3	
N	2			
Total inorganics mg/kg water (excluding O and C)	1670	141500	7260	1145

[1]Composition determined by ICP-AES.
[2]Composition determined through drying of water sample and characterization of solids *via* x-ray fluorescence (XRF) according to ASTM D4632.
[3] Calculated composition for mixture containing 4 wt % MFT and 96 wt % OPW.

Table 3-2 shows the chemical composition of the refractory materials used in corrosion modelling and laboratory testing. Refractories R1-R3 were pre-cast into blocks by the manufacturers prior to

testing. The dimensions of the blocks were 0.1 m x 0.1 m x 0.1 m. Where smaller pieces were required, the blocks were cut with a wet saw and rinsed with water to remove cutting dust. Samples were dried at ambient conditions before experiments commenced.

Table 3-2. Composition of refractory materials for modelling and experimental testing.

Refractory Material:	**Mullite-zirconia[1]**	**Silicon carbide[2]**	**Chromia corundum[3]**	**Magnesium aluminate spinel[4]**	**Chromia spinel[6]**
Refractory ID:	**R1**	**R2**	**R3**	**R4**	**R5**
Component			**Wt %**		
Al_2O_3	51.3	20.6	24.7	64.7	
SiO_2	21.3	14.7	0.2		
ZrO_2	19.5				
SiC	3.9	62.1			
CaO	1.5	2.2	0.1		
MgO				35.3	17.4
Cr_2O_3			74.8		82.7
TiO_2	0.4				
Fe_2O_3		0.2	0.1		
P_2O_5					
Alkalies	1.5	0.2			
Other	0.3		0.1		

[1]Composition provided by manufacturer [12].
[2]Composition given by manufacturer [13].
[3]Composition provided by manufacturer [14].
[4]Composition given by Carlborg et al. excluding species < 1wt % [15]
[5]Composition given by Bennett *et al.* excluding species < 1 wt % [16].

3.3.2 Thermodynamic simulations

The Equilib module of FactSage (version 7.2 to 8.0) [17] was used for thermodynamic simulations of deposition prediction and refractory corrosion. All gases, pure solids and solution phases in the FactPS, FToxid and FTpulp databases were considered unless otherwise indicated. The SLAGA solution phase from the FToxid database was used to model the slag solution, since it is the best-optimized slag solution in FactSage and considers all relevant species. The MELTA solution phase

of the FTpulp database was selected to provide the best-optimized thermodynamic solution for the major phases identified within the salt, when present.

3.3.2.1 Deposition models

All feeds to the combustor were entered into the Equilib module at 55 bar(g) to determine the composition of the slag phase and/or other phases at the temperature of interest. On a basis of 1000 kg/h of process water (OPW, MFT or MFT-OPW), which includes the solid and dissolved inorganic species listed in Table 3-1, the other combustor feeds were 124 kg/h of natural gas (97 mol % CH_4, 2 mol % C_2H_6, and 1 mol % C_3H_8) and 494 kg/h of oxygen. The energy and mass balances performed to define these flow rates have been described previously (Section 2.3.2.1). When fluxants were considered, the calcined fluxant (CaO when limestone is used, $CaMgO_2$ when dolomite was used, or CaF_2 when calcium fluoride was used), was added in addition to the above flow rates to reach the desired weight percent of fluxant in the new slag phase.

3.3.2.2 Molten slag penetration models

The method of performing the slag penetration models has been described in detail previously (Section 2.3.2.2). To summarize, a step-wise addition of the slag phase to increasing amounts of refractory was performed in FactSage to simulate the incremental penetration of the slag into the refractory. The first step combined an equal amount of slag and refractory (100 g). For each subsequent step, the mass of refractory was increased by 20 g. The mass of the liquid phase was held constant, but the composition was updated at each step - the output composition of the slag phase in the previous step was used as the input for the next step. This proceeded until either no liquid phase remained, making it impossible to continue, or until 15 calculation steps (corresponding to a slag to refractory ratio of 3.8 g refractory/g slag) were completed. For cases with non-fluxed MFT-OPW, only the fraction of the inorganics that are liquid at the selected

temperature and pressure (based on FactSage deposition models) were used as the input for the first step of the penetration models.

3.3.2.3 Refractory dissolution models

Refractory dissolution was modelled through calculation of the metastable diffusion factor of each major refractory phase (phases ≥10 wt % of the total refractory were considered) within the slag phase. The phases within each refractory at the temperature and pressure of interest were modelled using FactSage based on the refractory compositions in Table 2-2.The metastable diffusion factor depends on the temperature, viscosity, and change in concentration of the dissolved refractory between the initial and saturated slag. FactSage was used to determine the concentration of dissolved refractory in the slag at saturation. Starting with 100 g of slag, increasing amounts of the refractory phase of interest were added to the solution until the precipitation of the first solid. Only the initial slag phase, the refractory phase being added, and a gas phase were permitted to form in FactSage, hence the arrival at the "metastable" diffusion factor. This method has been previously described in more detail (Section 2.3.2.3).

3.3.3 Slag viscosity modeling

The slag viscosity database from the Slag Viscosity Modeling Toolbox [18] was used to find similar slag compositions to those modeled in this work. A series of viscosity models were applied to those compositions and the results were compared to the associated literature viscosity values within the database. The viscosity model that resulted in the minimum average absolute logarithmic error (AALE) between the literature value and the predicted value was finally applied to the new slag compositions in this work.

3.3.4 Synthetic slag preparation

Na_2CO_3, K_2CO_3, Al_2O_3, SiO_2, Fe_2O_3, $CaCO_3$ and MgO powders (Sigma Aldrich) were combined to create the slag solutions predicted by the deposition models. To ensure a homogenous mixture,

the powders were placed in a shaker mixer (Farmalabour) for 4 hours prior to use. Note that carbonates were not included in the slag phase. Under the conditions used for testing, the carbonates in the powders thermally decomposed to release CO_2 and yielded the target slag composition at the temperature of interest.

3.3.5 Liquid property measurement

Viscosity of the synthetic slag preparation was measured using the rotating bob technique. The sample was placed in an alumina crucible and heated in a high-temperature furnace under a constant flow of air to the maximum measurement temperature and the sample was allowed to equilibrate for 45 min. Using an alumina spindle and bob, the slag viscosity was then measured at step-wise temperature decrements. The equipment and full procedure have been described in Section 2.3.5.

The surface tension and density of the synthetic slag were measured using the sessile drop technique. Samples were heated on an alumina substrate in air and the droplet profile was fitted to the Laplace-Young equation as described in Section 2.7.1.1.

3.3.6 Ash fusion tests

An aliquot of the commercial MFT sample was dried to collect the total solids of the sample and ashed at 750 °C in air. To determine the melting behaviour of the sample, "ash" fusion tests were performed on the total solids as per ASTM D1857.

3.3.7 Refractory corrosion tests

3.3.7.1 Cup tests

Synthetic slag powders (60 g) were placed in refractory cups (0.1 m x 0.1 m x 0.076 m block with a central hole drilled 0.055 m wide and 0.55 m deep, with a 0.1 m x 0.1 m x 0.015 m lid) prepared as per Method A in the standard CEN/TS 15418:2006 [19]. The test pieces were heated to 1300 °C in air in a muffle furnace (Thermolyne F46240CM-33) at a rate of 15 °C/min. The temperature

was maintained for 5 hours and then the samples were cooled to room temperature at a rate of no more than 20 °C/min.

3.3.7.2 Sessile drop tests

Pellets measuring 6 mm in diameter and weighing approximately 0.15 g were prepared from the synthetic slag powder under a force of 15.6 kN using a Carver manual press (model #4555.L). A single pellet was placed at the centre of a refractory test piece measuring approximately 15 mm x 15 mm x 10 mm. Test pieces were heated in a muffle furnace under the same conditions described in Section 3.3.7.1.

3.3.7.3 Scanning electron microscopy and energy dispersive x-ray spectroscopy (SEM-EDX)

Following corrosion tests, refractory samples were cross-sectioned using a wet saw and/or a Buehler Isomet low-speed saw. The sample face to be imaged was sectioned with the low-speed saw to obtain a smooth surface. Samples were washed by sonicating them first with dish soap, and then in distilled water. A Pd-Au (60/40) coating was applied to the sample surface for electron conductivity. SEM-EDX analysis was done with a Hitachi S-3400N SEM and Oxford Instruments Si(Li) Pentafet Plus X-Max 20 mm^2 detector. Area scans (approximately 0.2 mm x 0.2 mm, with 0.2 mm spacing between them) were performed vertically from the slag layer down to the bottom of the refractor piece to quantify the elemental composition within each area. Two area scans for each refractory depth at different lateral location were taken for each sample and averaged. This generated a profile of composition relative to penetration depth into the refractory. Elemental compositions were converted to oxide compositions to reflect the base components of the slag and refractory materials.

3.4 Results and Discussion

3.4.1 Deposition models and measured properties of MFT-OPW

FactSage simulations were conducted with the combustor feeds at 55 bar(g) to determine the compositions of deposits for each process water source. As seen in Figure 3-1, the predicted silica content of the MFT slag at its liquidus is very high (72.5 wt %), making the liquidus temperature of the mixture very high as well (>1500 °C based on ash fusion tests). To avoid solids build-up and plugging of the reactor, the combustor would likely have to be operated at an elevated temperature to exceed the liquidus temperature of the mixture and reduce its viscosity sufficiently to achieve a flowing slag layer. This is undesirable because it would reduce the efficiency of the process by decreasing the throughput of MFT that can be treated and the resultant steam production rate for a given firing rate. This operating temperature would also likely approach or exceed the maximum allowable working temperature of common refractory materials; for example mullite zirconia (R1) and SiC (R2) maximum temperatures are respectively 1600 and 1540 °C [12], [13]. This would thus require active wall cooling or other engineering approaches that may further reduce the efficiency of the process. To partially counteract this issue, MFT was combined with a second oil sands produced water – OPW – in a mass ratio of 24:1 OPW:MFT. This water has a much lower solids content (Table 3-1) and serves to dilute the inorganics in the MFT. Some slag is expected to be produced in the combustor at the liquidus with OPW (Figure 3-1), but the majority (92 %) of the liquid phase from this water source is expected to be a low-viscosity molten salt rich in Na_2SO_4, Na_2CO_3, NaCl and NaOH. The resultant slag for the MFT-OPW mixture is expected to again be high in silica, but with dilution by Na_2O.

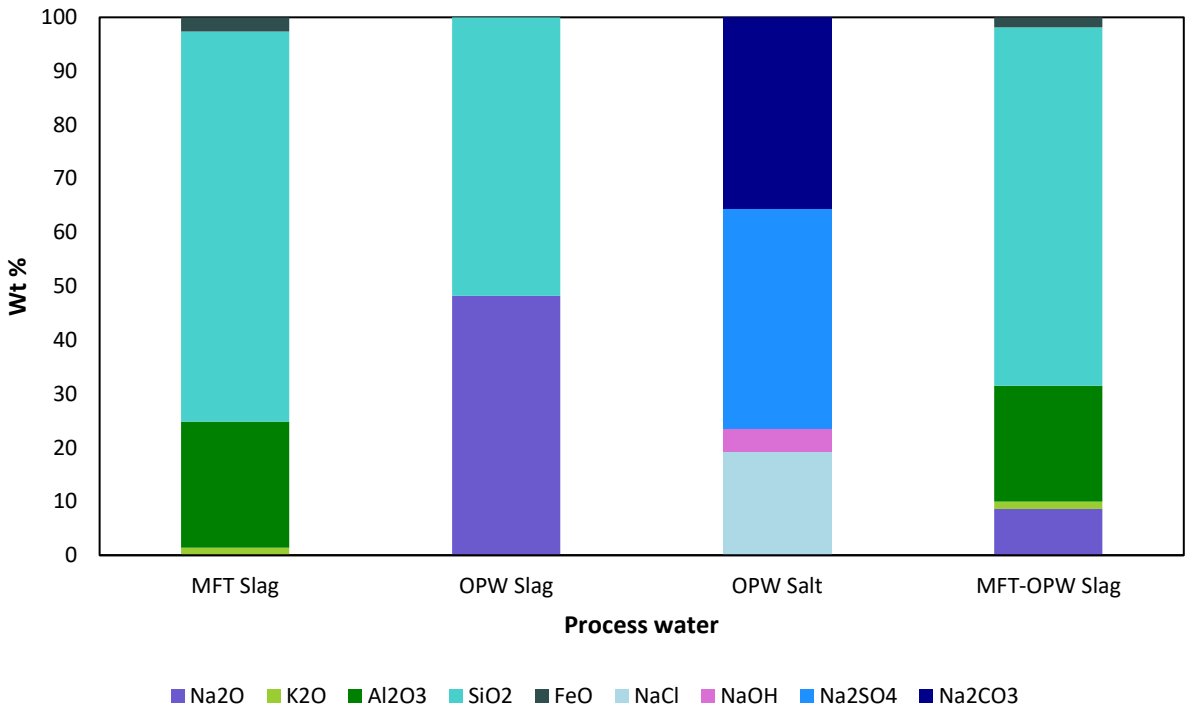

Figure 3-1. Expected compositions of deposits in the DCSG combustor at their predicted liquidus temperatures at 55 bar(g). Species representing <1 wt % are excluded.

Synthetic preparations of the MFT-OPW slag were heated in a tensiometer furnace to assess its properties at high temperature. Figure 3-2 shows images of the pellet during the experiment (A) and after cool-down (B). As an axisymmetric drop was not observed, it is believed that the internal core of the pellet never became liquid throughout the experiment, even at the maximum temperature (1600 °C) of the equipment. Thus it can be assumed that the liquidus temperature of the MFT-OPW mixture is >1600 °C.

Though the total solids loading on the combustor will be significantly less with the mixture rather than MFT alone, the issues discussed previously for MFT remain for operation with the MFT-OPW mixture. To illustrate this problem, Figure 3-3 shows the refractory lining (0.1 m ID) from a pilot-scale test with the MFT-OPW mixture, operating at 55 bar(g) and 240 kW. Temperature probes indicated an average combustor temperature in the range of 1100-1250 °C throughout the

test, but due to the solids accumulation on the probes this cannot be considered accurate. Melted solids in the upper region were believed to be have been melted by passage directly through the flame, which is expected to be at temperatures exceeding 1800 °C, before being deposited on the walls. The temperature gradient in the combustor resulted in a thick build up of slag just below the level of the flame as the viscosity increased, and significant accumulation of solids in the lower region of the reactor of un-melted or partially molten solids that either by-passed the flame or did not have sufficient residence time in the flame.

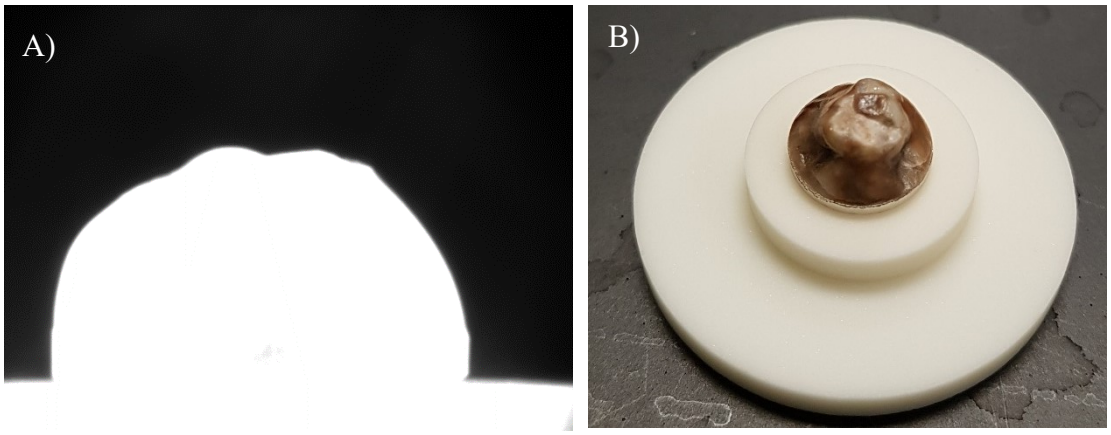

Figure 3-2. Pellet of synthetic MFT-OPW A) at 1600 °C and 1 atm, and B) after cool-down.

Figure 3-3. Refractory lining (0.1 m ID) of DCSG combustor following a pilot-scale test with MFT-OPW. Combustor conditions: 1100-1250 °C, 55 bar(g), 240 kW. Test duration was 100 min.

3.4.2 Selection of fluxant and weight fraction

Based on the results presented in Section 3.4.1, additional measures must be taken to make the DCSG combustor operable with MFT-OPW. One option is the addition of a fluxant that can be co-injected with the MFT-OPW into the combustor. A fluxant can serve to lower the liquidus temperature and viscosity of the slag by modifying its network structure, which would allow the combustor to be operated at a lower temperature without the risk of solids accumulation and

plugging. Three fluxants were considered: limestone, dolomite and fluorite. At increasing weight fractions of fluxant, the resultant liquidus of the mixture was estimated with FactSage, and the viscosity of the mixture was estimated at various potential operating temperatures using the Slag Viscosity Modelling Toolbox [18]. The optimal choice of fluxant minimizes both the amount of fluxant required and the operating temperature of the reactor. An acceptable operating temperature for each mixture was estimated based on the slag viscosity, which according to a common heuristic, should be ≤ 25 Pa·s at the slag tap [20]–[22].

Fluorite was discounted early from consideration after FactSage simulations showed that combination of the fluxant with the MFT-OPW inorganics under DCSG combustor conditions resulted in volatization of the majority of the fluorine. Combining 35 wt % CaF_2 in the total MFT-OPW-CaF_2 inorganics mixture resulted in retention of less than 3 wt % of the fluorine in the slag. The calcium was incorporated in the slag as CaO, thus having a similar effect as the addition of limestone, without the potential of creating gaseous hydrofluoric acid. Due to environmental concerns related to release of fluorine, the scarcity of the mineral, and potential issues with refractory wear, [23], [24] fluorite was not further considered.

Figure 3-4 shows the viscosity of various combinations of MFT-OPW with limestone and dolomite. At the temperatures and pressure considered, both fluxants are in their calcined form. The balance between operating temperature and the amount of flux used will be an economic decision, however, for this preliminary work it is assumed that the optimal operating temperature of the combustor is 1300 °C. For limestone, the resultant slag mixture must contain more than 35 wt % CaO to be operable in terms of generating a steady-flowing slag layer to avoid accumulation of inorganics and plugging (Figure 3-4A). For dolomite, the slag mixture must contain at least 20 wt % $CaMgO_2$ (Figure 3-4B). Thus, dolomite is the clear choice in minimizing the amount of

fluxant, though limestone could be considered if dolomite is not available in close proximity to the commercial facility.

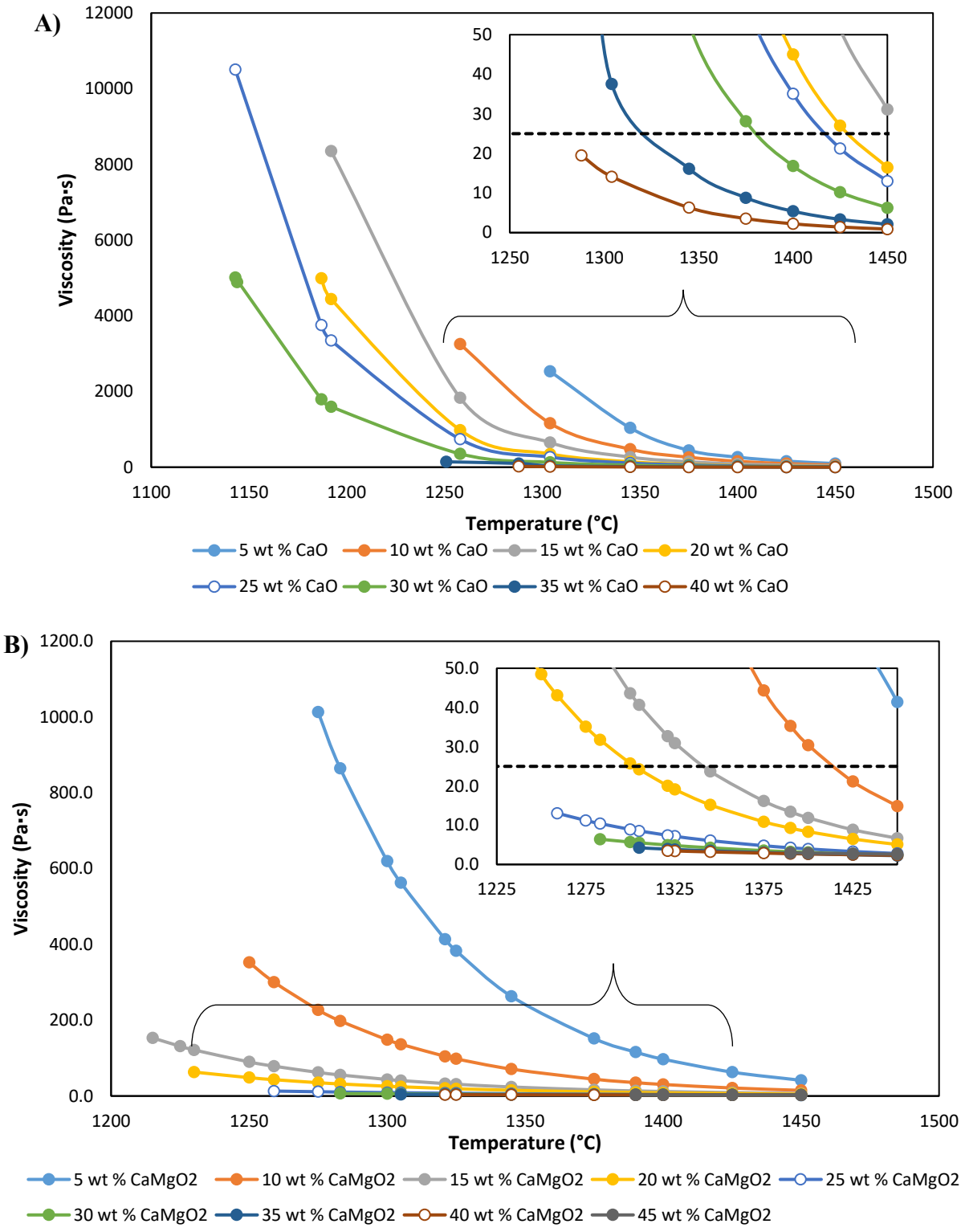

Figure 3-4. Modelled viscosity of MFT-OPW slag fluxed with A) limestone and B) dolomite as a function of temperature. The Duchesne viscosity model was applied [18]. The lowest temperature at which viscosity is modelled for each mixture represents the liquidus as estimated with FactSage. The horizontal dashed line indicates the viscosity target of 25 Pa·s.

3.4.3 Physical properties of fluxed MFT-OPW

The physical properties of the MFT-OPW slag fluxed with 20 wt % $CaMgO_2$ were confirmed with bench-scale experiments. In addition to the slag's ability to flow and prevent plugging, its viscosity as well as its surface tension impact the depth at which a slag may penetrate a refractory material in a fixed time period [25]. Figure 3-5 shows the surface tension and density of the mixture as measured using the sessile drop technique. The density does not show the expected trend, as it is seen to gradually increase with temperature. This may be a result of small bubbles trapped in the slag at lower temperatures, making the total droplet volume appear larger, which then coalesced with the gas-sample interface and escaped as the experiment continued and the sample was heated further. The liquidus point was visually estimated to be in the range of 1275-1300 °C during the same experiment. This liquidus is approximately 50 °C greater than expected from the FactSage models in Section 3.4.2, however, viscosity measurements (Figure 3-6) show that the 25 Pa·s operational threshold is reached at a temperature of 1300 °C, the same temperature predicted by the models. Further, the Duchesne *et al.* model [18] is shown to be a good fit for this composition, particularly at temperatures above 1200 °C, with an AALE of 0.045 over the entire measurement range.

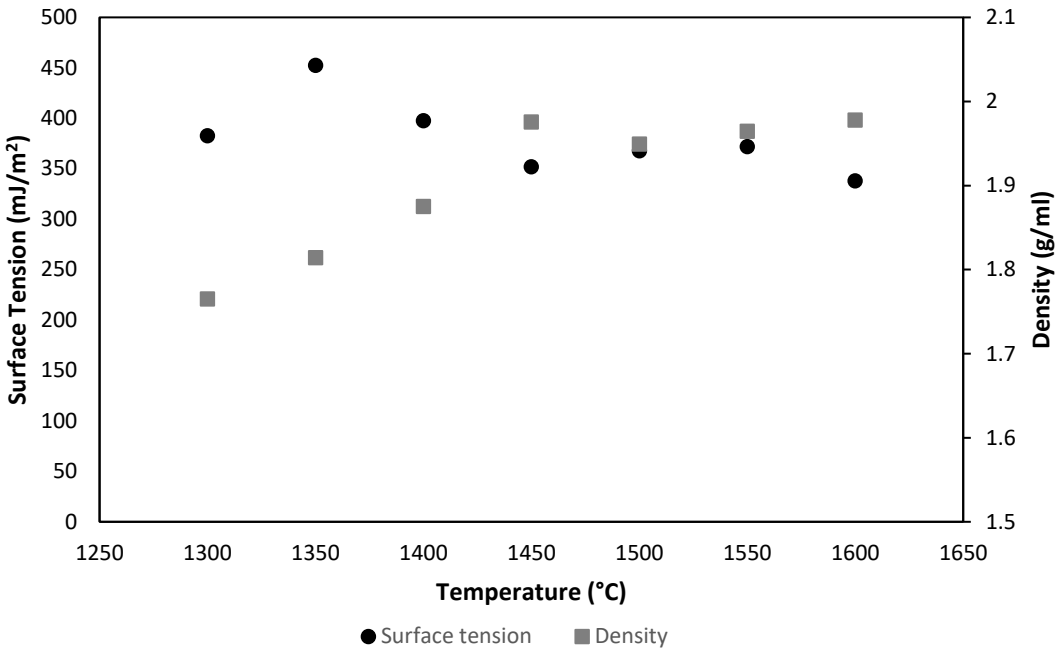

Figure 3-5. Surface tension and density of MFT-OPW fluxed with 20 wt% $CaMgO_2$. Measurements were performed in air at atmospheric pressure. Data points are the average of 5 repeat measurements. Coefficient of variation < 4 %.

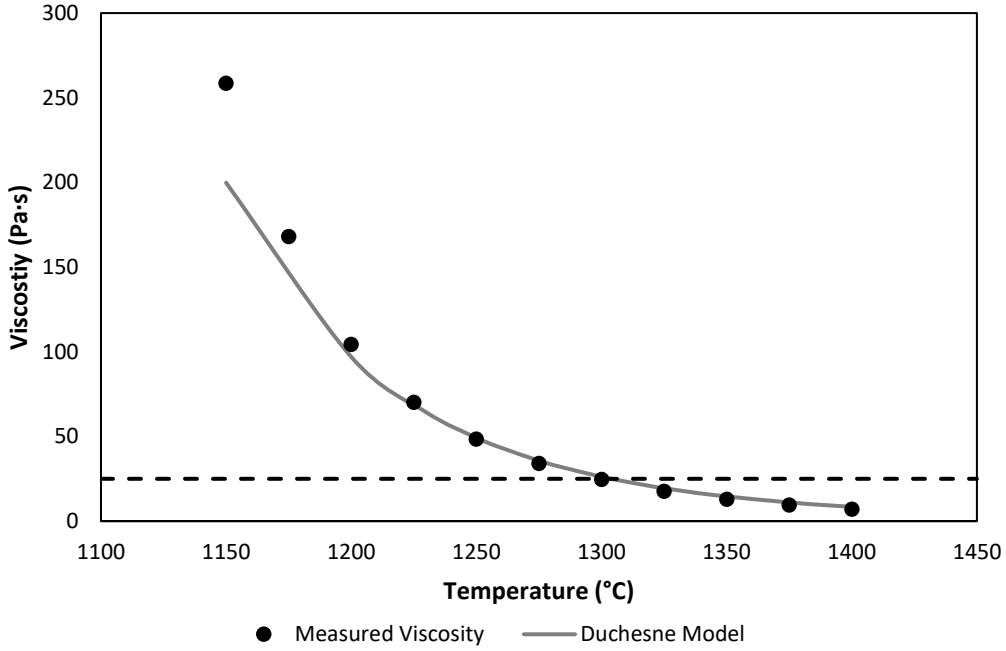

Figure 3-6. Measured and modelled viscosity of MFT-OPW fluxed with 20 wt% $CaMgO_2$. Measurements were performed in air at atmospheric pressure. Data points are the average of 9 repeat measurements. Coefficient of variation < 3%. Model predictions were done with the Duchesne *et al.* model [18].

3.4.4 Refractory corrosion models

Five refractory materials were assessed through corrosion modelling. The fluxed MFT-OPW slag is comparable to those resulting from coal or petcoke combustion or gasification, in that it its major constituent is silica, with significant portions of alumina, lime and magnesia [26]–[28]. The main difference between the fluxed MFT-OPW slag and typical coal slags is the lower content of iron oxide and higher fraction of sodium oxide. For coal conversion systems, high chrome oxide refractory materials are found to be the most resistant to corrosion [29], [30], and additionally it has been found that chromium-based refractories with Cr embedded in a magnesia spinel lattice have improved corrosion and vaporization resistance compared to refractories with free Cr_2O_3 [31]. For this reason, two of such refractories were chosen for evaluation (R3 and R5). A magnesium aluminate spinel (R4) was also considered since it is possible the spinel lattice may offer the same protective effects as R5 without the higher cost and environmental concerns associated with chromia-based refractories. Silicon carbide refractories have also shown good resistance in coal combustion and waste incineration [32], [33] and thus R2 was included in the evaluation.

The slag studied herein also shares similarities with slag and ash resulting from biomass conversion, albeit with sodium oxide instead of potassium oxide as the major alkali species [34]–[37]. Based purely upon the base to acid ratio (defined by Vargas [10]), one would determine that the fluxed MFT-OPW slag is acidic and thus should be paired with an acidic or neutral refractory composed of species such as silica or alumina. For this reason, R1 was included, though based on previous literature studies of high-alkali biomass slag with aluminosilicates, it is expected to perform poorly compared to the other refractory materials [15], [38], [39].

The slag penetration models show the phases that may form as a liquid slag phase travels into a refractory material through cracks and pores. This model considers only thermodynamic equilibrium and does not factor in the physical properties of the liquid solutions such as their viscosity and surface wettability, both of which will also contribute to the total depth that a slag may penetrate into a refractory material in a given time [25]. Thus, while Table 3-3 shows a similar number of calculation steps can be completed for penetration of the fluxed and non-fluxed slag into each refractory material, when physical properties are taken into account, the non-fluxed slag is not expected to penetrate as deeply due to its much higher viscosity. The key outcome of these models is to predict if there is the potential for low-density solids to form within cracks and pores of the refractory, which can cause damage through volume expansion and severely limit the service life of the refractory [15]. Contrarily, rapid formation of high-density solids may indicate good corrosion resistance of the refractory by sealing off the surface from further attack [16], [40].

As summarized in Table 3-3 and detailed in Figure 3-S1 & 3-S2, the formation of feldspar was consistently predicted throughout the calculation steps for R1 and R2 with both fluxed and non-fluxed slags; this could be problematic due to the lower density of feldspar relative to the bulk refractory material. Simulations with R3 result in formation of feldspar only with the fluxed slag, however, since it appears only in the first calculation step (Figure 3-S3), it is expected to form only near the refractory surface and may not cause damage. Additionally, this combination of refractory and slag also results in the formation of a dense spinel phase, which is hypothesized to form a protective layer on the refractory and prevent further slag infiltration [31]. Similar to R3, all liquid phases are consumed after the first two calculation steps and there are no low-density (<3 g/cm^3) solid phases formed for R4 and R5 (Figures 3-S4 and 3-S5) with either the fluxed or non-fluxed

slag. Thus, R3, R4 and R5 all may be good candidates for the DCSG combustor refractory lining when using MFT-OPW.

Table 3-3. Phases formed with the step-wise slag penetration simulations at 55 bar(g) and 1300 °C for MFT-OPW with and without 20 wt % $CaMgO_2$ added as flux. New phases that are not predicted to be in the untreated refractory material at equilibrium are indicated in red.

Refractory:			**R1**		**R2**		**R3**		**R4**		**R5**	
Fluxant (Yes/No):			**N**	**Y**	**N**	**Y**	**N**	**Y**	**N**	**Y**	**N**	**Y**
Phases Formed	**Chemical Formula**	**State[1]**										
Slag	-	ls	**X**	**X**	**X**	**X**	**X**		**X**	**X**	**X**	**X**
Mullite	$Al_6O_{13}Si_2$	ss	X	X	X	X						
Feldspar	$(K,Na,Ca)(Al,Si)_4O_8$	ss	**X**	**X**	**X**	**X**		**X**				
Zirconia	ZrO_2	s	X	X								
Graphite	C	s	**X**	**X**	**X**	**X**						
Silicon carbide	SiC	s	X	X	X	X						
Iron silicide	FeSi	s	**X**	**X**	**X**	**X**						
Zircon	$ZrSiO_4$	s	**X**									
Tridymite	SiO_2	s			X	X						
Corundum	$(Al,Cr,Fe)_2O_3$	ss					X	X			**X**	
Metal oxide solution	$(Na)(Al,Fe)O_2$	ss					**X**	**X**		**X**	**X**	**X**
Sodium chromate	Na_2CrO_4	s					**X**					
Sodium chromite	$(Na_2O)(Cr_2O_3)$	s					**X**	**X**			**X**	**X**
Potassium chromium (III) oxide	$KCrO_2$	s					**X**	**X**			**X**	**X**
Beta-alumina	$NaAl_9O_{14}$	s					**X**	**X**	**X**		**X**	**X**
Beta-alumina	$Na_2Al_{12}O_{19}$	s								**X**		
Mono-potassium aluminum oxide	KAl_9O_{14}	ss							**X**			
Di-potassium aluminum oxide	$K_2Al_{12}O_{19}$	s								**X**		
Sapphirine	$Mg_4Al_{10}Si_2O_{23}$	s		**X**								
Cordierite	$Al_4(Mg,Fe)_2Si_5O_{18}$	ss				**X**			**X**			
Magnesium aluminate spinel	$(Mg,Al)(Al,Cr)_2O_4$	ss						**X**	X	X	X	X
Sodium calcium aluminum oxide	$Na_2(Na_2,Ca)Al_4O_8$	ss						**X**	**X**	**X**	**X**	**X**

Refractory: **Fluxant (Yes/No):**			**R1** **N**	**Y**	**R2** **N**	**Y**	**R3** **N**	**Y**	**R4** **N**	**Y**	**R5** **N**	**Y**
Phases Formed	**Chemical Formula**	**State**[1]										
Potassium magnesium aluminum oxide	$KMg_2Al_{15}O_{25}$	s							**X**			
Iron - BCC	Fe	s							**X**			
Olivine	$(Mg,Fe,Ca)(Mg,Fe)SiO_4$	ss								**X**		
No. Calculation Steps Completed:			15	15	15	15	3	2	2	2	2	2

[1] s = solid; ss = solid solution; l = liquid; ls = liquid solution

The ability of a slag solution to dissolve the refractory material was estimated through calculation of the metastable diffusion factor of each major refractory phase in the slag. Refractory phases with a diffusion factor of >100 K/Pa·s have been tied to observations of significant refractory dissolution, while those with diffusion factors <50 K/Pa·s showed negligible dissolution [20]. As observed in Table 3-4, while the refractory phases have higher metastable diffusion factors in the fluxed slag due to its lower viscosity, in no case is significant dissolution of the refractory expected. Based on the propensity for refractory dissolution alone, all of the studied refractory materials are good candidates for the lining of the DCSG combustor.

Table 3-4. Predicted diffusion factors of major refractory phases in fluxed (20 wt % $CaMgO_2$) and non-fluxed MFT-OPW slag solutions at 1300 °C. Phases representing <10 wt % of the refractory were not considered. Values are reported for initial contact between pure slag and pure refractory. Viscosity of non-fluxed slag = 646 Pa·s; viscosity of fluxed slag = 24.7 Pa·s.

		Metastable Diffusion Factor (K/Pa·s)	
Refractory Material	**Refractory phase added**	**No Flux**	**Flux**
R1	Mullite	5.70×10^{-7}	15.8
	Zirconia	1.31×10^{-2}	8.20×10^{-1}
R2	Silicon carbide	4.87×10^{-4}	0[1]
	Mullite	4.80×10^{-7}	15.8
	Anorthite	3.55×10^{-1}	18.4
R3	Corundum $(Cr,Al)_2O_3$	1.01×10^{-3}	1.53×10^{-1}
R4	Magnesium aluminate spinel ($MgAl_2O_4$)	1.26×10^{-1}	5.37
R5	Chromia spinel ($MgCr_2O_4$)	2.52×10^{-3}	6.93×10^{-2}
	Chromia	2.71×10^{-3}	0[1]

[1]Within the resolution of the model, no amount of refractory could be dissolved in the slag, thus yielding a concentration driving force of 0 between the saturated and non-saturated slag.

3.4.5 Refractory corrosion tests

A subset of the five refractory materials used in the corrosion models were obtained for further testing. R1 and R2 were selected to validate the assumption of poorer performance based on the models, while R3 was selected to confirm its predicted corrosion resistance. The properties of these refractories, including pore size distributions and surface morphology, have been characterized previously (Section 2.7.1.2). Table 3-S1 shows baseline measurements for the

composition of each refractory material by SEM-EDX, which were used to inform cut-off limits (Table 3-S2) of the various species in each refractory when considering penetration depth. Due to the heterogeneous nature of the refractory materials, local concentrations can vary quite widely compared to the bulk compositions provided by the manufacturer, limiting the resolution when comparing penetration of species that are both in the slag and in the bulk refractory. Better resolution can be obtained by looking at the species that are contained in the slag phase but not in the untreated refractory.

Performance of the three refractory materials in contact with the non-fluxed MFT-OPW mixture were assessed by sessile drop corrosion tests. This method has been shown previously to yield comparable results to the more rigorous corrosion cup tests (Section 2.4.4.3). As discussed above in Section 3.4.1, the liquidus of this inorganic mixture is > 1600 °C, which is above the test temperature (1300 °C, as selected in Section 3.4.2). Thus, only a portion of the inorganic sample was liquid throughout the duration of this test. As seen in Figure 3-7 B, the R1 refractory was discoloured to a dark grey following the test, while the R2 and R3 refractories (Figure 3-7 E & H) appeared unaffected at the macro scale. In the SEM images (Figure 3-7 C, F & I), the transition between the slag layer and the surface of the refractory is depicted by the red lines and was recognizable by a shift in the bulk concentrations measured by EDX. Dislodged refractory grains, which can be a sign of dissolution, were not observed in the slag layer, and the morphology of the refractory below the interface appeared unaffected relative to the untreated refractory material (Section 2.4.4.1).

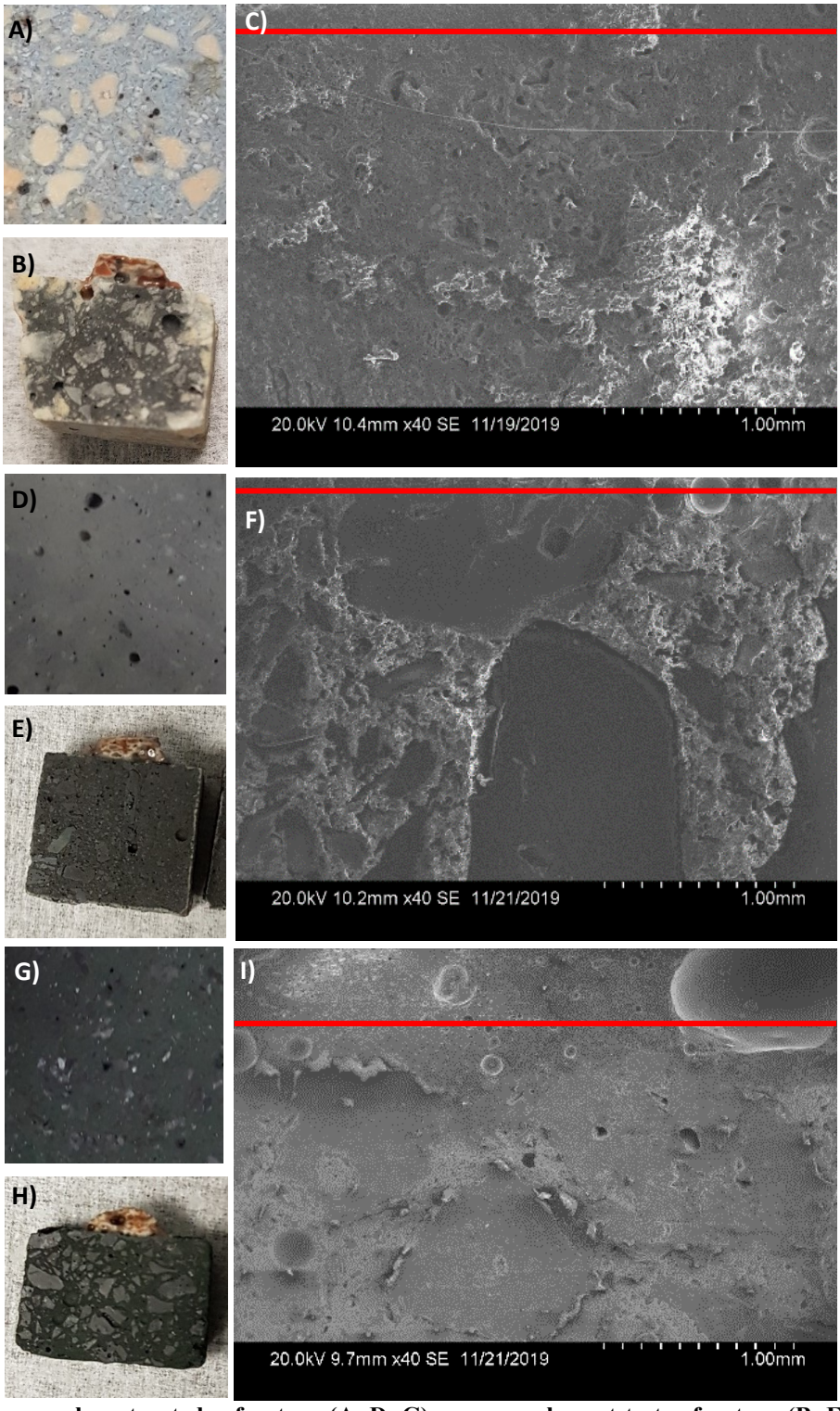

Figure 3-7. Macro-scale untreated refractory (A, D, G) macro-scale post-test refractory (B, E, H) and SEM post-test images (C, F, I) of cross-sections of R1 (A-C), R2 (D-F) and R3 (G-I) for sessile drop corrosion tests with non-fluxed MFT-OPW at 1300 °C.

The performance of the refractory materials in contact with the fluxed MFT-OPW slag was more rigorously tested with the cup corrosion method. Again, the transition between the slag and refractory layer was marked by a shift in the bulk composition by EDX. An increase in porosity was also observed upon transition from the slag to the refractory. Figure 3-8 A shows discolouration of the R1 refractory material to a dark grey deep into the areas below and beside the slag pool. R2 (Figure 3-8 B) had a thin glassy layer on exposed surfaces, likely from oxidation of SiC to SiO_2, but appeared otherwise unaffected. Likewise, R3 (Figure 3-8 C) appeared unaffected on the macro scale. In the SEM image of R3 (Figure 3-8 F), a dislodged refractory grain is indicated by the red arrow, indicating some dissolution of the refractory by the slag. This is corroborated by the green colouration of the slag layer and by EDX measurements, indicating chromia has migrated to the slag.

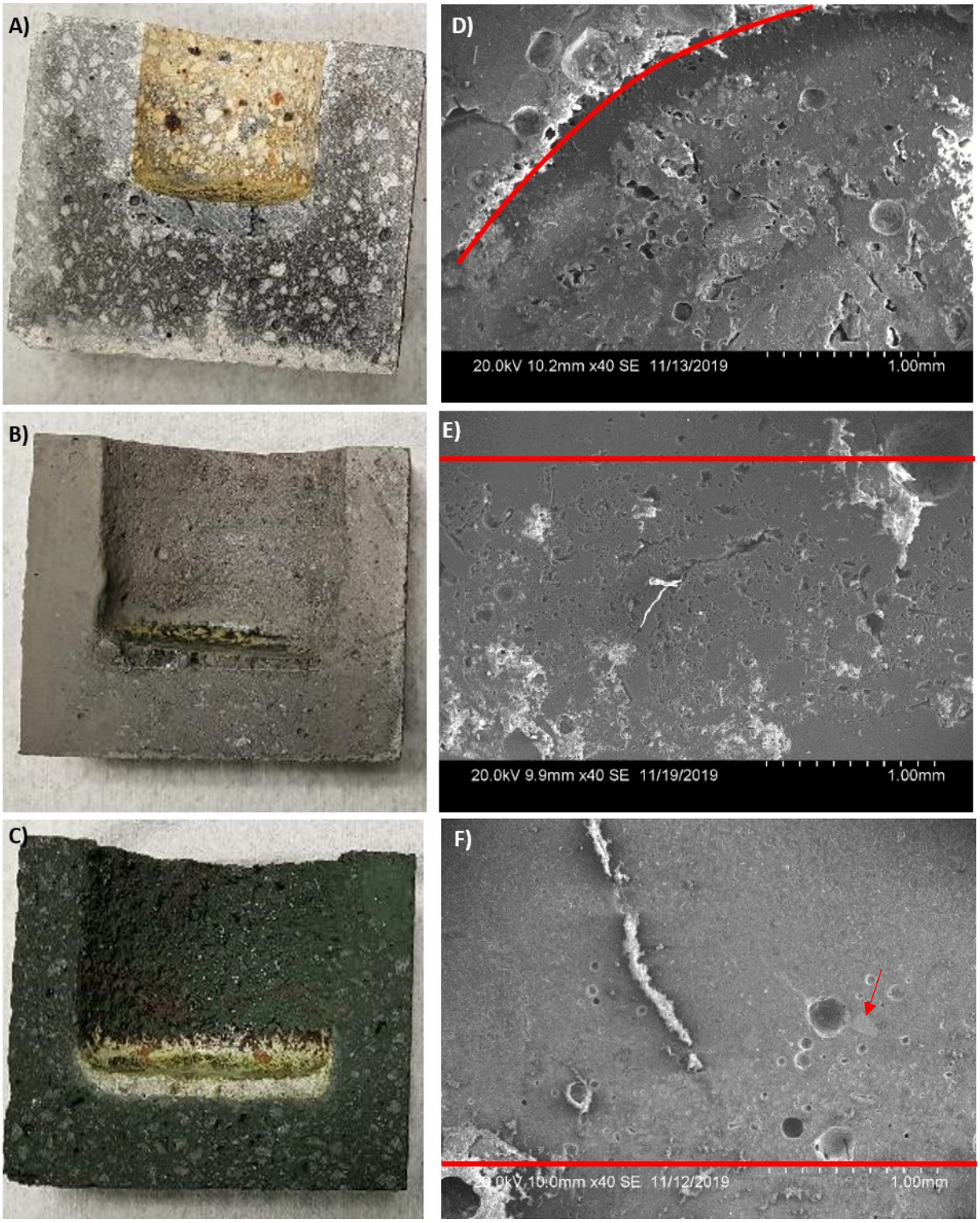

Figure 3-8. Macro-scale (A-C) and SEM images (D-F) of cross-sections of refractory R1 (A, D), R2 (B, E) and R3 (C, F) following cup corrosion tests with fluxed (20 wt % $CaMgO_2$) MFT-OPW at 1300 °C. The red line indicates the slag-refractory interface and the arrow indicates a dislodged refractory grain.

Table 2-6 shows the penetration depth of various species contained within the slag into the refractory materials in the two sets of tests. The sessile drop and cup corrosion tests are not directly comparable due to the much lower ratio of liquid compared to refractory in the non-fluxed sessile drop tests and the differing geometry, however it can be seen that in both cases R1 was completely penetrated by Na_2O. The presence of Na_2O within the refractory may lead to formation of damaging low-density feldspars as predicted by the corrosion models in Section 3.4.4. Thus, the susceptibility of silica-based refractories to attack by K_2O noted by other researchers [15], [38], [39] appears to hold true for Na_2O as well. For the non-fluxed MFT-OPW, aside from Na_2O, the only species showing deep penetration was Fe_2O_3 into R2. This may be a false positive, because the silicon carbide refractory contains 0.2 wt % Fe_2O_3 on a bulk basis. Since this is a heterogeneous refractory, it is possible that there are inclusions that are locally higher in concentration of Fe_2O_3 and unrelated to penetration by exogenous species. As seen in Figure 3-S6, only sporadic points showed Fe_2O_3 concentrations greater than the cut-off threshold, whereas a gradual concentration gradient would be expected for slag penetration. For the fluxed MFT-OPW, differences in mobility of species are evident. CaO and MgO, while they did penetrate the refractory materials, did not traverse as deeply into the refractory as Na_2O. It is hypothesized that the presence of Na_2O deeper within the refractory may have been a result of a mechanism other than slag penetration, such as gas-phase transport and condensation, whereas the CaO and MgO may represent the true slag front for the fluxed MFT-OPW. Based on the FactSage deposition models, there are several sodium species that are predicted to be present in the gas phase thus supporting the idea of gas-phase transport.

Regardless of whether the MFT-OPW is fluxed or not, R3 offered the greatest resistance to penetration by Na_2O. With the presence of significant quantities of Na_2O being the main difference

between typical coal conversion slags and those used in this study, it is confirmed that this commonly used refractory for coal conversion processes still offered a good corrosion resistance in this application. R2 performed well for the non-fluxed slag, but is not recommended for the fluxed slag due to the Na_2O penetration unless formation of an interfacial silica layer from oxidation of the SiC is capable of halting further penetration. Other researchers have reported protective effects of interfacial silica layers for silicon carbide refractories. This could be assessed through additional experimentation with multiple time points, to see if the penetration depth stops increasing after a certain amount of time. It is also possible that the still relatively high aluminosilicate proportion of this refractory (Table 3-2) was the reason that Na_2O was able to penetrate around the SiC grains, and that choosing a higher-proportion SiC refractory, or refractory with a different binder phase, could improve penetration resistance. For the fluxed slag, all refractories performed comparably in terms of resistance to penetration by CaO and MgO.

Table 3-5. Observed penetration depth of species found in fluxed (20 wt % $CaMgO_2$) and non-fluxed MFT-OPW slags in various refractory materials following corrosion tests at 1300 °C. Concentration thresholds for which a species was said to penetrate the refractory are defined in Table 3-S2. A zero indicated no penetration, while a dash (-) indicates the species was not present in the experiment.

	R1		R2		R3	
Flux (Y/N):	**N**	**Y**	**N**	**Y**	**N**	**Y**
Species	**Penetration Depth (mm)**					
Na_2O	Full penetration	Full penetration	0.00	2.66	0.10	0.76
CaO	-	0.38	-	0.00	-	0.38
MgO	-	0.38	-	0.38	-	0.00
K_2O	0.00	0.00	0.00	0.00	0.00	0.00
Fe_2O_3	0.00	0.00	12.16	0.00	0.10	0.00
SiO_2	-	-	-	-	0.10	0.76
Total refractory depth (mm)	10.64	31.90	13.30	22.80	9.98	20.10

3.5 Conclusions

Use of MFT-OPW from mining operations as the water source for DCSG resulted in mainly solid inorganic deposits at temperatures below 1600 °C and severely fouled the combustor. To improve operability with this water source and maximize steam throughput for a given firing rate, dolomite was identified as the optimal fluxant at a proportion of 20 wt % $CaMgO_2$ within the total solid and dissolved inorganic species injected to the combustor. This would allow for operation of the combustor at a temperature of 1300 °C while maintaining a steady-flowing slag layer to avoid solids build-up and plugging of the combustor. Viscosity experiments validated the use of the Duchesne *et al* viscosity model for the fluxed slag mixture. Should it be necessary to alter the amount of flux required in the solution, adapt to small differences in MFT-OPW composition or use limestone instead of dolomite based on materials availability, the viscosity of the resultant slag can be predicted with reasonable accuracy. Further experiments are recommended for the economic optimization of the proportion of flux and operating temperature.

Candidate refractory materials for the lining of the DCSG combustor were investigated at 1300 °C both with and without fluxant. Models showed that aluminosilicate refractory materials should not be used due to their risk of forming low-density solid species, such as feldspar, which can damage the refractory material through volume expansion and shorten its lifetime. A chromia-corundum refractory showed the greatest resistance to penetration among those tested in the laboratory, though some dissolution of the chromia was evident in the slag layer. From the corrosion models, a magnesium aluminate spinel and a chromia spinel also showed good resistance to the slags and merit further testing.

3.6 References

[1] L. Botha and J. B. P. Soares, "The influence of tailings composition on flocculation," *Can. J. Chem. Eng.*, vol. 93, no. 9, pp. 1514–1523, Sep. 2015, doi: 10.1002/cjce.22241.

[2] E. W. Allen, "Process water treatment in Canada's oil sands industry: I. Target pollutants and treatment objectives," *J. Environ. Eng. Sci.*, vol. 7, no. 2, pp. 123–138, Mar. 2008, doi: 10.1139/S07-038.

[3] A. Farkish, "SAP based rapid dewatering of oil sands mature fine tailings," University of Ottawa, Ottawa, ON, 2013.

[4] P. E. C. Cairns *et al.*, "High-pressure oxy-firing (HiPrOx) of fuels with water for the purpose of direct contact steam generation," *Energy Fuels*, vol. 29, no. 7, pp. 4522–4533, Jul. 2015, doi: 10.1021/ef502754h.

[5] J. Seaba, D. Wissmiller, and S. Alavandi, "Advanced steam generation: Technologies for Canadian oil sands," Gas Technology Institute, 2017. Accessed: Apr. 30, 2020. [Online]. Available: https://www.cosia.ca/uploads/documents/id46/COSIA%20Advanced%20Steam%20Generation%20-%20Technologies%20for%20Canadian%20Oil%20Sands.pdf.

[6] M. Wolinetz, "DCSG market analysis," Navius Research, 2013.

[7] J. Masliyah, Z. J. Zhou, Z. Xu, J. Czarnecki, and H. Hamza, "Understanding water-based bitumen extraction from Athabasca oil sands," *Can. J. Chem. Eng.*, vol. 82, no. 4, pp. 628–654, 2004, doi: https://doi.org/10.1002/cjce.5450820403.

[8] P. K. A. Hong, Z. Cha, X. Zhao, C.-J. Cheng, and W. Duyvesteyn, "Extraction of bitumen from oil sands with hot water and pressure cycles," *Fuel Process. Technol.*, vol. 106, pp. 460–467, Feb. 2013, doi: 10.1016/j.fuproc.2012.09.013.

[9] J. Nakano, S. Sridhar, J. Bennett, K.-S. Kwong, and T. Moss, "Interactions of refractory materials with molten gasifier slags," *Int. J. Hydrog. Energy*, vol. 36, no. 7, pp. 4595–4604, Apr. 2011, doi: 10.1016/j.ijhydene.2010.04.117.

[10] S. Vargas, F. J. Frandsen, and K. Dam-Johansen, "Rheological properties of high-temperature melts of coal ashes and other silicates," *Prog. Energy Combust. Sci.*, vol. 27, no. 3, pp. 237–429, Mar. 2001, doi: 10.1016/S0360-1285(00)00023-X.

[11] K. Loganathan, P. Chelme-Ayala, and M. Gamal El-Din, "Effects of different pretreatments on the performance of ceramic ultrafiltration membrane during the treatment of oil sands tailings pond recycle water: A pilot-scale study," *J. Environ. Manage.*, vol. 151, pp. 540–549, Mar. 2015, doi: 10.1016/j.jenvman.2015.01.014.

[12] Allied Mineral Products, Inc., "TUFFCRETE® AZS 4 X," Columbus, United States, TUFCAZS4X, Jan. 2016.

[13] "THOR 60 ADTECH." Harbison Walker International.

[14] PD Refratories GmbH, "Chromium Corundum Bricks," 2017. https://www.pd-refractories.com/website/en/products/chromium_bricks/chromium_corundum_bricks.php (accessed Nov. 28, 2017).

[15] M. Carlborg, F. Weiland, C. Ma, R. Backman, I. Landälv, and H. Wiinikka, "Exposure of refractory materials during high-temperature gasification of a woody biomass and peat mixture," *J. Eur. Ceram. Soc.*, vol. 38, no. 2, pp. 777–787, Feb. 2018, doi: 10.1016/j.jeurceramsoc.2017.09.016.

[16] J. Bennett, A. Nakano, J. Nakano, and H. Thomas, "Gasification slag and the mechanism by which phosphorous additions reduce slag wear and corrosion in high Cr_2O_3 refractories,"

in *Advances in Molten Slags, Fluxes and Salts: Proceedings of the 10th International Conference on Molten Slags, Fluxes and Salts*, 2016, pp. 1109–1116.

[17] C. W. Bale *et al.*, "FactSage thermochemical software and databases, 2010–2016," *Calphad*, vol. 54, pp. 35–53, Sep. 2016, doi: 10.1016/j.calphad.2016.05.002.

[18] M. A. Duchesne, A. M. Bronsch, R. W. Hughes, and P. J. Masset, "Slag viscosity modeling toolbox," *Fuel*, vol. 114, pp. 38–43, Dec. 2013, doi: 10.1016/j.fuel.2012.03.010.

[19] "Methods of test for dense refractory products - Guidelines for testing the corrosion of refractories caused by liquids (CEN/TS 15418:2006)." European Committee for Standardization, 2006.

[20] M. A. Duchesne, A. D. Hall, R. W. Hughes, D. J. McCalden, E. J. Anthony, and A. Macchi, "Fate of inorganic matter in entrained-flow slagging gasifiers: Fuel characterization," *Fuel Process. Technol.*, vol. 118, pp. 208–217, Feb. 2014, doi: 10.1016/j.fuproc.2013.09.004.

[21] X. Chen *et al.*, "The key for sodium-rich coal utilization in entrained flow gasifier: The role of sodium on slag viscosity-temperature behavior at high temperatures," *Appl. Energy*, vol. 206, pp. 1241–1249, Nov. 2017, doi: 10.1016/j.apenergy.2017.10.020.

[22] G. J. Browning, G. W. Bryant, H. J. Hurst, J. A. Lucas, and T. F. Wall, "An empirical method for the prediction of coal ash slag viscosity," *Energy Fuels*, vol. 17, no. 3, pp. 731–737, May 2003, doi: 10.1021/ef020165o.

[23] X. Wang *et al.*, "Effect of CaF_2 on the viscosity and microstructure of $CaO–SiO_2–Al_2O_3$ based continuous casting mold flux," *Metals*, vol. 9, no. 8, p. 871, Aug. 2019, doi: 10.3390/met9080871.

[24] H. Abdeyazdan, H. Edris, and M. H. Abbasi, "The effect of CaF2 content in hot metal pretreatment flux based on lime," *International Journal of ISSA*, vol. 8, no. 2, pp. 5–8, 2011.

[25] W. E. Lee and S. Zhang, “Melt corrosion of oxide and oxide–carbon refractories,” *Int. Mater. Rev.*, vol. 44, no. 3, pp. 77–104, Mar. 1999, doi: 10.1179/095066099101528234.

[26] M. A. Duchesne *et al.*, “Flow behaviour of slags from coal and petroleum coke blends,” *Fuel*, vol. 97, pp. 321–328, Jul. 2012, doi: 10.1016/j.fuel.2012.02.019.

[27] T. Vojnovich, “Refractories for coal gasification and combustion systems,” Westinghouse Research and Development Center, Pittsburg, PA, EPRI-AP-1268, Jul. 1980. doi: 10.2172/5360793.

[28] T. K. Kaneko, H. Thomas, J. P. Bennett, and S. Sridhar, “Synthetic coal slag infiltration into varying refractory materials,” *J. Am. Ceram. Soc.*, vol. 95, no. 10, pp. 3325–3333, Oct. 2012, doi: 10.1111/j.1551-2916.2012.05350.x.

[29] Z. Zhou *et al.*, “Interactions of high-chromia refractory materials with infiltrating coal slag in the oxidizing atmosphere of a cyclone furnace,” *Ceram. Int.*, vol. 40, no. 3, pp. 3829–3839, Apr. 2014, doi: 10.1016/j.ceramint.2013.08.023.

[30] V. Krishnamoorthy and S. V. Pisupati, “A critical review of mineral matter related issues during gasification of coal in fixed, fluidized, and entrained flow gasifiers,” *Energies*, vol. 8, no. 9, Art. no. 9, Sep. 2015, doi: 10.3390/en80910430.

[31] P. Biedenkopf *et al.*, “Vaporization and corrosion of refractories in the presence of pressurized pulverized coal combustion slag,” *J. Am. Ceram. Soc.*, vol. 84, no. 7, pp. 1445–1452, Dec. 2004, doi: 10.1111/j.1151-2916.2001.tb00858.x.

[32] J. Wells, G. Riley, and J. Williamson, “Interactions between coal-ash and burner quarls. Part 2: resistance of different refractory materials to slag attack in a combustion test facility,” *Fuel*, vol. 82, no. 15–17, pp. 1867–1873, Oct. 2003, doi: 10.1016/S0016-2361(03)00164-9.

[33] C. H. Schroder and E. C. Prowse, “Silicon carbide refractories in incinerators,” in *Proceedings of the National Incinerator Conference*, New York, United States, 1966, pp. 199–201.

[34] D. Olevano, P. Miceli, U. Martini, A. di Donato, and S. Martelli, “Criteria to select the refractory lining in biomass co-combustion reactors for energy production,” *Advances in Science and Technology*, 2014. http://www.scientific.net/AST.92.288 (accessed Dec. 03, 2020).

[35] S. Arvelakis, B. Folkedahl, K. Dam-Johansen, and J. Hurley, “Studying the melting behavior of coal, biomass, and coal/biomass ash using viscosity and heated stage XRD Data,” *Energy Fuels*, vol. 20, no. 3, pp. 1329–1340, May 2006, doi: 10.1021/ef050168b.

[36] J. P. Bennett, K.-S. Kwong, and C. A. Powell, “Issues Impacting Refractory Service Life in Biomass/Waste Gasification,” presented at the NACE - International Corrosion Conference Series, 2007.

[37] T. Heinzel, V. Siegle, H. Spliethoff, and K. R. G. Hein, “Investigation of slagging in pulverized fuel co-combustion of biomass and coal at a pilot-scale test facility,” *Fuel Process. Technol.*, vol. 54, no. 1, pp. 109–125, Mar. 1998, doi: 10.1016/S0378-3820(97)00063-5.

[38] D. N. Togobitskaya, A. F. Khamkhot’ko, N. A. Tsivataya, and D. A. Stepanenko, “Corrosion activity of alkali-containing slags with respect to a blast furnace refractory lining,” *Refract. Ind. Ceram.*, vol. 54, no. 3, pp. 155–159, Sep. 2013, doi: 10.1007/s11148-013-9568-9.

[39] S. Schaafhausen, E. Hugon, E. Yazhenskikh, B. Wilhelmi, and M. Müller, “Corrosion of refractory materials in fluidised bed gasification of alkali rich fuels,” *Adv. Appl. Ceram.*, vol. 114, no. 1, pp. 55–64, Jan. 2015, doi: 10.1179/1743676114Y.0000000191.

[40] J. Roy, S. Chandra, S. Das, and S. Maitra, “Oxidation behaviour of silicon carbide - a review,” *Rev. Adv. Mater. Sci*, vol. 38, pp. 29–39, 2014.

[41] R. G. Munro and S. J. Dapkunas, “Corrosion characteristics of silicon carbide and silicon nitride,” *J. Res. Natl. Inst. Stand. Technol.*, vol. 98, no. 5, p. 607, Sep. 1993, doi: 10.6028/jres.098.040.

3.7 Supplementary Data

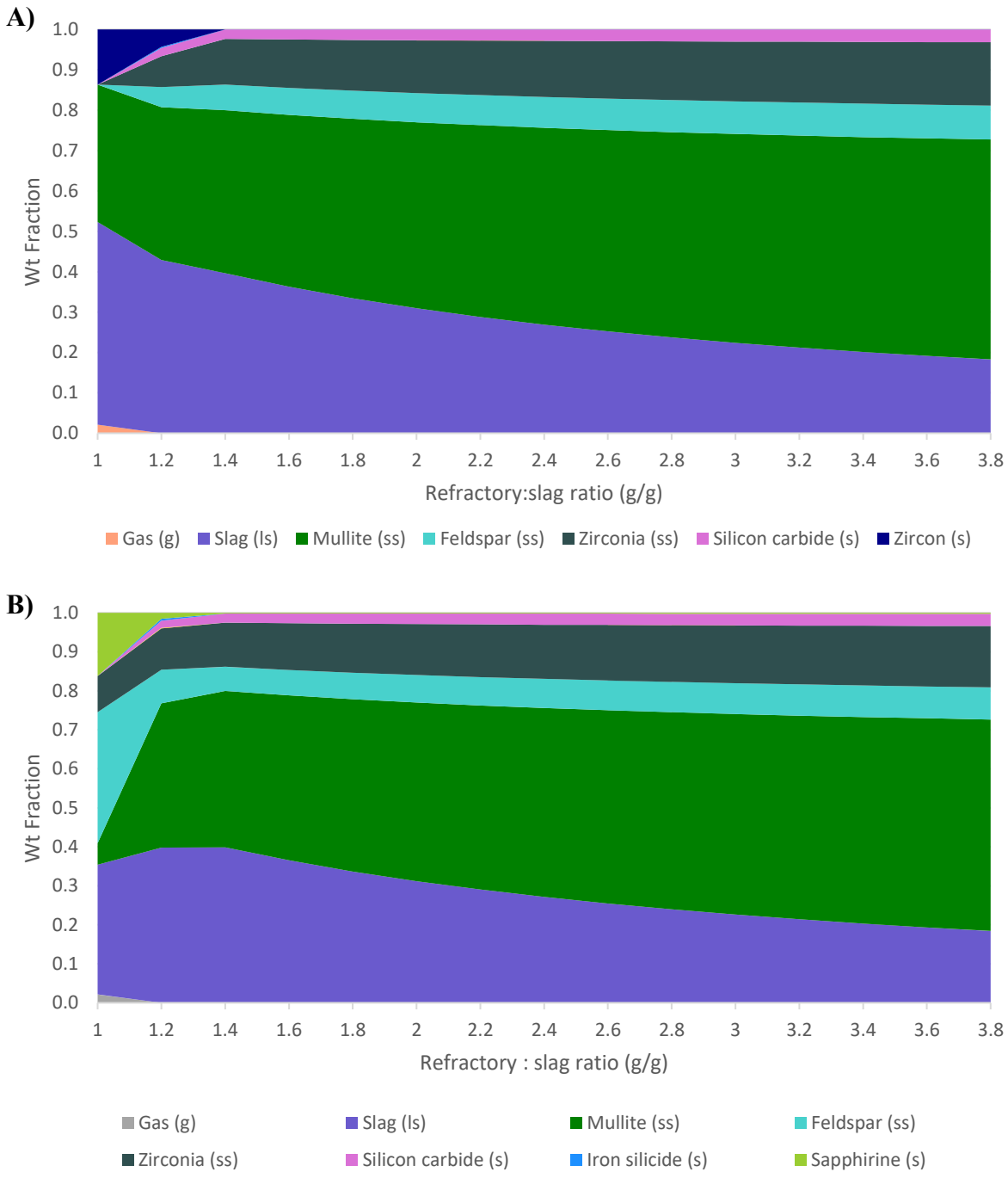

Figure 3-S1. Phases formed during the stepwise addition of A) non-fluxed and B) $CaMgO_2$-fluxed MFT-OPW slag into refractory R1 at 1300 °C and 55 barg. Phases < 1 wt % are excluded.

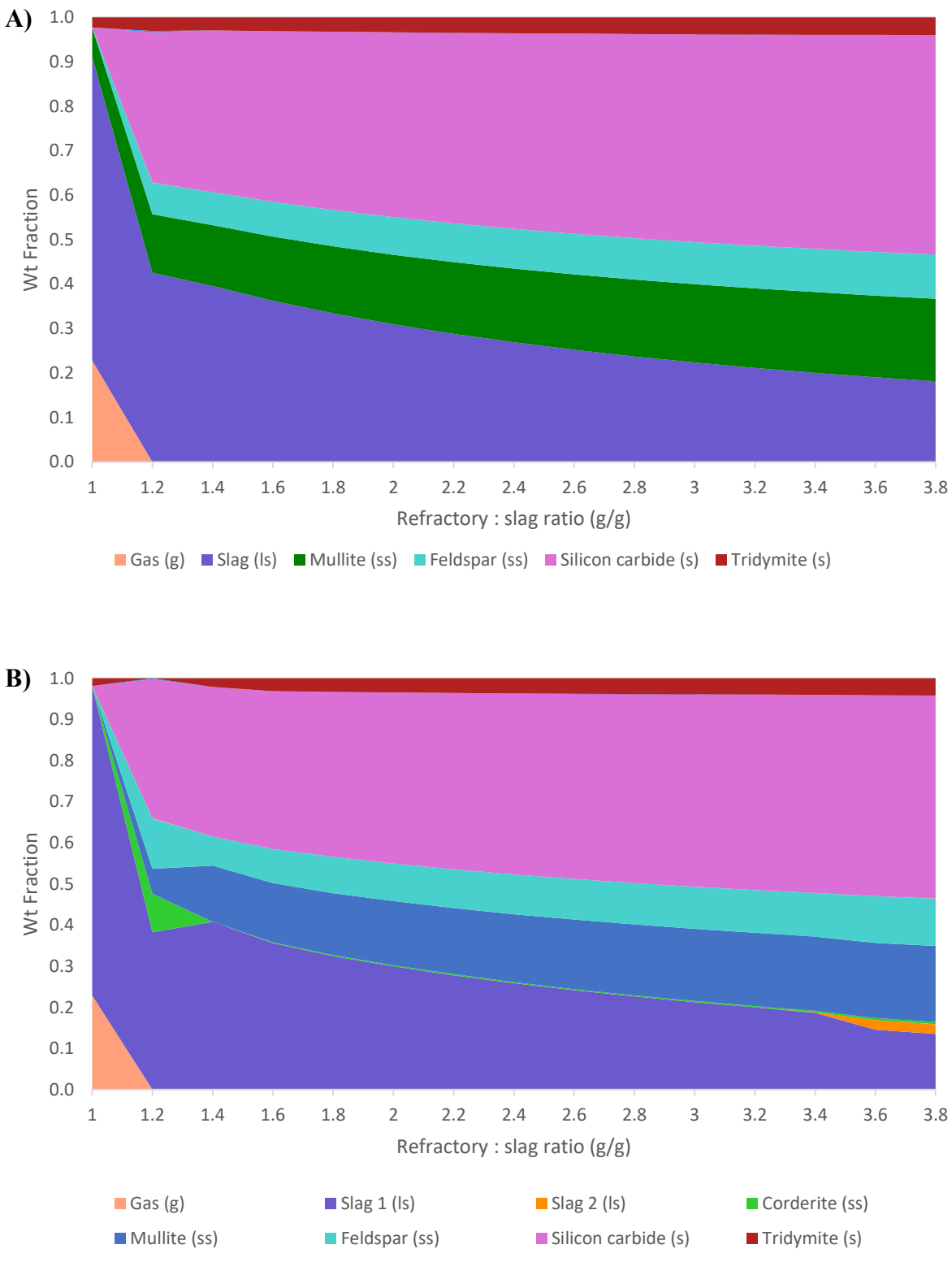

Figure 3-S2. Phases formed during the stepwise addition of A) non-fluxed and B) $CaMgO_2$-fluxed MFT-OPW slag into refractory R2 at 1300 °C and 55 barg. Phases < 1 wt % are excluded.

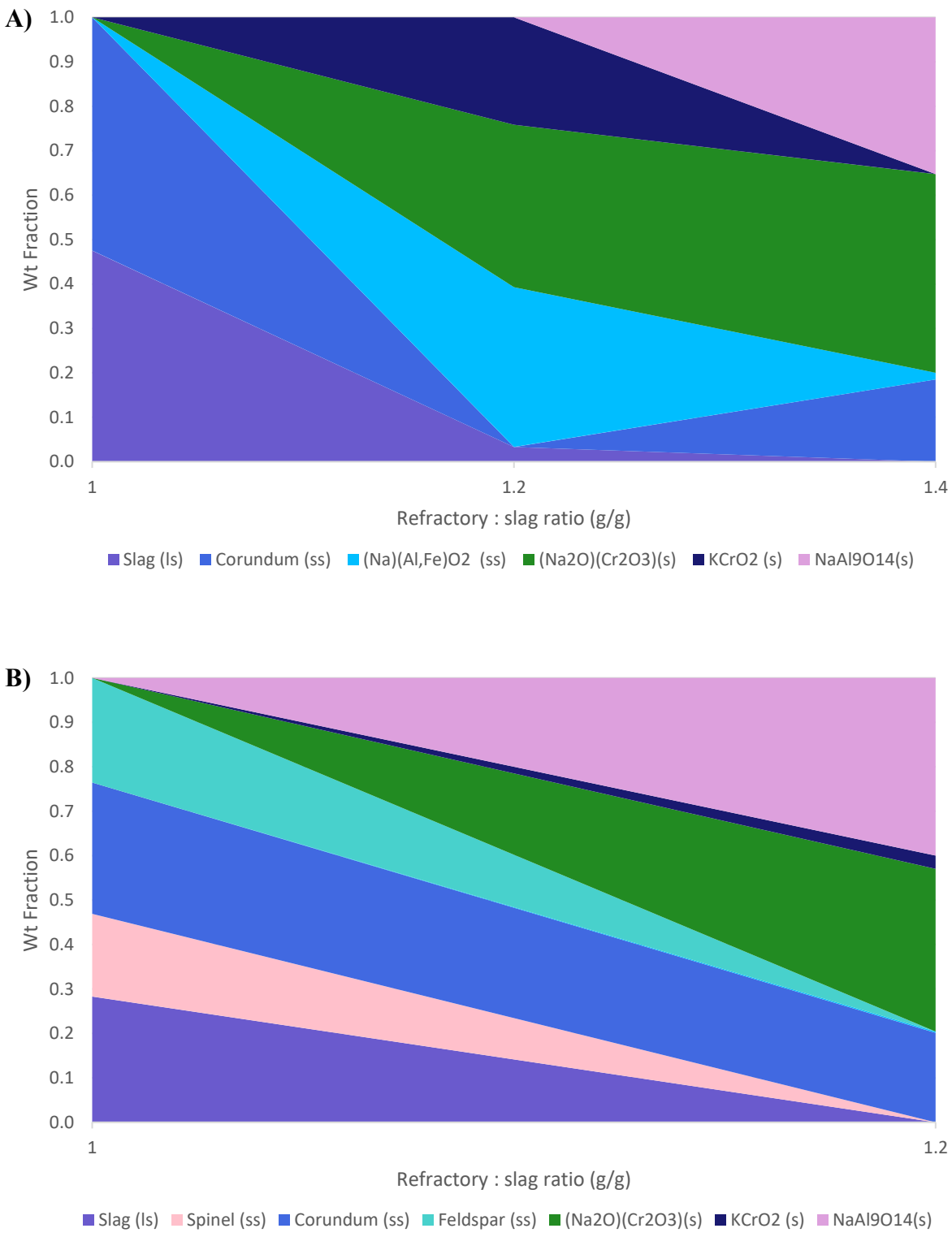

Figure 3-S3. Phases formed during the stepwise addition of A) Non-fluxed and B) $CaMgO_2$-fluxed MFT-OPW slag into refractory R3 at 1300 °C and 55 barg. Phases < 1 wt % are excluded.

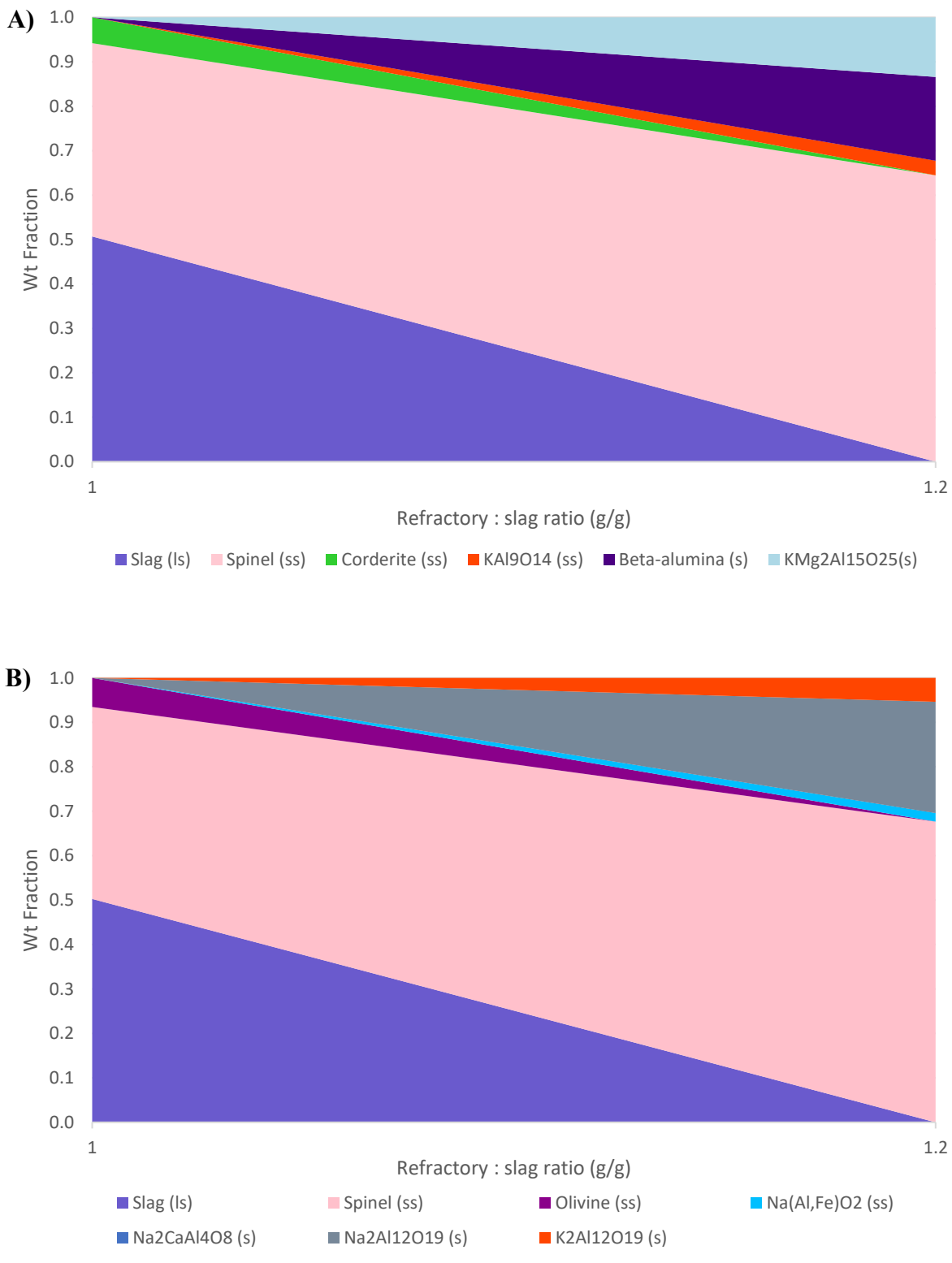

Figure 3-S4. Phases formed during the stepwise addition of A) non-fluxed and B) $CaMgO_2$-fluxed MFT-OPW slag into refractory R4 at 1300 °C and 55 barg. Phases < 1 wt % are excluded.

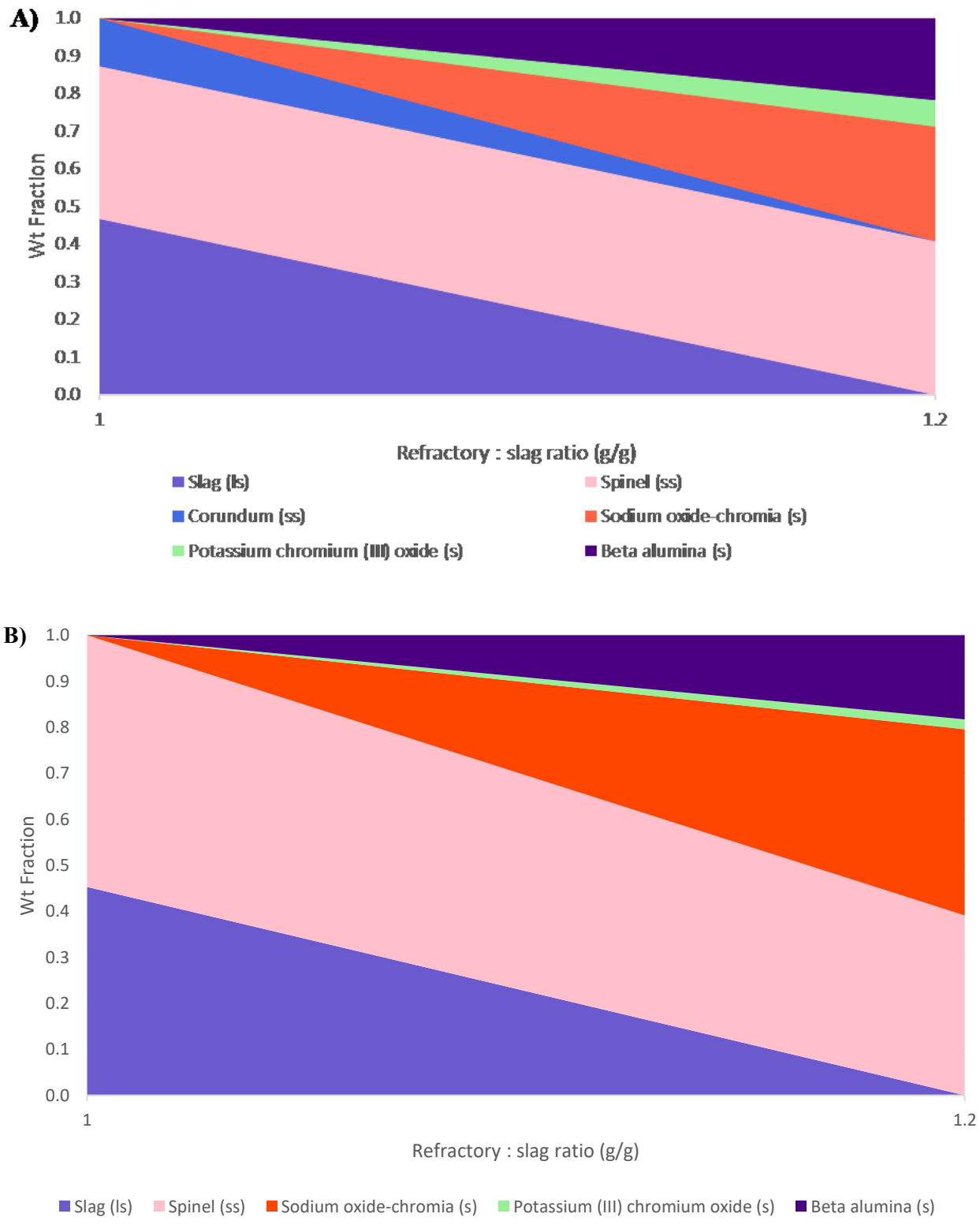

Figure 3-S5. Phases formed during the stepwise addition of A) non-fluxed and B) $CaMgO_2$-fluxed MFT-OPW slag into refractory R5 at 1300 °C and 55 barg. Phases < 1 wt% are excluded.

Table 3-S1. Baseline measurements of composition of pure refractory materials by area scans with SEM-EDX.

		Wt %									
		Na_2O	Al_2O_3	SiO_2	SiC	CaO	ZrO_2	Fe_2O_3	TiO_2	Cr_2O_3	MgO
R1	Min	0.00	0.71	0.00	0.00	0.00	3.20	0.00	0.00	-	-
	Max	0.76	74.66	39.66	0.00	2.31	99.29	0.82	0.90	-	-
	Avg	0.07	23.70	5.10	0.00	0.32	70.66	0.07	0.08	-	-
R2	Min	0.00	0.17	0.00	0.00	0.00	-	0.00	-	-	-
	Max	0.00	43.09	73.12	99.83	7.44	-	1.07	-	-	-
	Avg	0.00	24.71	48.40	22.93	3.64	-	0.32	-	-	-
R3	Min	0.00	10.06	0.00	-	0.00	-	-	0.00	65.41	0.00
	Max	0.38	29.31	2.31	-	13.26	-	-	0.66	89.61	0.46
	Avg	0.06	19.41	0.38	-	1.23	-	-	0.04	78.83	0.05

Table 3-S2. Cut-off thresholds for determination of penetration depth into refractory for SEM-EDX experiments.

Refractory:	R1	R2	R3
Species		**Thresholds (wt %)**	
Na_2O	1	1	1
CaO	4	8	1.5
MgO	1	1	1
K_2O	1	1	1
Fe_2O_3	1	1.5	1
SiO_2	-	-	3

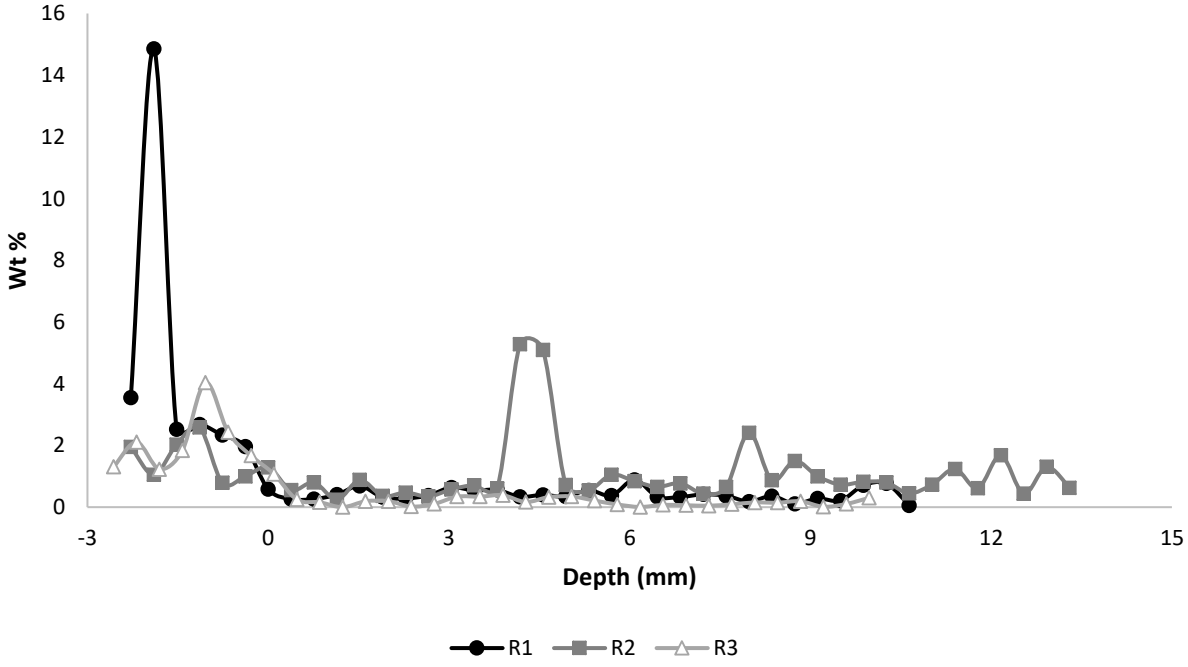

Figure 3-S6. Concentration of Fe_2O_3 with increasing depth into refractory materials after sessile drop corrosion tests with non-fluxed MFT-OPW at 1300 °C.

Chapter 4. Conclusions and future work

This work examined the fate of inorganics in the combustor for two DCSG applications in the Canadian oil sands to establish recommended operating points and refractory materials. For both SAGD and surface mining operations, silicate deposits rich in Na_2O were predicted to form in the combustor, though the properties of these deposits were quite different between the two cases.

For SAGD applications using FWKD as the process water, the presence of Na_2SO_4 in the slag increased at lower combustor wall temperatures (the assumed equilibrium temperature of the inorganics), and the increased Na_2SO_4 content served to decrease the slag viscosity. Thus operation of the combustor in the moderate to lower temperature range studied (1075 – 1250 °C) should not be problematic in terms of being able to generate a flowing slag layer. At the lowest temperature studied (1075 °C), a low viscosity molten salt solution was also predicted to form, which resulted in structural changes to two of the three refractory materials tested. The operating temperature of the combustor in regions where fresh inorganic material will contact the wall should thus be sufficiently high (≥1200 °C) that this potentially corrosive salt phase will not form, but otherwise minimized since a lower temperature maximizes the steam throughput for a given firing rate and reduces the kinetics of corrosion.

For mining applications using MFT, dilution with another oil sands processing water is likely required due to the high solids content (approximately 30 wt %) of the MFT. Even when diluted with OPW at a mass ratio of 24:1, the deposits were high in silica and had a liquidus temperature >1600 °C, indicating that a sticky solid layer is likely to accumulate and plug the combustor since a flowing liquid slag layer cannot be formed. To improve operability of the combustor, dolomite was identified as a fluxant to reduce the liquidus of the inorganic deposits resulting from the MFT-OPW. It was found that incorporation of 20 wt % $CaMgO_2$ in the mixture was optimal and resulted

in a slag with a viscosity of < 25 Pa·s at temperatures ≥ 1300 °C. From a process perspective, like for SAGD, it is desired to minimize the operating temperature of the combustor, though the final selection of the concentration of fluxant and resultant allowable operating temperature will require further work for economic optimization.

For both SAGD and mining applications, refractory corrosion models and corrosion tests yielded similar conclusions and showed that the rule of thumb that acidic or neutral refractories will be suitable for acidic slags (as is the case for all of the slags studied in this work) does not hold for these applications. Due to the high concentration of Na_2O in the slag for both applications, refractory materials high in alumina and/or silica should be avoided due to the possibility of forming low density solids such as nepheline or feldspar upon reaction with the alkali. These low density solids have the potential to cause damage to the refractory through volume expansion, and may severely shorten refractory life. As expected, during experimental work, the mullite zirconia refractory was deeply penetrated by Na_2O and in some cases showed dissolution of the binder phase. The silicon carbide refractory performed better but still showed substantial penetration by Na_2O, likely through the aluminosilicate binder phase. A refractory with a higher proportion of silicon carbide or a different binder may offer improved corrosion resistance. Finally, a chromia corundum refractory yielded the highest overall resistance to penetration of the refractories tested experimentally, though dissolution of the chromia in the slag layer was still evident. Based on these results, a high chrome oxide refractory material is recommended for further investigation for the DCSG combustor for both applications. More work is required to determine the dissolution rate of chromia in the slag to establish how it will affect refractory life, and if solid phases forming at the slag-refractory interface will slow or halt further attack. Two other refractories from the models yielded promising results and warrant further testing: a chromia spinel ($MgCr_2O_4$) and a

magnesium aluminate spinel ($MgAl_2O_4$). Incorporation of the chromium into the spinel lattice instead of as a free Cr_2O_3 grain is believed to reduce the susceptibility of the refractory to dissolution by the slag. The close packing of atoms in the spinel structure may also make a magnesium aluminate spinel refractory less susceptible to attack compared to the other aluminum-containing refractories tested. This refractory offers advantages of reduced cost and reduced environmental impact compared to chromium-containing refractories.

Future work could include testing the impact of gaseous species in the combustor such as Cl, Na, S and steam on refractory materials. Most refractory surfaces are expected to be coated with a liquid slag layer, however, diffusion of these gaseous species through the slag is possible and thus relevant to consider. As a step toward scale up, refractory from the DCSG pilot plant constructed by CanmetENERGY Ottawa could be assessed to validate slag compositions resulting from the models and examine refractory wear.

This work focused on refractory suitability based on resistance to chemical attack by the liquid phase, which is assumed to coat all interior refractory surfaces at steady state. Equally important are the mechanical properties of the refractory such as elastic modulus, toughness and thermal shock resistance. From current work, it is unclear how the slag-refractory interactions may affect these physical properties. Tests to assess mechanical strength, such as crushing tests, are suggested to characterize the refractory sample before and after corrosion testing.